THE UNIVERSITY OF CHICAGO

STATISTICAL PROPERTIES OF UNDULATOR RADIATION: CLASSICAL AND QUANTUM EFFECTS

A DISSERTATION SUBMITTED TO
THE FACULTY OF THE DIVISION OF THE PHYSICAL SCIENCES
IN CANDIDACY FOR THE DEGREE OF
DOCTOR OF PHILOSOPHY

DEPARTMENT OF PHYSICS

BY
IHAR LOBACH

CHICAGO, ILLINOIS
DECEMBER 2021

TABLE OF CONTENTS

LIST OF FIGURES

LIST OF TABLES

ACKNOWLEDGMENTS

I am very thankful to my thesis advisors Prof. Sergei Nagaitsev (UChicago/Fermilab) and Dr. Giulio Stancari (Fermilab) for their support and guidance during my research work at Fermilab. Sergei helped identify research opportunities for my dissertation. He guided me through the research process, while also leaving room to originate with my own ideas. His unique ability to see the big picture and, at the same time, to be able to give advice about low-level theoretical and technical challenges was extremely helpful. Giulio instilled meticulous attention to detail in me. He taught me best practices of planning and conducting an experiment, building a data acquisition system, collecting, storing and processing data, drawing unbiased conclusions from it.

I am grateful to many people at FAST/IOTA who contributed to building the experimental apparatus and taking measurements, especially Aleksandr Romanov, Mark Obrycki, James Santucci, Wayne Johnson, Dean Edstrom, and Kermit Carlson. Greg Saewert constructed the photodiode detection circuit and provided the test light source. Brian Fellenz, Daniil Frolov, David Johnson, and Todd Johnson provided some equipment and assisted during the detector tests. I had useful discussions about the theoretical description with Valeri Lebedev, Alexander Valishev, Kwang-Je Kim (UChicago/ANL), and our collaborators from SLAC — Aliaksei Halavanau and Zhirong Huang — who also kindly provided the undulator. Steve Benson designed the stand for the undulator. Lucy Nobrega led the installation process.

This work was completed in part with resources provided by the University of Chicago Research Computing Center. This research is supported by the University of Chicago and the US Department of Energy under contracts DE-AC02-76SF00515 and DE-AC02-06CH11357. This manuscript has been authored by Fermi Research Alliance, LLC under Contract No. DE-AC02-07CH11359 with the U.S. Department of Energy, Office of Science, Office of High Energy Physics.

ABSTRACT

This dissertation presents two experiments studying the statistical properties of the undulator radiation in the Integrable Optics Test Accelerator (IOTA) storage ring at Fermilab.

The first experiment studies the turn-to-turn fluctuations in the power of the radiation generated by an electron bunch (1–3 billion electrons). Generally, these turn-to-turn fluctuations depend on the full 6D phase-space distribution of the electron bunch. This effect is related to the interference of fields radiated by different electrons. Changes in the relative electron positions and velocities inside the bunch result in fluctuations in the total emitted energy per pass in a synchrotron radiation source. This dissertation presents the most complete (to date) theoretical description of this effect. The experiment in IOTA confirms that the fluctuations depend on the shape, size, and angular divergence of the electron bunch. It reveals the possibility to measure some electron bunch parameters via the fluctuations. The bunch length has been measured by this method in previous experiments. In IOTA, it is shown that it is also possible to measure some transverse properties of the electron bunch distribution (size, angular divergence). This non-invasive electron beam diagnostic technique may be particularly beneficial for the existing and next-generation low-emittance high-brightness ultraviolet and x-ray synchrotron light sources.

The second experiment studies the photon statistics of the undulator radiation generated by a single electron circulating in the ring. When there is only one electron, any classical interference-related collective effects are eliminated, and the quantum fluctuations can be studied in detail. In this experiment, on average, there is only one photocount per several hundred revolutions. The collected data are analyzed to find possible deviations from the expected Poisson process exhibiting uncorrelated detection events. In addition, the arrival times of the photocounts are used to track the longitudinal motion of the single electron and to compare it with the simulation. This allows to determine several useful parameters of the storage ring.

CHAPTER 1

INTRODUCTION

The x-ray synchrotrons and free-electron lasers (FELs, [1]) opened a new era in the investigation of matter on the angstrom length scale and with time resolution on the order of femtoseconds. The synchrotron radiation of highest quality is currently obtained using the undulator — a sequence of magnets with alternating polarities, see Fig. 1.1. The magnetic field in this insertion device forces the electron to wiggle from side to side as it travels through the undulator. The synchrotron radiation generated along the entire undulator length is emitted in approximately the same direction, as opposed to the bending-magnet radiation, where the radiation fields produced in different regions of the dipole magnet travel in significantly different directions and cannot be focused on the target simultaneously. In addition, due to the periodicity of the undulator, at certain wavelengths, the fields produced in different periods can add up constructively. As a result, the spectral intensity distribution of the undulator radiation is represented by a narrow peak [2, p.34] (the fundamental) and harmonics of it, as opposed to a very wide spectral intensity distribution of the bending-magnet (or wiggler) radiation.

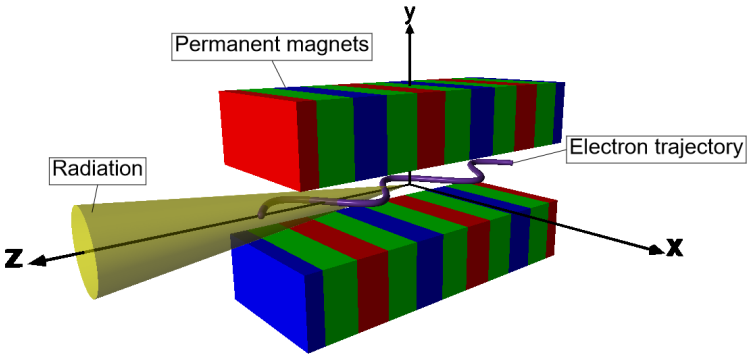

Figure 1.1: Illustration of an undulator, the electron trajectory in the undulator, and the undulator radiation cone.

The x-ray undulator radiation is used in numerous areas of research, such as biology, chemistry, materials science, and medicine. It allows to study atomic details of viruses

(including COVID-19), film chemical reactions [3, 4], decipher the structure of proteins and other macromolecules. In particular, solving the structure of the ribosome [5] earned the Nobel Prize in Chemistry in 2009 [6]. The intense x-ray radiation produced in FELs even allows to study the processes in the interior of planets [7].

Examples of existing or planned x-ray FELs and synchrotrons include LCLS [8] and LCLS-II [9] at SLAC, European XFEL [4] at DESY, SACLA [10] in Japan, APS [11] (and APS-Upgrade) at Argonne, and Swiss FEL [12]. These are large machines (e.g., European XFEL is 3.4 km long) with construction costs reaching or even exceeding a billion dollars. Because of the very limited number of such machines, they are booked for experiments by the users for months or years in advance. Due to these reasons, it is crucial to understand the properties of the electron bunches and the generated synchrotron radiation in these machines very well, including the statistical properties of the radiation.

In the past few decades, a substantial progress has been made in understanding the statistical properties of synchrotron radiation. The turn-to-turn intensity fluctuations of incoherent spontaneous bending-magnet, wiggler, and undulator radiation in storage rings have been studied in Refs. [13–18], both theoretically and experimentally. The statistical properties of the free-electron laser radiation have been studied in Refs. [19–25]. Nevertheless, to this day, people are mostly interested in pulse-by-pulse average properties of synchrotron radiation, such as the total radiated power, spectral composition, angular intensity distribution and brightness [2]. The predictions of classical electrodynamics for these pulse-by-pulse average characteristics are supported by countless observations. In fact, they are confirmed every day by routine operations of synchrotron radiation user facilities around the world. The statistical properties of synchrotron radiation have not been studied to the same level of detail yet. The goal of this dissertation is to try to close this gap and also to point out some possible applications.

This dissertation presents experiments studying the statistical properties of undulator

(a) (b) (c)

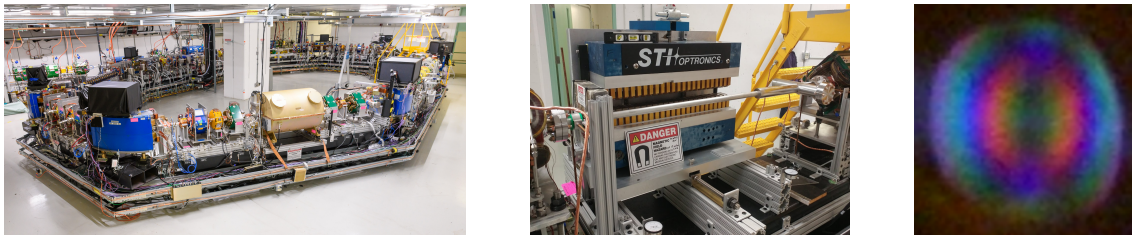

Figure 1.2: (a) Photograph of the IOTA storage ring. Photographed by Giulio Stancari in May 2021. (b) Photograph of the permanent-magnet undulator installed in IOTA on a movable stage. Photographed by the author in February 2019. (c) Photograph of the undulator radiation on the surface of a black screen.

radiation in a storage ring. The relevant theoretical description is presented as well. These experiments took place at the Fermilab's Integrable Optics Test Accelerator (IOTA), see Ref. [26] and Fig. 1.2(a). It is a small 40-meter-circumference storage ring, primarily designed for accelerator science and technology research. This ring can store protons and electrons. To this moment, it has only stored electrons. The main research avenues in the ring are the following: the nonlinear beam optics studies [27–32], the optical stochastic cooling (OSC) experiment [33–38], and the electron lens experiments [39–42]. However, there is also time for other smaller opportunistic experiments, such as the experiments presented in this dissertation.

A short permanent-magnet undulator has been installed in one of the straight sections of the ring, see Fig. 1.2(b). This undulator was borrowed from SLAC. The energy of the electrons was 96.4 MeV. At this energy, the fundamental of the undulator radiation was about 1.16 µm (near-infrared). The second harmonic was in the visible range and could be observed in a regular photograph, see Fig. 1.2(c).

Two experiments were carried out to study the statistical properties of the undulator radiation in IOTA. In the first experiment, there was one electron bunch in the ring, consisting of relatively many electrons (1–3 billion), and the light detector (an InGaAs p-i-n photodiode) was mostly sensitive to the fundamental of the undulator radiation. These

measurements took place during February–April 2019 and during February–March 2020. In the second experiment, there was a single electron (or a few electrons) circulating in the ring. A Single Photon Avalanche Diode (SPAD) detector was used, which was mostly sensitive to the second harmonic of the undulator radiation. These measurements took place during February–March 2020 and during May–July 2021. In both experiments, the turn-by-turn data were collected. The results of these two experiments will be described in Chapters 3 and 4, respectively.

In the first experiment with a bunch of electrons, the idea is to record the number (1–2×10^7) of detected photons at each revolution in the IOTA ring for about 11 thousand consecutive revolutions (1.5 ms). These numbers are not the same, there are small fluctuations with the relative magnitude of about 10^{-4}–10^{-3} (rms). Then, one can calculate the variance of these 11 thousand numbers and systematically study it as a function of the electron bunch parameters (charge, size, shape, angular divergence). Further, it will be shown that it is possible to reverse this procedure and infer some electron bunch parameters using the measured fluctuations of the number of detected photons.

In the second experiment with a single electron, similar turn-by-turn data are collected. However, a photon detection does not occur every turn in this case. On average, it occurs once per several hundred IOTA revolutions. In the first experiment with a bunch of electrons, the fluctuations are dominated by classical effects, related to the interference of the electromagnetic fields produced by different electrons in the bunch. The second experiment with a single electron eliminates any classical effects and allows us to scrutinize the quantum fluctuations of the number of detected photons. This experiment is motivated by the surprizing observation [43, 44] of non-classical sub-Poissonian photon statistics in the seventh coherent spontaneous harmonic of an FEL. Even though it could have been an instrumentation effect [45], it is interesting to carry out a fairly similar experiment in IOTA and see the results. In addition, some measurements are taken with two detectors to study possible

correlation (or anticorrelation) in the detected photon pairs. Lastly, it will be shown that the collected photocount detection times can be used to study the synchrotron motion of a single electron in IOTA.

CHAPTER 2

DERIVATION OF STATISTICAL PROPERTIES OF UNDULATOR RADIATION

The number of photons, radiated by an electron bunch in an external electromagnetic field (undulator, wiggler, bending magnet, etc.), fluctuates from pass to pass due to the following two mechanisms [46]. The first mechanism is the photon shot noise, related to the quantum discrete nature of light. This effect would exist even if there was only one electron circulating in the ring. Indeed, the electron would radiate photons with Poisson statistics [47–49]. The second mechanism is related to the interference of fields radiated by different electrons. Changes in relative electron positions and velocities inside the bunch result in fluctuations in intensity, and, consequently, in the number of photons. In a storage ring, given a constant number of electrons in the bunch, the effect arises because of the betatron motion, synchrotron motion, radiation induced diffusion, etc.; in linacs, there are additionally bunch-to-bunch fluctuations in beam intensity.

For dense bunches, the fluctuations in the number of detected photons are usually dominated by the latter mechanism [2], as was the case in Refs. [13–15, 17, 18]. In this section, a unified description of both mechanisms is presented in the framework of quantum optics. Below, let us consider one electron bunch circulating in a storage ring. The number of electrons in the bunch is assumed to be constant on the time scale of interest. Let us consider the radiation generated in one of the synchrotron radiation sources in the ring, e.g., in an undulator, a wiggler, a bending magnet, etc. Section 2.1 presents our derivation of the equations for the mean and the variance of the number of detected photons for an electron bunch of arbitrary shape and arbitrary degree of coherence of the radiation. These equations assume negligible angular electron beam divergence and energy spread. Section 2.6 discusses several cases, where simple closed-form expressions can be obtained. In Section 2.3, our calculations are compared with the empirical data from the previous experiment carried out at Brookhaven

National Laboratory [13]. Unfortunately, the experiment's parameters are not known to us with sufficient accuracy. Therefore, in Section 2.4, a new experiment in the IOTA storage ring is proposed [16, 50], where all relevant parameters are measured with good accuracy. It will be shown that the angular electron beam divergence cannot be neglected in IOTA and, therefore, the corresponding modifications to the theoretical description are presented in Section 2.5.

2.1 Quantum optics description of the fluctuations of the number of detected photons

Let us assume a detector that can measure the number of detected photons $\mathcal{N}$ during each revolution in a ring. The operator corresponding to this observable will be denoted by $\hat{\mathcal{N}}$. The operation principle of the detector will be discussed later. In this section, the goal is to calculate the average number of detected photons $\langle\mathcal{N}\rangle$ and its turn-to-turn variance $\mathrm{var}(\mathcal{N})$ in the framework of quantum optics. In this consideration, the electromagnetic field of the radiation is quantized. The electrons are classical point-like particles with equal velocities before entering the synchrotron radiation source. Quantitatively, it means that the electron momentum spread σ_p is sufficiently small, so that all of them produce radiation with approximately the same spectrum. Also, it means that the beam divergence is negligible compared to the radiation divergence [2, 17, 51],

$$\sigma_{x'} \ll \sigma_{r,x'}, \quad \sigma_{y'} \ll \sigma_{r,y'}. \tag{2.1}$$

These conditions are satisfied in the experiments reported in Refs. [13, 17, 52], for example.

2.1.1 Density operator formalism

The density operator [48, 53–55] for the radiation is

$$\hat{\rho} = \int \mathrm{d}\xi \; p(\xi) \, |\psi(\xi)\rangle \, \langle\psi(\xi)| \, , \tag{2.2}$$

where $|\psi(\xi)\rangle$ represents the state of the radiation field after the passage of the electron bunch through the synchrotron radiation source. This state is a function of the relative positions of the electrons in the center of the radiator. To signify this let us use the symbol ξ,

$$\xi = (\widetilde{\boldsymbol{r}}_1, \ldots \widetilde{\boldsymbol{r}}_{n_e}), \tag{2.3}$$

$$\mathrm{d}\xi = d\widetilde{\boldsymbol{r}}_1 \ldots d\widetilde{\boldsymbol{r}}_{n_e}, \tag{2.4}$$

where $\widetilde{\boldsymbol{r}}_m = (x_m, y_m, -ct_m)$, here and below vector quantities will be represented by bold symbols; t_m is the time when mth electron passes the center of the light source, x_m and y_m are the transverse coordinates of the mth electron at that moment in time, n_e is the number of electrons in the bunch, $p(\xi)$ is the probability density function for the relative electron positions configuration ξ,

$$\int \mathrm{d}\xi \; p(\xi) = 1. \tag{2.5}$$

In a more general case, ξ should include the velocities of the electrons in the center of the radiation source. This more general case will be considered in Section 2.5. For now the velocities are assumed to be equal.

Let us choose the coordinate system where the z-axis goes along the axis of the undulator (wiggler), and the x- and y-axes are the horizontal and vertical axes in the plane, perpendicular to the z-axis, as illustrated in Fig. 1.1. In a bending magnet, the z-axis can be chosen to point along the radiation traveling towards the detector.

The goal is to find the expressions for the average number of detected photons $\langle \mathcal{N} \rangle$ and for the turn-to-turn variance of $\mathcal{N}$, $\mathrm{var}(\mathcal{N})$. In the density operator formalism [53], these quantities can be obtained as

$$\langle \mathcal{N} \rangle = \mathrm{Tr}\big(\hat{\rho}\hat{\mathcal{N}}\big) = \int \mathrm{d}\xi \; p(\xi) \, \langle \psi(\xi) | \hat{\mathcal{N}} | \psi(\xi) \rangle \, , \tag{2.6}$$

$$\mathrm{var}(\mathcal{N}) = \mathrm{Tr}\big(\hat{\rho}\big(\hat{\mathcal{N}} - \langle \mathcal{N} \rangle\big)^2\big) = \mathrm{Tr}\big(\hat{\rho}\hat{\mathcal{N}}^2\big) - \langle \mathcal{N} \rangle^2 = \int \mathrm{d}\xi \; p(\xi) \, \langle \psi(\xi) | \hat{\mathcal{N}}^2 | \psi(\xi) \rangle - \langle \mathcal{N} \rangle^2 \, . \tag{2.7}$$

This dissertation considers the regime of negligible electron recoil, and, thereby, classical electrons [48, 49]. This is satisfied in all existing storage rings. In this case, according to Ref. [48], the radiation is in the coherent state, also known as the Glauber state. Let us begin by considering the radiation in a cube with a finite side length L and periodic boundary conditions. Hence, there are discrete optical modes with wave-vectors $\boldsymbol{k} = (m, n, l) \times 2\pi/L$, where m, n, l are integers, not equal to zero simultaneously. For each wave-vector $\boldsymbol{k}$, there are two perpendicular polarizations $\boldsymbol{e}_s(\boldsymbol{k})$, $s = 1, 2$. For simplicity, let us consider only one polarization s. In this case, each mode is fully described by its wave-vector $\boldsymbol{k}$. Therefore, instead of carrying the indices m, n, l, it is sufficient to use a single symbol $\boldsymbol{k}$ as an index in a sum (or product) over all optical modes. Similarly, $\boldsymbol{k}$ will be used as a subscript of several functions, quantities, quantum states and operators to indicate which mode they pertain to. In this convention, the coherent state of the radiation field, as a direct product over all the optical modes, is

$$|\psi(\xi)\rangle = \prod_{\boldsymbol{k}} |\alpha_{\boldsymbol{k}}(\xi)\rangle_{\boldsymbol{k}} \, , \tag{2.8}$$

with

$$\Big|\alpha_{\boldsymbol{k}}(\xi)\Big\rangle_{\boldsymbol{k}} = e^{-\frac{1}{2}\left|\alpha_{\boldsymbol{k}}(\xi)\right|^2} \sum_{n_{\boldsymbol{k}}} \frac{\alpha_{\boldsymbol{k}}^{n_{\boldsymbol{k}}}(\xi)}{\sqrt{n_{\boldsymbol{k}}!}} \, |n_{\boldsymbol{k}}\rangle_{\boldsymbol{k}} \, , \tag{2.9}$$

where $|n_{\boldsymbol{k}}\rangle_{\boldsymbol{k}}$ represents the number state (Fock state) of the optical mode with a wave-vector

$\boldsymbol{k}$. According to Ref. [48],

$$\alpha_{\boldsymbol{k}}(\xi) = \frac{1}{\sqrt{2L^3\hbar\omega}} \int \mathrm{d}t\, \mathrm{d}^3\boldsymbol{r}\, \boldsymbol{e}_s(\boldsymbol{k}) \cdot \boldsymbol{j}(\xi, \boldsymbol{r}, t) e^{i\boldsymbol{k}\cdot\boldsymbol{r} - i\omega t}, \tag{2.10}$$

where $\boldsymbol{j}(\xi, \boldsymbol{r}, t)$ represents the current density of the electron bunch with the initial relative arrangement ξ, $\hbar$ is the reduced Planck constant, $\omega = kc$, where c is the speed of light.

The coherent state of each optical mode is the eigenstate of the annihilation operator corresponding to this mode,

$$\hat{a}_{\boldsymbol{k}} \left|\alpha_{\boldsymbol{k}}(\xi)\right\rangle_{\boldsymbol{k}} = \alpha_{\boldsymbol{k}}(\xi) \left|\alpha_{\boldsymbol{k}}(\xi)\right\rangle_{\boldsymbol{k}}. \tag{2.11}$$

The calculation of $\alpha_{\boldsymbol{k}}(\xi)$ is postponed until Section 2.1.3. Discussion of the regime, where both polarization components are registered, will be provided later [see Eq. (2.58)].

2.1.2 Detection operator

The specifics of operation of the chosen light detector determine the form of the operator $\hat{\mathcal{N}}$. This operator has different forms for photodiodes, homodyne detectors, avalanche photodiodes and multiplexed detection schemes with many avalanche photodiodes [53]. In this dissertation, the $\boldsymbol{k}$-dependent (and polarization dependent) quantum efficiency $\eta_{\boldsymbol{k}}$ of a non-ideal detector is considered in the model of a beamsplitter, followed by an ideal detector, see Ref. [54] and Fig. 2.1.

The input-output relations for the beamsplitter take the form [56]

$$\hat{b}_{\boldsymbol{k}} = \sqrt{\eta_{\boldsymbol{k}}}\hat{a}_{\boldsymbol{k}} + i\sqrt{1-\eta_{\boldsymbol{k}}}\hat{c}_{\boldsymbol{k}}, \tag{2.12}$$

$$\hat{d}_{\boldsymbol{k}} = \sqrt{1-\eta_{\boldsymbol{k}}}\hat{c}_{\boldsymbol{k}} + i\sqrt{\eta_{\boldsymbol{k}}}\hat{a}_{\boldsymbol{k}}, \tag{2.13}$$

where $\hat{a}_{\boldsymbol{k}}$ represents the incoming field, $\hat{c}_{\boldsymbol{k}}$ corresponds to the second input port, which

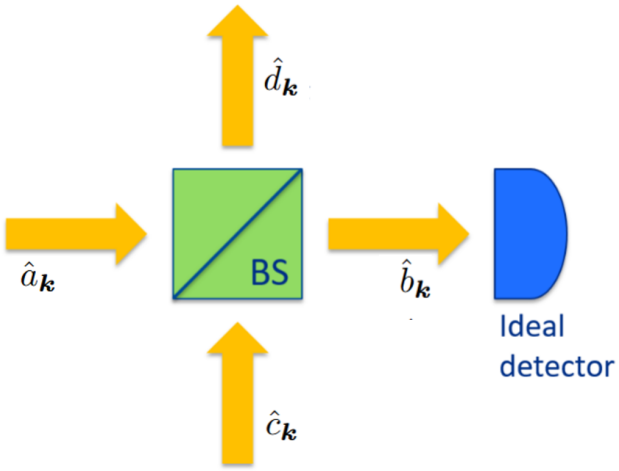

Figure 2.1: The beamsplitter model for quantum efficiency of a non-ideal detector.

is in the vacuum state in this model, $\hat{b}_{\boldsymbol{k}}$ and $\hat{d}_{\boldsymbol{k}}$ are the transmitted and reflected fields, respectively. This model is appropriate for quantum efficiency of a photodiode [53], where the number of detected photons $\mathcal{N}$ is determined as the number of photoelectrons coming from the photodiode. In addition, this model can take into account the spectral transmission of optical filters, lenses, reflectance of mirrors, and detector acceptance.

Further, let us assume that the operator for the total number of detected photons $\hat{\mathcal{N}}$ is a superposition over all modes, i.e.,

$$\hat{\mathcal{N}} = \sum_{\boldsymbol{k}} \hat{b}^{\dagger}_{\boldsymbol{k}} \hat{b}_{\boldsymbol{k}}. \tag{2.14}$$

In this model of the detector, the operator $\hat{\mathcal{N}}$ belongs to the Hilbert space composed of the Hilbert subspaces of both input ports of the beamsplitter. Therefore, the vector state of the radiation $|\psi(\xi)\rangle$ has to be supplemented by the vacuum state of the second input port,

$$|\psi(\xi)\rangle \to |0\rangle_c \, |\psi(\xi)\rangle \,, \tag{2.15}$$

where the subscript c is used to indicate the Hilbert subspace of the second input port. When

the substitution, Eq. (2.15), is carried out in Eqs. (2.6) and (2.7), the expectation values in these equations will take the following form,

$$\langle\psi(\xi)|\hat{\mathcal{N}}|\psi(\xi)\rangle \to \langle\psi(\xi)|\,{}_c\langle 0|\hat{\mathcal{N}}|0\rangle_c\,|\psi(\xi)\rangle\,, \tag{2.16}$$

$$\langle\psi(\xi)|\hat{\mathcal{N}}^2|\psi(\xi)\rangle \to \langle\psi(\xi)|\,{}_c\langle 0|\hat{\mathcal{N}}^2|0\rangle_c\,|\psi(\xi)\rangle\,. \tag{2.17}$$

Therefore, it is necessary to calculate the expectation values ${}_c\langle 0|\hat{\mathcal{N}}|0\rangle_c$ and ${}_c\langle 0|\hat{\mathcal{N}}^2|0\rangle_c$ for the vacuum state of the second input port $|0\rangle_c$. Let us start with ${}_c\langle 0|\hat{\mathcal{N}}|0\rangle_c$. Using Eq. (2.12) in Eq. (2.14) one can obtain

$$\hat{\mathcal{N}} = \sum_{\boldsymbol{k}}\big(\eta_{\boldsymbol{k}}\hat{a}^\dagger_{\boldsymbol{k}}\hat{a}_{\boldsymbol{k}} + i\sqrt{\eta_{\boldsymbol{k}}}\sqrt{1-\eta_{\boldsymbol{k}}}\hat{a}^\dagger_{\boldsymbol{k}}\hat{c}_{\boldsymbol{k}} - i\sqrt{\eta_{\boldsymbol{k}}}\sqrt{1-\eta_{\boldsymbol{k}}}\hat{c}^\dagger_{\boldsymbol{k}}\hat{a}_{\boldsymbol{k}} + (1-\eta_{\boldsymbol{k}})\hat{c}^\dagger_{\boldsymbol{k}}\hat{c}_{\boldsymbol{k}}\big). \tag{2.18}$$

Since only the first term in the parentheses in Eq. (2.18) will provide a nonzero contribution in ${}_c\langle 0|\hat{\mathcal{N}}|0\rangle_c$, one can immediately obtain

$${}_c\langle 0|\hat{\mathcal{N}}|0\rangle_c = \sum_{\boldsymbol{k}}\eta_{\boldsymbol{k}}\hat{a}^\dagger_{\boldsymbol{k}}\hat{a}_{\boldsymbol{k}}. \tag{2.19}$$

The derivation of the expression for ${}_c\langle 0|\hat{\mathcal{N}}^2|0\rangle_c$ is more lengthy,

$$\begin{aligned}
{}_c\langle 0|\hat{\mathcal{N}}^2|0\rangle_c &= {}_c\langle 0|\sum_{\boldsymbol{k}_1}\hat{b}^\dagger_{\boldsymbol{k}_1}\hat{b}_{\boldsymbol{k}_1}\sum_{\boldsymbol{k}_2}\hat{b}^\dagger_{\boldsymbol{k}_2}\hat{b}_{\boldsymbol{k}_2}|0\rangle_c \\
&= {}_c\langle 0|\sum_{\boldsymbol{k}_1,\boldsymbol{k}_2}\big(\eta_{\boldsymbol{k}_1}\hat{a}^\dagger_{\boldsymbol{k}_1}\hat{a}_{\boldsymbol{k}_1} + i\sqrt{\eta_{\boldsymbol{k}_1}}\sqrt{1-\eta_{\boldsymbol{k}_1}}\hat{a}^\dagger_{\boldsymbol{k}_1}\hat{c}_{\boldsymbol{k}_1} - i\sqrt{\eta_{\boldsymbol{k}_1}}\sqrt{1-\eta_{\boldsymbol{k}_1}}\hat{c}^\dagger_{\boldsymbol{k}_1}\hat{a}_{\boldsymbol{k}_1} + (1-\eta_{\boldsymbol{k}_1})\hat{c}^\dagger_{\boldsymbol{k}_1}\hat{c}_{\boldsymbol{k}_1}\big) \\
&\quad \big(\eta_{\boldsymbol{k}_2}\hat{a}^\dagger_{\boldsymbol{k}_2}\hat{a}_{\boldsymbol{k}_2} + i\sqrt{\eta_{\boldsymbol{k}_2}}\sqrt{1-\eta_{\boldsymbol{k}_2}}\hat{a}^\dagger_{\boldsymbol{k}_2}\hat{c}_{\boldsymbol{k}_2} - i\sqrt{\eta_{\boldsymbol{k}_2}}\sqrt{1-\eta_{\boldsymbol{k}_2}}\hat{c}^\dagger_{\boldsymbol{k}_2}\hat{a}_{\boldsymbol{k}_2} + (1-\eta_{\boldsymbol{k}_2})\hat{c}^\dagger_{\boldsymbol{k}_2}\hat{c}_{\boldsymbol{k}_2}\big)|0\rangle_c.
\end{aligned} \tag{2.20}$$

After considering the products of each term from the first parentheses with each term

from the second parentheses in Eq. (2.20), it can be concluded that only the following two will provide nonzero contributions,

$$
\begin{aligned}
{}_c\langle 0|\hat{\mathcal{N}}^2|0\rangle_c &= {}_c\langle 0| \sum_{\boldsymbol{k}_1,\boldsymbol{k}_2} \big(\eta_{\boldsymbol{k}_1}\eta_{\boldsymbol{k}_2}\hat{a}^\dagger_{\boldsymbol{k}_1}\hat{a}_{\boldsymbol{k}_1}\hat{a}^\dagger_{\boldsymbol{k}_2}\hat{a}_{\boldsymbol{k}_2} + \sqrt{\eta_{\boldsymbol{k}_1}(1-\eta_{\boldsymbol{k}_1})\eta_{\boldsymbol{k}_2}(1-\eta_{\boldsymbol{k}_2})}\hat{a}^\dagger_{\boldsymbol{k}_1}\hat{c}_{\boldsymbol{k}_1}\hat{c}^\dagger_{\boldsymbol{k}_2}\hat{a}_{\boldsymbol{k}_2}\big)|0\rangle_c \\
&= \sum_{\boldsymbol{k}_1,\boldsymbol{k}_2} \eta_{\boldsymbol{k}_1}\eta_{\boldsymbol{k}_2}\hat{a}^\dagger_{\boldsymbol{k}_1}(\hat{a}^\dagger_{\boldsymbol{k}_2}\hat{a}_{\boldsymbol{k}_1} + \delta_{\boldsymbol{k}_1,\boldsymbol{k}_2})\hat{a}_{\boldsymbol{k}_2} + \sum_{\boldsymbol{k}} \eta_{\boldsymbol{k}}(1-\eta_{\boldsymbol{k}})\hat{a}^\dagger_{\boldsymbol{k}}\hat{a}_{\boldsymbol{k}} \\
&= \sum_{\boldsymbol{k}_1,\boldsymbol{k}_2} \eta_{\boldsymbol{k}_1}\eta_{\boldsymbol{k}_2}\hat{a}^\dagger_{\boldsymbol{k}_1}\hat{a}^\dagger_{\boldsymbol{k}_2}\hat{a}_{\boldsymbol{k}_1}\hat{a}_{\boldsymbol{k}_2} + \sum_{\boldsymbol{k}} \eta^2_{\boldsymbol{k}}\hat{a}^\dagger_{\boldsymbol{k}}\hat{a}_{\boldsymbol{k}} + \sum_{\boldsymbol{k}} \eta_{\boldsymbol{k}}\hat{a}^\dagger_{\boldsymbol{k}}\hat{a}_{\boldsymbol{k}} - \sum_{\boldsymbol{k}} \eta^2_{\boldsymbol{k}}\hat{a}^\dagger_{\boldsymbol{k}}\hat{a}_{\boldsymbol{k}}, \quad (2.21)
\end{aligned}
$$

where the following commutation relation was used [48],

$$
[\hat{a}_{\boldsymbol{k}_1}, \hat{a}^\dagger_{\boldsymbol{k}_2}] = \delta_{\boldsymbol{k}_1,\boldsymbol{k}_2} = \begin{cases} 1, & \text{if } \boldsymbol{k}_1 = \boldsymbol{k}_2, \\ 0, & \text{otherwise}, \end{cases} \quad (2.22)
$$

and also the fact that

$$
{}_c\langle 0|\hat{c}_{\boldsymbol{k}_1}\hat{c}^\dagger_{\boldsymbol{k}_2}|0\rangle_c = \delta_{\boldsymbol{k}_1,\boldsymbol{k}_2}. \quad (2.23)
$$

After noticing that the second and the forth terms in Eq. (2.21) cancel out, one can arrive at the final expression,

$$
{}_c\langle 0|\hat{\mathcal{N}}^2|0\rangle_c = \sum_{\boldsymbol{k}} \eta_{\boldsymbol{k}}\hat{a}^\dagger_{\boldsymbol{k}}\hat{a}_{\boldsymbol{k}} + \sum_{\boldsymbol{k}_1,\boldsymbol{k}_2} \eta_{\boldsymbol{k}_1}\eta_{\boldsymbol{k}_2}\hat{a}^\dagger_{\boldsymbol{k}_1}\hat{a}^\dagger_{\boldsymbol{k}_2}\hat{a}_{\boldsymbol{k}_2}\hat{a}_{\boldsymbol{k}_1}. \quad (2.24)
$$

The expressions in Eqs. (2.19) and (2.24) are not scalars, they are operators in the Hilbert subspace of the first input port, to which the vector state $|\psi(\xi)\rangle$ belongs.

2.1.3 General expressions for the mean and the variance of the number of detected photons

The expectation values of the operators obtained in Eqs. (2.19) and (2.24) with respect to the vector state $|\psi(\xi)\rangle$, defined in Eq. (2.8), can be calculated by using Eq. (2.11). When the results are used in Eqs. (2.6) and (2.7), the expressions for $\langle\mathcal{N}\rangle$ and $\mathrm{var}(\mathcal{N})$ in the beamsplitter model of the detector take the following form,

$$\langle\mathcal{N}\rangle = \sum_{\boldsymbol{k}} \int \mathrm{d}\xi \; p(\xi)\eta_{\boldsymbol{k}} \left|\alpha_{\boldsymbol{k}}(\xi)\right|^2, \tag{2.25}$$

$$\mathrm{var}(\mathcal{N}) = \langle\mathcal{N}\rangle + \int \mathrm{d}\xi \; p(\xi)\big(\sum_{\boldsymbol{k}} \eta_{\boldsymbol{k}} \left|\alpha_{\boldsymbol{k}}(\xi)\right|^2\big)^2 - \langle\mathcal{N}\rangle^2 . \tag{2.26}$$

Now it is necessary to obtain the expression for $\alpha_{\boldsymbol{k}}(\xi)$. The current density of the electron bunch is

$$\boldsymbol{j}(\xi, \boldsymbol{r}, t) = \sum_m e\boldsymbol{v}_m(t)\delta(\boldsymbol{r}_m(t) - \boldsymbol{r}), \tag{2.27}$$

where $\delta(..)$ is the Dirac delta function, $m = 1, \ldots n_e$; $\boldsymbol{r} = (x, y, z)$ describes the position in space,

$$\boldsymbol{r}_m(t) = (x_m(t), y_m(t), z_m(t)) \tag{2.28}$$

is the trajectory of mth electron [not to be confused with $\widetilde{\boldsymbol{r}}_m = (x_m, y_m, -ct_m)$ from Eq. (2.3)], $\boldsymbol{v}_m(t)$ is the velocity vector of mth electron as a function of time.

Without loss of generality one can choose the electron with $m = 1$ to be the reference electron. To be specific, for this electron, the time of passing the center of the undulator is zero, $t_1 = 0$, and its transverse position at this moment in time is zero as well, $\widetilde{\boldsymbol{r}}_{1\perp} = 0$. Let us assume that in the synchrotron light source under consideration the trajectory of the mth electron is merely the trajectory of the reference electron offset by $\widetilde{\boldsymbol{r}}_{m\perp} = (x_m, y_m, 0)$. It is

usually a good approximation in undulators, wigglers, and bending magnets. In this case,

$$\boldsymbol{j}(\xi, \boldsymbol{r}, t) = \sum_m e\boldsymbol{v}(t - t_m)\delta(\boldsymbol{r}(t - t_m) + \widetilde{\boldsymbol{r}}_{m\perp} - \boldsymbol{r}), \tag{2.29}$$

where the index "1" was dropped in the position vector and the velocity vector of the reference electron for brevity, i.e., $\boldsymbol{r}_1(t - t_m) \to \boldsymbol{r}(t - t_m)$ and $\boldsymbol{v}_1(t - t_m) \to \boldsymbol{v}(t - t_m)$.

By integrating over $\boldsymbol{r}$ in Eq. (2.10) using Eq. (2.29), one can obtain

$$\alpha_{\boldsymbol{k}}(\xi) = \sqrt{\frac{\alpha}{2L^3k}} \sum_m \int \mathrm{d}t \boldsymbol{e}_s(\boldsymbol{k}) \cdot \boldsymbol{v}(t - t_m) \times e^{i\boldsymbol{k}\cdot\boldsymbol{r}(t-t_m) + i\boldsymbol{k}\cdot\widetilde{\boldsymbol{r}}_{m\perp} - i\omega(t-t_m)}, \tag{2.30}$$

where $\alpha = e^2/(\hbar c)$ is the fine-structure constant.

By changing the integration variable from t to $t - t_m$ in each sum term one arrives at

$$\alpha_{\boldsymbol{k}}(\xi) = \sqrt{\frac{\alpha}{2L^3k}} \sum_m e^{i\boldsymbol{k}\cdot\widetilde{\boldsymbol{r}}_{m\perp} - i\omega t_m} \int \mathrm{d}t \boldsymbol{e}_s(\boldsymbol{k}) \cdot \boldsymbol{v}(t) e^{i\boldsymbol{k}\cdot\boldsymbol{r}(t) - i\omega t} = \big(\sum_m e^{i\widetilde{\boldsymbol{k}}\cdot\widetilde{\boldsymbol{r}}_m}\big) \times \alpha^{(1)}_{\boldsymbol{k}}, \tag{2.31}$$

where $\widetilde{\boldsymbol{k}} = (k_x, k_y, k)$, noting that the last component is $k = |\boldsymbol{k}| = \omega/c$, not k_z. The new function $\alpha^{(1)}_{\boldsymbol{k}}$ is calculated only for the reference electron,

$$\alpha^{(1)}_{\boldsymbol{k}} = \sqrt{\frac{\alpha}{2L^3k}} \int \mathrm{d}t \boldsymbol{e}_s(\boldsymbol{k}) \cdot \boldsymbol{v}(t) e^{i\boldsymbol{k}\cdot\boldsymbol{r}(t) - i\omega t}. \tag{2.32}$$

To summarize, assuming a monoenergetic electron bunch with negligible beam divergence [see Eq. (2.1)], the following expression was derived,

$$\alpha_{\boldsymbol{k}}(\xi) = \alpha^{(1)}_{\boldsymbol{k}} \times \sum_m e^{i\widetilde{\boldsymbol{k}}\cdot\widetilde{\boldsymbol{r}}_m}, \tag{2.33}$$

where $\alpha^{(1)}_{\boldsymbol{k}}$ is given by Eq. (2.32) and calculated only for the reference electron; $\widetilde{\boldsymbol{r}}_m = (x_m, y_m, -ct_m)$, where x_m and y_m are the transverse positions of mth electron (relative to

the reference electron) when mth electron passes through the center of the light source at the moment in time t_m. Similar calculations have been presented in [2, 17, 51].

At this point, one can take the limit $L \to \infty$ and transition from discrete to continuos optical modes. As a replacement for $\alpha_{\boldsymbol{k}}^{(1)}$ in this limit, one can introduce a continuous function $\mathcal{E}_{\boldsymbol{k}}$ of a continuous variable $\boldsymbol{k}$ in the following way

$$\mathcal{E}_{\boldsymbol{k}} = \sqrt{\frac{\alpha k}{2(2\pi)^3}} \int \mathrm{d}t \, \boldsymbol{e}_s(\boldsymbol{k}) \cdot \boldsymbol{v}(t) e^{i\boldsymbol{k}\cdot\boldsymbol{r}(t) - i\omega t}. \tag{2.34}$$

The square of the magnitude of $\mathcal{E}_{\boldsymbol{k}}$ describes the photon flux produced by a single electron (s.e.) in the direction of the wave-vector $\boldsymbol{k}$, i.e., for the number of detected photons one can write

$$\frac{\mathrm{d}^3 \langle \mathcal{N}_{\text{s.e.}} \rangle}{\mathrm{d}k \, \mathrm{d}^2\Omega} = \eta_{\boldsymbol{k}} \left| \mathcal{E}_{\boldsymbol{k}} \right|^2, \tag{2.35}$$

where $\mathrm{d}^2\Omega$ is the element of solid angle around the direction of $\boldsymbol{k}$. The expression for $\mathcal{E}_{\boldsymbol{k}}$ for the undulator radiation will be presented in Section 2.2. For now, let us assume an arbitrary synchrotron light source.

It will be necessary to work with the complex function $\mathcal{E}_{\boldsymbol{k}}$ in Section 2.5. In the current section, however, only $\left|\alpha_{\boldsymbol{k}}^{(1)}\right|^2$ will be encountered (and, therefore, only $|\mathcal{E}_{\boldsymbol{k}}|^2$). Therefore, to slightly simplify further derivations, let us introduce the "intensity" function for one electron $I_{\boldsymbol{k}}^{(1)}$ as

$$I_{\boldsymbol{k}}^{(1)} = \frac{|\mathcal{E}_{\boldsymbol{k}}|^2}{k^2}. \tag{2.36}$$

Then, in the limit $L \to \infty$, any sum over discrete optical modes in the current section can be turned into an integral by the following simple substitution,

$$\left|\alpha_{\boldsymbol{k}}^{(1)}\right|^2 \to I_{\boldsymbol{k}}^{(1)} \, \mathrm{d}^3\boldsymbol{k}\,. \tag{2.37}$$

Then, Eqs. (2.25) and (2.26) become, respectively,

$$\langle \mathcal{N} \rangle = \int \mathrm{d}^3\boldsymbol{k}\, \eta_{\boldsymbol{k}} I^{(1)}_{\boldsymbol{k}} \int \mathrm{d}\xi\; p(\xi) \mathcal{J}_{\boldsymbol{k}}(\xi), \tag{2.38}$$

$$\mathrm{var}(\mathcal{N}) = \langle \mathcal{N} \rangle + \int \mathrm{d}^3\boldsymbol{k}_1\, \mathrm{d}^3\boldsymbol{k}_2\, \eta_{\boldsymbol{k}_1} I^{(1)}_{\boldsymbol{k}_1} \eta_{\boldsymbol{k}_2} I^{(1)}_{\boldsymbol{k}_2} \int \mathrm{d}\xi\; p(\xi) \mathcal{J}_{\boldsymbol{k}_1}(\xi) \mathcal{J}_{\boldsymbol{k}_2}(\xi) - \langle \mathcal{N} \rangle^2 , \tag{2.39}$$

where a new function was introduced,

$$\mathcal{J}_{\boldsymbol{k}}(\xi) \equiv \left| \sum_m e^{i\widetilde{\boldsymbol{k}}\cdot\widetilde{\boldsymbol{r}}_m} \right|^2 . \tag{2.40}$$

Henceforth, let us consider an electron bunch, where the positions of the electrons are independent random variables with identical probability density functions, i.e.,

$$p(\xi) = p(\widetilde{\boldsymbol{r}}_1) \ldots p(\widetilde{\boldsymbol{r}}_{n_e}). \tag{2.41}$$

The function $\mathcal{J}_{\boldsymbol{k}}(\xi)$ can be represented in the following form,

$$\begin{aligned} \mathcal{J}_{\boldsymbol{k}}(\xi) = \sum_m e^{i\widetilde{\boldsymbol{k}}\cdot\widetilde{\boldsymbol{r}}_m} \sum_n e^{-i\widetilde{\boldsymbol{k}}\cdot\widetilde{\boldsymbol{r}}_n} &= \sum_{m,n} e^{i\widetilde{\boldsymbol{k}}\cdot(\widetilde{\boldsymbol{r}}_m - \widetilde{\boldsymbol{r}}_n)} \\ &= \sum_m 1 + \sum_{m\neq n} e^{i\widetilde{\boldsymbol{k}}\cdot(\widetilde{\boldsymbol{r}}_m - \widetilde{\boldsymbol{r}}_n)} = n_e + \sum_{m\neq n} e^{i\widetilde{\boldsymbol{k}}\cdot(\widetilde{\boldsymbol{r}}_m - \widetilde{\boldsymbol{r}}_n)}. \end{aligned} \tag{2.42}$$

Therefore, the integral over ξ in Eq. (2.38) can be calculated as

$$\begin{aligned} &\int \mathrm{d}\xi\; p(\xi) \mathcal{J}_{\boldsymbol{k}}(\xi) = n_e + \int \mathrm{d}\xi\; p(\xi) \sum_{m\neq n} e^{i\widetilde{\boldsymbol{k}}\cdot(\widetilde{\boldsymbol{r}}_m - \widetilde{\boldsymbol{r}}_n)} \\ &= n_e + \sum_{m\neq n} \int p(\widetilde{\boldsymbol{r}}_m) e^{i\widetilde{\boldsymbol{k}}\cdot\widetilde{\boldsymbol{r}}_m}\, \mathrm{d}^3\widetilde{\boldsymbol{r}}_m \int p(\widetilde{\boldsymbol{r}}_n) e^{-i\widetilde{\boldsymbol{k}}\cdot\widetilde{\boldsymbol{r}}_n}\, \mathrm{d}^3\widetilde{\boldsymbol{r}}_n = n_e + n_e\,(n_e - 1) \left| \mathcal{P}\left(\widetilde{\boldsymbol{k}}\right) \right|^2 , \end{aligned} \tag{2.43}$$

where the multiplier $n_e\,(n_e - 1)$ comes from the sum over m and n from 1 to n_e, ignoring

the diagonal terms, where $m = n$. Also, the following function was introduced,

$$\mathcal{P}\left(\widetilde{\boldsymbol{k}}\right) \equiv \int p(\widetilde{\boldsymbol{r}}) e^{i\widetilde{\boldsymbol{k}}\cdot\widetilde{\boldsymbol{r}}}\, \mathrm{d}^3\widetilde{\boldsymbol{r}}\,. \tag{2.44}$$

To summarize, the final expression for $\langle \mathcal{N} \rangle$ takes the form

$$\langle \mathcal{N} \rangle = n_e \int \mathrm{d}^3\boldsymbol{k}\, \eta_{\boldsymbol{k}} I^{(1)}_{\boldsymbol{k}} \big(1 + (n_e - 1)\left|\mathcal{P}\left(\widetilde{\boldsymbol{k}}\right)\right|^2\big). \tag{2.45}$$

Now let us obtain the expression for $\mathrm{var}(\mathcal{N})$. The calculation of the integral over ξ in Eq. (2.39) is lengthy. One can start by using the following relation in Eq. (2.39),

$$\begin{aligned}
\mathcal{J}_{\boldsymbol{k}_1}(\xi)\mathcal{J}_{\boldsymbol{k}_2}(\xi) &= \left|\sum_m e^{i\widetilde{\boldsymbol{k}}_1\cdot\widetilde{\boldsymbol{r}}_m}\right|^2 \left|\sum_n e^{i\widetilde{\boldsymbol{k}}_2\cdot\widetilde{\boldsymbol{r}}_n}\right|^2 \\
&= \left(n_e + \sum_{m\neq n} e^{i\widetilde{\boldsymbol{k}}_1\cdot(\widetilde{\boldsymbol{r}}_m - \widetilde{\boldsymbol{r}}_n)}\right)\left(n_e + \sum_{i\neq j} e^{-i\widetilde{\boldsymbol{k}}_2\cdot(\widetilde{\boldsymbol{r}}_i - \widetilde{\boldsymbol{r}}_j)}\right) \\
&= n_e^2 + n_e \sum_{m\neq n} e^{i\widetilde{\boldsymbol{k}}_1\cdot(\widetilde{\boldsymbol{r}}_m - \widetilde{\boldsymbol{r}}_n)} + n_e \sum_{i\neq j} e^{-i\widetilde{\boldsymbol{k}}_2\cdot(\widetilde{\boldsymbol{r}}_i - \widetilde{\boldsymbol{r}}_j)} + \sum_{m\neq n} e^{i\left(\widetilde{\boldsymbol{k}}_1 - \widetilde{\boldsymbol{k}}_2\right)\cdot(\widetilde{\boldsymbol{r}}_m - \widetilde{\boldsymbol{r}}_n)} \\
&\qquad + \sum_{\substack{m\neq n, i\neq j \\ m,n\neq i,j}} e^{i\widetilde{\boldsymbol{k}}_1(\widetilde{\boldsymbol{r}}_m - \widetilde{\boldsymbol{r}}_n) - i\widetilde{\boldsymbol{k}}_2(\widetilde{\boldsymbol{r}}_i - \widetilde{\boldsymbol{r}}_j)}.
\end{aligned} \tag{2.46}$$

Then, the next step is to multiply each term of Eq. (2.46) by $p(\xi)$ and integrate over ξ. The integral of the first term in Eq. (2.46) is trivial. The second, third and fourth terms have the same form as Eq. (2.43). Therefore, let us simply provide the results,

$$\int \mathrm{d}\xi\; p(\xi) n_e \sum_{m\neq n} e^{i\widetilde{\boldsymbol{k}}_1\cdot(\widetilde{\boldsymbol{r}}_m - \widetilde{\boldsymbol{r}}_n)} = n_e^2(n_e - 1)\left|\mathcal{P}\left(\widetilde{\boldsymbol{k}}_1\right)\right|^2, \tag{2.47}$$

$$\int \mathrm{d}\xi\; p(\xi) n_e \sum_{i\neq j} e^{-i\widetilde{\boldsymbol{k}}_2\cdot(\widetilde{\boldsymbol{r}}_i - \widetilde{\boldsymbol{r}}_j)} = n_e^2(n_e - 1)\left|\mathcal{P}\left(\widetilde{\boldsymbol{k}}_2\right)\right|^2, \tag{2.48}$$

$$\int \mathrm{d}\xi\ p(\xi) \sum_{m\neq n} e^{i\left(\widetilde{\boldsymbol{k}}_1-\widetilde{\boldsymbol{k}}_2\right)\cdot(\widetilde{\boldsymbol{r}}_m-\widetilde{\boldsymbol{r}}_n)} = n_e(n_e-1)\left|\mathcal{P}\left(\widetilde{\boldsymbol{k}}_1-\widetilde{\boldsymbol{k}}_2\right)\right|^2. \tag{2.49}$$

The fifth (last) term has to be considered separately. It can be represented in the following form,

$$\sum_{\substack{m\neq n, i\neq j\\ m,n\neq i,j}} e^{i\widetilde{\boldsymbol{k}}_1(\widetilde{\boldsymbol{r}}_m-\widetilde{\boldsymbol{r}}_n)-i\widetilde{\boldsymbol{k}}_2(\widetilde{\boldsymbol{r}}_i-\widetilde{\boldsymbol{r}}_j)} = A_1(\xi)+A_2(\xi)+A_3(\xi), \tag{2.50}$$

where

$$A_1(\xi) = \sum_{\substack{m\neq n\\ j\neq n\\ j\neq m}} e^{i(\widetilde{\boldsymbol{k}}_1-\widetilde{\boldsymbol{k}}_2)\cdot\widetilde{\boldsymbol{r}}_m-i\widetilde{\boldsymbol{k}}_1\cdot\widetilde{\boldsymbol{r}}_n+i\widetilde{\boldsymbol{k}}_2\cdot\widetilde{\boldsymbol{r}}_j}, \tag{2.51}$$

$$A_2(\xi) = \sum_{\substack{m\neq n\\ i\neq n\\ i\neq m}} e^{-i(\widetilde{\boldsymbol{k}}_1-\widetilde{\boldsymbol{k}}_2)\cdot\widetilde{\boldsymbol{r}}_n+i\widetilde{\boldsymbol{k}}_1\cdot\widetilde{\boldsymbol{r}}_m-i\widetilde{\boldsymbol{k}}_2\cdot\widetilde{\boldsymbol{r}}_i}, \tag{2.52}$$

$$A_3(\xi) = \sum_{\substack{m\neq n\\ i\neq j\\ i\neq m\\ j\neq n}} e^{i\widetilde{\boldsymbol{k}}_1\cdot(\widetilde{\boldsymbol{r}}_m-\widetilde{\boldsymbol{r}}_n)-i\widetilde{\boldsymbol{k}}_2\cdot(\widetilde{\boldsymbol{r}}_i-\widetilde{\boldsymbol{r}}_j)}. \tag{2.53}$$

Integration of Eq. (2.50) is analogous to Eq. (2.43), with the exception that counting the terms in the sums is more difficult. Omitting the details,

$$\int \mathrm{d}\xi\ p(\xi)A_1(\xi) = \left(\int \mathrm{d}\xi\ p(\xi)A_2(\xi)\right)^* = n_e\,(n_e-1)\,(n_e-2)\,\mathcal{P}\left(\widetilde{\boldsymbol{k}}_1-\widetilde{\boldsymbol{k}}_2\right)\mathcal{P}^*\left(\widetilde{\boldsymbol{k}}_1\right)\mathcal{P}\left(\widetilde{\boldsymbol{k}}_2\right), \tag{2.54}$$

$$\int \mathrm{d}\xi\ p(\xi)A_3(\xi) = n_e\,(n_e-1)\left(n_e^2-3n_e+3\right)\left|\mathcal{P}\left(\widetilde{\boldsymbol{k}}_1\right)\mathcal{P}\left(\widetilde{\boldsymbol{k}}_2\right)\right|^2. \tag{2.55}$$

When Eqs. (2.47) to (2.49), (2.54), and (2.55) are used together with Eq. (2.46) to calculate the integral over ξ in Eq. (2.39), one arrives at

$$\int \mathrm{d}\xi\; p(\xi)\mathcal{J}_{\boldsymbol{k}_1}(\xi)\mathcal{J}_{\boldsymbol{k}_2}(\xi) = n_e^2 + n_e(n_e-1)\left|\mathcal{P}\big(\widetilde{\boldsymbol{k}}_1-\widetilde{\boldsymbol{k}}_2\big)\right|^2 + n_e(n_e-1)\Bigg[n_e\Big(\left|\mathcal{P}\big(\widetilde{\boldsymbol{k}}_1\big)\right|^2+\left|\mathcal{P}\big(\widetilde{\boldsymbol{k}}_2\big)\right|^2\Big) + (n_e-2)\left(\mathcal{P}\big(\widetilde{\boldsymbol{k}}_1-\widetilde{\boldsymbol{k}}_2\big)\mathcal{P}^*\big(\widetilde{\boldsymbol{k}}_1\big)\mathcal{P}\big(\widetilde{\boldsymbol{k}}_2\big)+c.c.\right) + \Big(n_e^2-3n_e+3\Big)\left|\mathcal{P}\big(\widetilde{\boldsymbol{k}}_1\big)\mathcal{P}\big(\widetilde{\boldsymbol{k}}_2\big)\right|^2\Bigg]. \quad (2.56)$$

Finally, by using Eqs. (2.45) and (2.56) in Eq. (2.39), one can obtain the final expression for $\mathrm{var}(\mathcal{N})$,

$$\mathrm{var}(\mathcal{N}) = \langle\mathcal{N}\rangle + n_e(n_e-1)\int \mathrm{d}^3\boldsymbol{k}_1\,\mathrm{d}^3\boldsymbol{k}_2\,\eta_{\boldsymbol{k}_1}I^{(1)}_{\boldsymbol{k}_1}\eta_{\boldsymbol{k}_2}I^{(1)}_{\boldsymbol{k}_2}\Bigg[\left|\mathcal{P}\big(\widetilde{\boldsymbol{k}}_1-\widetilde{\boldsymbol{k}}_2\big)\right|^2-\left|\mathcal{P}\big(\widetilde{\boldsymbol{k}}_1\big)\mathcal{P}\big(\widetilde{\boldsymbol{k}}_2\big)\right|^2 + (n_e-2)\Big[\mathcal{P}^*\big(\widetilde{\boldsymbol{k}}_1\big)\mathcal{P}\big(\widetilde{\boldsymbol{k}}_2\big)\Big(\mathcal{P}\big(\widetilde{\boldsymbol{k}}_1-\widetilde{\boldsymbol{k}}_2\big)-\mathcal{P}\big(\widetilde{\boldsymbol{k}}_1\big)\mathcal{P}^*\big(\widetilde{\boldsymbol{k}}_2\big)\Big)+c.c.\Big]\Bigg]. \quad (2.57)$$

Equations (2.45) and (2.57) are the most general results of this section. They apply to any degree of coherence of the radiation (both transverse and temporal), for any number of the electrons in the bunch n_e, and for any probability density function of each electron $p(\widetilde{\boldsymbol{r}})$. If both polarization components are registered by the detector, the following substitution should be performed,

$$\eta_{\boldsymbol{k}}I^{(1)}_{\boldsymbol{k}} \rightarrow \sum_{s=1,2}\eta_{\boldsymbol{k},s}I^{(1)}_{\boldsymbol{k},s}. \quad (2.58)$$

In Eq. (2.45), the first term represents incoherent radiation. The second term constitutes coherent synchrotron radiation (CSR). The limit of fully coherent radiation can be obtained by assuming that all the electrons are concentrated in a single point. Using the Dirac delta

function, $p(\widetilde{\boldsymbol{r}}) = \delta(\widetilde{\boldsymbol{r}})$. In this limit, for any $\widetilde{\boldsymbol{k}}$,

$$\mathcal{P}\left(\widetilde{\boldsymbol{k}}\right) = 1, \tag{2.59}$$

and in Eq. (2.45) one can obtain the expected result, that the intensity scales as n_e^2.

In Eq. (2.57), the first term, namely, $\langle \mathcal{N} \rangle$, is the photon shot noise contribution. It exists even in the case of a single electron, $n_e = 1$. The second term arises from the variations in the relative positions of the classical point-like electrons in the bunch. It vanishes in the case of fully coherent radiation, as one can see by inserting Eq. (2.59) in Eq. (2.57). However, it is nonzero in the case of incoherent or partially coherent radiation. Therefore, henceforth, this term may be called the incoherence contribution to the fluctuations.

In Section 2.1.5, possible simplifications of Eqs. (2.45) and (2.57) will be considered in the case of temporally incoherent radiation. However, before that, one special example will be considered in Section 2.1.4, namely, the Gaussian electron bunch. In the case of a Gaussian electron bunch, a closed-form expression can be obtained for the function $\mathcal{P}\left(\widetilde{\boldsymbol{k}}\right)$ at arbitrary degree of coherence.

2.1.4 Gaussian electron bunch example. Arbitrary degree of coherence. Negligible electron beam divergence

In this section, the form of Eqs. (2.45) and (2.57) will be provided for a Gaussian electron bunch, where each electron has the probability density function

$$p(\widetilde{\boldsymbol{r}}) = \frac{1}{(2\pi)^{3/2}\,\sigma_x \sigma_y c\sigma_t} \exp\left(-\frac{x^2}{2\sigma_x^2} - \frac{y^2}{2\sigma_y^2} - \frac{(ct)^2}{2(c\sigma_t)^2} \right). \tag{2.60}$$

In this case, the integration over $\widetilde{\boldsymbol{r}}$ in Eq. (2.44) can be performed by using the Hub-

bard–Stratonovich identity [57]. The results are

$$\langle \mathcal{N} \rangle = n_e \int \mathrm{d}^3\boldsymbol{k}\, \eta_{\boldsymbol{k}} I^{(1)}_{\boldsymbol{k}} \big(1 + (n_e - 1)\, e^{-\mathbf{K}\cdot\boldsymbol{\Sigma}}\big), \tag{2.61}$$

where $\mathbf{K} \equiv (k_x^2, k_y^2, k^2)$, $\boldsymbol{\Sigma} \equiv (\sigma_x^2, \sigma_y^2, c^2\sigma_t^2)$,

$$\mathrm{var}(\mathcal{N}) = \langle \mathcal{N} \rangle + n_e(n_e-1) \int \mathrm{d}^3\boldsymbol{k}_1\, \mathrm{d}^3\boldsymbol{k}_2\, \eta_{\boldsymbol{k}_1} I^{(1)}_{\boldsymbol{k}_1} \eta_{\boldsymbol{k}_2} I^{(1)}_{\boldsymbol{k}_2} \Big[\Delta^2 - \Sigma^2 + 2(n_e-2)\Sigma(\Sigma-\Delta)\Big], \tag{2.62}$$

where

$$\Delta = e^{-\frac{1}{2}\boldsymbol{\Delta}_{12}\cdot\boldsymbol{\Sigma}}, \quad \Sigma = e^{-\frac{1}{2}\mathbf{K}_{12}\cdot\boldsymbol{\Sigma}}, \tag{2.63}$$

$$\boldsymbol{\Delta}_{12} = ((k_{1x} - k_{2x})^2, (k_{1y} - k_{2y})^2, (k_1 - k_2)^2), \tag{2.64}$$

$$\mathbf{K}_{12} = (k_{1x}^2 + k_{2x}^2, k_{1y}^2 + k_{2y}^2, k_1^2 + k_2^2). \tag{2.65}$$

2.1.5 Regime of temporal incoherence

In this section, the regime of temporally incoherent radiation will be considered,

$$\omega\sigma_t \gg 1, \tag{2.66}$$

where σ_t is the rms bunch duration. It will be shown that Eq. (2.57) agrees with the results obtained in [17], where this less general regime was studied classically.

Given Eq. (2.66), the integrals of the form of Eq. (2.44) with the arguments $\widetilde{\boldsymbol{k}}_1$ and $\widetilde{\boldsymbol{k}}_2$ will be negligible due to the fast oscillations of the phase factor. Only the integral with the argument $\widetilde{\boldsymbol{k}}_1 - \widetilde{\boldsymbol{k}}_2$ will result in a non-vanishing contribution. Therefore,

$$\langle \mathcal{N} \rangle = n_e \int \mathrm{d}^3\boldsymbol{k}\, \eta_{\boldsymbol{k}} I^{(1)}_{\boldsymbol{k}}, \tag{2.67}$$

$$\mathrm{var}(\mathcal{N}) = \langle \mathcal{N} \rangle + n_e(n_e - 1) \int \mathrm{d}^3\boldsymbol{k}_1 \, \mathrm{d}^3\boldsymbol{k}_2 \, \eta_{\boldsymbol{k}_1} I^{(1)}_{\boldsymbol{k}_1} \eta_{\boldsymbol{k}_2} I^{(1)}_{\boldsymbol{k}_2} \left| \mathcal{P}\left(\widetilde{\boldsymbol{k}}_1 - \widetilde{\boldsymbol{k}}_2\right) \right|^2 . \tag{2.68}$$

Following the notation of [13, 17] and [2, p. 28], Eq. (2.68) can be rewritten as

$$\mathrm{var}(\mathcal{N}) = \langle \mathcal{N} \rangle + \frac{1}{M} \langle \mathcal{N} \rangle^2 , \tag{2.69}$$

where the parameter M was introduced. In this dissertation, M is defined by Eq. (2.69). Then, according to Eqs. (2.67) and (2.68), it follows that

$$\frac{1}{M} \equiv (1 - 1/n_e) \frac{\int \mathrm{d}^3\boldsymbol{k}_1 \, \mathrm{d}^3\boldsymbol{k}_2 \, \eta_{\boldsymbol{k}_1} I^{(1)}_{\boldsymbol{k}_1} \eta_{\boldsymbol{k}_2} I^{(1)}_{\boldsymbol{k}_2} \left| \mathcal{P}\left(\widetilde{\boldsymbol{k}}_1 - \widetilde{\boldsymbol{k}}_2\right) \right|^2}{\left(\int \mathrm{d}^3\boldsymbol{k} \, \eta_{\boldsymbol{k}} I^{(1)}_{\boldsymbol{k}} \right)^2} . \tag{2.70}$$

However, this parameter can be identified with the number of coherent modes, defined in [2, 51, 58, 59]. Therefore, let us use this name for the parameter M from now on. Equation (2.70) is in agreement with Eq. (14) of Ref. [17], which was derived for a relative fluctuation of classical radiation intensity.

Equation (2.66) is satisfied, for example, in the Brookhaven experiment [13] and in our experiments in IOTA [16, 50, 60]. In both cases, $\omega\sigma_t \sim 10^6$.

There is one more possible simplification, which can be used for the above mentioned experiments. If the probability function can be factorized into temporal and transverse components,

$$p(\widetilde{\boldsymbol{r}}) = p_t(t) p_\perp(\widetilde{\boldsymbol{r}}_\perp), \tag{2.71}$$

then,

$$\mathcal{P}\left(\widetilde{\boldsymbol{k}}_1 - \widetilde{\boldsymbol{k}}_2\right) = \mathcal{P}_t(k_1 - k_2) \mathcal{P}_\perp(\boldsymbol{k}_1 - \boldsymbol{k}_2), \tag{2.72}$$

with

$$\mathcal{P}_t(k_1 - k_2) = \int p_t(t) e^{ic(k_1 - k_2)t} \mathrm{d}t, \tag{2.73}$$

$$\mathcal{P}_\perp(\boldsymbol{k}_1 - \boldsymbol{k}_2) = \int p_\perp(\widetilde{\boldsymbol{r}}_\perp) e^{i(\boldsymbol{k}_1 - \boldsymbol{k}_2)\cdot\widetilde{\boldsymbol{r}}_\perp} \, \mathrm{d}^2\widetilde{\boldsymbol{r}}_\perp \,, \tag{2.74}$$

where

$$\widetilde{\boldsymbol{r}}_\perp = (x, y, 0), \qquad\qquad \mathrm{d}^2\widetilde{\boldsymbol{r}}_\perp = \mathrm{d}x\mathrm{d}y. \tag{2.75}$$

The width of $\mathcal{P}_t(k_1 - k_2)$ as a function of $k_1 - k_2$ is of the order of $1/(c\sigma_t)$. If $\mathcal{P}_t(k_1 - k_2)$ is much narrower than any other scale in the problem, such as the width of the radiation spectrum, or the monochromator's FWHM (if used), then the following relation, employing the Dirac delta function, can be used,

$$|\mathcal{P}_t(k_1 - k_2)|^2 = \frac{\sqrt{\pi}}{c\,\sigma_t^{\mathrm{eff}}} \delta(k_1 - k_2), \tag{2.76}$$

where σ_t^{eff} is the effective electron bunch duration, defined as

$$\sigma_t^{\mathrm{eff}} = 1/\big(2\sqrt{\pi} \int p_t^2(t)\,\mathrm{d}t\big). \tag{2.77}$$

For a Gaussian temporal electron bunch distribution, the effective bunch duration σ_t^{eff} is equal to the rms bunch duration

$$\sigma_t = \sqrt{\int t^2\, p_t(t)\,\mathrm{d}t}, \tag{2.78}$$

where it is assumed that $\int t\, p_t(t)\,\mathrm{d}t = 0$.

In practical calculations, it may be more convenient to use units of length for the temporal distribution of the electron bunch. Below in this dissertation, the parameters σ_z and σ_z^{eff}

may be used, which are defined as

$$\sigma_z = c\,\sigma_t, \qquad\qquad \sigma_z^{\rm eff} = c\,\sigma_t^{\rm eff}. \tag{2.79}$$

Strictly speaking, σ_z and $\sigma_z^{\rm eff}$, defined by Eq. (2.79), still refer to the temporal distribution of the electron bunch, simply scaled by a factor of c — the speed of light. However, sometimes σ_z and $\sigma_z^{\rm eff}$ will be called the rms bunch length and the effective bunch length, respectively, because only ultrarelativistic electrons will be encountered in this dissertation, for which it is a very good approximation.

To prove Eq. (2.77), one can start with the following ansatz,

$$|\mathcal{P}_t(k)|^2 = \kappa_t \delta(k). \tag{2.80}$$

Then,

$$\begin{aligned}\kappa_t &= \int \mathrm{d}k\,|\mathcal{P}_t(k)|^2 = \int \mathrm{d}k \int p_t(t_1) e^{ickt_1} dt_1 \int p_t(t_2) e^{ickt_2} dt_2 \\ &= 2\pi \int p_t(t_1) p_t(t_2) \Big(\int \frac{e^{ick(t_1-t_2)}}{2\pi} dk \Big) \mathrm{d}t_1 \mathrm{d}t_2 = (2\pi/c) \int p_t(t_1) p_t(t_2) \delta(t_1 - t_2) \mathrm{d}t_1 \mathrm{d}t_2 \\ &= (2\pi/c) \int p_t^2(t) \mathrm{d}t, \end{aligned} \tag{2.81}$$

which coincides with the factor in front of the Delta function in Eq. (2.76), when $\sigma_t^{\rm eff}$ is calculated using Eq. (2.77).

Using Eqs. (2.71) to (2.77) and (2.79), Eq. (2.70) takes the form

$$\frac{1}{M} = (1 - 1/n_e) \frac{\sqrt{\pi}}{\sigma_z^{\rm eff}} \frac{\int \mathrm{d}k\, \mathrm{d}^2\Omega_1\, \mathrm{d}^2\Omega_2\, k^4 \eta_{k\boldsymbol{n}_1} I^{(1)}_{k\boldsymbol{n}_1} \eta_{k\boldsymbol{n}_2} I^{(1)}_{k\boldsymbol{n}_2} \left|\mathcal{P}_\perp\big(k\boldsymbol{n}_1 - k\boldsymbol{n}_2\big)\right|^2}{\big(\int \mathrm{d}\boldsymbol{k} \eta_{\boldsymbol{k}} I^{(1)}_{\boldsymbol{k}}\big)^2}, \tag{2.82}$$

where $\boldsymbol{n}_1$ and $\boldsymbol{n}_2$ are two unit vectors,

$$\boldsymbol{n}_i = (n_{ix}, n_{iy}, n_{iz}), \quad n_{iz} = \sqrt{1 - n_{ix}^2 - n_{iy}^2}, \tag{2.83}$$

$$\mathrm{d}^2\Omega_i = \mathrm{d}n_{ix}\mathrm{d}n_{iy}/n_{iz}, \tag{2.84}$$

where $i = 1, 2$; $\mathrm{d}^2\Omega_i$ is the element of solid angle. Note that the above derivation did not use the paraxial approximation,

$$\boldsymbol{n}_i \approx (\phi_{ix}, \phi_{iy}, 1 - \phi_{ix}^2/2 - \phi_{iy}^2/2), \tag{2.85}$$

with $\phi_{ix}, \phi_{iy} \ll 1$. However, it can be used in most practical cases. Also, usually $n_e \gg 1$ and, hence, $1/n_e$ can be neglected.

For a Gaussian electron bunch [see Eq. (2.60)],

$$\left|\mathcal{P}_\perp\left(k\boldsymbol{n}_1 - k\boldsymbol{n}_2\right)\right|^2 = e^{-k^2\sigma_x^2(n_{1x}-n_{2x})^2 - k^2\sigma_y^2(n_{1y}-n_{2y})^2}, \tag{2.86}$$

$$\sigma_z^{\mathrm{eff}} = \sigma_z. \tag{2.87}$$

While in a typical electron storage ring the longitudinal momentum distribution is close to Gaussian, the longitudinal density distribution may not be Gaussian due to beam interaction with its environment (see [61], for example). This is also the case in IOTA. Equation (2.77) correctly accounts for the actual longitudinal distribution and it will be used in Section **??** during the calculations of the number of coherent modes M for the experiments in IOTA. The probability density function $p_t(t)$ will be measured using a wall-current monitor [62].

Equations (2.69) and (2.82) do not reveal the exact distribution of $\mathcal{N}$, they only give the variance $\mathrm{var}(\mathcal{N})$. However, the form of the distribution can be suggested by a simple qualitative argument when the number of longitudinal modes M_L (see [2, p. 28]) is much larger than one. For bending-magnet radiation $M_L \sim \omega\sigma_t$, for undulator radiation $M_L \sim$

$\omega\sigma_t/N_{\rm u}$, where $N_{\rm u}$ is the number of undulator periods. Indeed, in this case the total number of detected photons $\mathcal{N}$ is the sum of a large number of independent random numbers of detected photons coming from small longitudinal slices of the bunch. Therefore, according to the central limit theorem, $\mathcal{N}$ follows a normal distribution with good accuracy. More details on the exact distribution of $\mathcal{N}$ can be found in [2, 18, 59, 63–65] which suggest that, in the case of incoherent spontaneous radiation, the classical radiated power follows the Gamma distribution.

2.2 Calculation of spectral-angular distribution of the undulator radiation

To this point, the exact forms of $I_{\boldsymbol{k}}^{(1)}$ or $\mathcal{E}_{\boldsymbol{k}}$ have not been discussed. The kind of the synchrotron light source has not been specified. Below in this dissertation, our focus will be on the undulator (wiggler) radiation. Therefore, in this section, an expression for $\mathcal{E}_{\boldsymbol{k}}$ for the undulator (wiggler) radiation is provided at arbitrary value of the undulator parameter $K_{\rm u}$. The case of small $K_{\rm u} \ll 1$ has been considered in Refs. [66, 67], for example. The undulator parameter $K_{\rm u}$ is defined as

$$K_{\rm u} = \frac{eB\lambda_{\rm u}}{2\pi m_e c}, \tag{2.88}$$

where e is the electron charge, B is the amplitude of the vertical magnetic field in the undulator. The magnetic field in the undulator is assumed to follow a sinusoid inside the undulator as a function of the longitudinal position z along the undulator with the period $\lambda_{\rm u}$, see Fig. 1.1. The number of the undulator periods will be denoted by $N_{\rm u}$.

The paraxial approximation $\boldsymbol{k} = k(\phi_x, \phi_y, 1-\phi_x^2/2-\phi_y^2/2)$ will be used and, therefore, the notation will be slightly changed from $\mathcal{E}_{\boldsymbol{k}}$ to $\mathcal{E}_{k,s}(\boldsymbol{\phi})$, where $\boldsymbol{\phi} = (\phi_x, \phi_y)$ and the polarization subscript $s = 1, 2$ is explicitly included. For specificity, $s = 1$ and $s = 2$ will describe the horizontal and vertical polarizations, respectively.

The procedure to obtain an expression for $\mathcal{E}_{k,s}(\boldsymbol{\phi})$ is to find the trajectory $\boldsymbol{r}(t)$ of the electron in N_u periods of a sinusoidal magnetic field with the amplitude B and then calculate the integral in Eq. (2.34). This rather lengthy calculation has been carried out in Chapter 4 of Ref. [68]. Therefore, only the results will be presented here.

In the vicinity of hth harmonic of the undulator radiation,

$$\mathcal{E}_{k,1}(\boldsymbol{\phi}) = \frac{h\gamma N_\mathrm{u}}{A}\sqrt{\frac{\alpha}{k}}L\left(\frac{N_\mathrm{u}\Delta k}{k_1}\right)\left[2\gamma\phi_x\sum_{p=-\infty}^{+\infty}J_{n+2p}(X)J_p(Y)\right.$$
$$\left. - K_\mathrm{u}\left(\sum_{p=-\infty}^{+\infty}J_{n+2p-1}(X)J_p(Y) + \sum_{p=-\infty}^{+\infty}J_{n+2p+1}(X)J_p(Y)\right)\right], \quad (2.89)$$

$$\mathcal{E}_{k,2}(\boldsymbol{\phi}) = \frac{h\gamma N_\mathrm{u}}{A}\sqrt{\frac{\alpha}{k}}L\left(\frac{N_\mathrm{u}\Delta k}{k_1}\right)\left[2\gamma\phi_y\sum_{p=-\infty}^{+\infty}J_{n+2p}(X)J_p(Y)\right], \quad (2.90)$$

where $\boldsymbol{\phi} = (\phi_x, \phi_y)$, $\Delta k = k - hk_1$, $k_1 = 4\pi\gamma^2/(\lambda_\mathrm{u}A)$, $J_m(x)$ is the Bessel function of the first kind,

$$A = 1 + \frac{K_\mathrm{u}^2}{2} + \gamma^2(\phi_x^2 + \phi_y^2), \quad (2.91)$$

$$X = \frac{2hK_\mathrm{u}\gamma\phi_x}{A}, \quad (2.92)$$

$$Y = \frac{hK_\mathrm{u}^2}{4A} \quad (2.93)$$

$$L\left(\frac{N_\mathrm{u}\Delta k}{k_1}\right) = \frac{\sin\left(\frac{\pi N_\mathrm{u}\Delta k}{k_1}\right)}{N_\mathrm{u}\sin\left(\frac{\pi\Delta k}{k_1}\right)}. \quad (2.94)$$

Notice that in the equations above k_1 is a function of $(\phi_x^2 + \phi_y^2)$. For future reference, in

the fundamental ($h = 1$), the peak on-axis intensity is achieved at the wavelength

$$\lambda_1 = \frac{\lambda_\mathrm{u}}{2\gamma^2}\left(1 + \frac{K_\mathrm{u}^2}{2}\right). \tag{2.95}$$

If $\mathcal{E}_{k,s}(\boldsymbol{\phi})$ needs to be calculated in a wide spectral range including several harmonics, it may be approximated as a sum over several values of h in Eqs. (2.89) and (2.90). We developed a PYTHON package for calculation of $\mathcal{E}_{k,s}(\boldsymbol{\phi})$ in this way — WIGRAD [69]. The infinite sums over p in Eqs. (2.89) and (2.90) are approximated by keeping only a certain finite number of terms, e.g., 20 . The results obtained by this method are in agreement with the calculations by the general-purpose synchrotron radiation code SRW [70]. After numerical computation of $\mathcal{E}_{\boldsymbol{k}}$, one can obtain $I_{\boldsymbol{k}}^{(1)}$ by Eq. (2.36) and use it in the equations for $\langle\mathcal{N}\rangle$, M, and $\mathrm{var}(\mathcal{N})$ derived above.

2.3 Brookhaven experiment

Previously, Eq. (2.82) for the number of coherent modes M was derived for temporally incoherent radiation and arbitrary single-electron intensity function $I_{\boldsymbol{k}}^{(1)}$. Section 2.2 presented a way for numerical computation of $I_{\boldsymbol{k}}^{(1)}$ for the undulator (or wiggler) radiation. In the current section, it will be checked whether these predictions agree with the experimental data from the experiment at Brookhaven National Laboratory (BNL) reported in Ref. [13].

In the seminal experiment at BNL, the fluctuations in the wiggler and bending-magnet radiation were studied in the Vacuum-Ultraviolet (VUV) electron storage ring. The wiggler radiation data in Fig. 2.2 were extracted from the original paper [13] by digitizing the plot. The scale was also changed from log-log to a linear scale. This procedure could have introduced some deviations from the original data, but the deviations are believed to be negligible.

The data for the wiggler radiation were collected at the fundamental harmonic with the

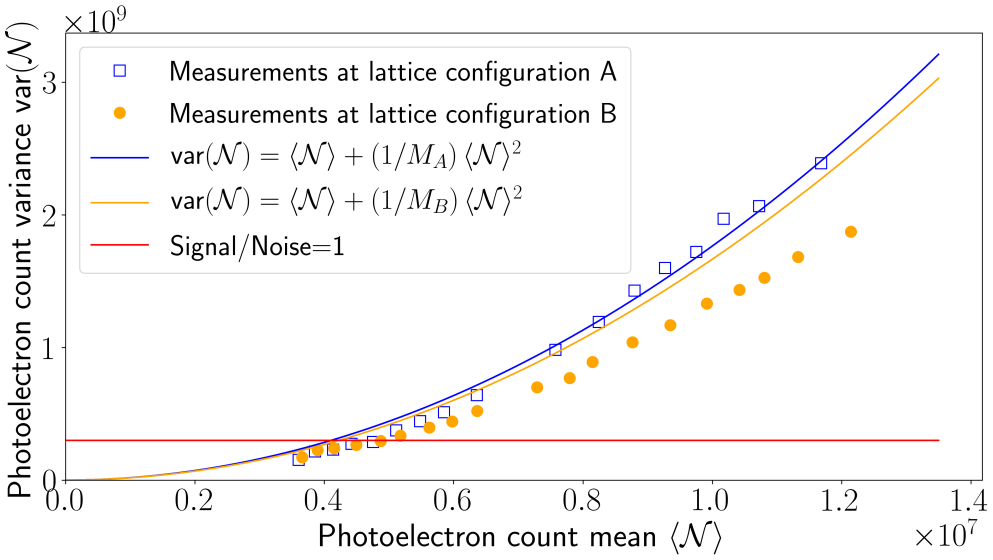

Figure 2.2: Experimental data from Ref. [13] for wiggler radiation (points) and predictions made by our calculation (solid curves). The noise variance (3×10^8) has been subtracted from the data.

on-axis peak at $\lambda_1 = 532\,\text{nm}$ [see Eq. (2.95)]. An optical interference filter with FWHM $= 3.2\,\text{nm}$ and a maximum transmission at λ_1 was used. Polarizing filters were not used. The parameters of the wiggler and the electron bunch are listed in Table 2.1. A silicon *p-i-n* photodiode was used to detect the wiggler radiation. A single convex lens was used to focus the radiation on the sensitive area of the photodiode. The measurements were carried out with two different lattice configurations, i.e., two different transverse electron beam profiles — in the language of the authors of Ref. [13], a tightly focused beam and a loosely focused beam. In this dissertation, let us refer to them as lattice configuration A and lattice configuration B, respectively.

The mean photoelectron count was mainly varied by using a variable neutral density filter. Neutral density filters are filters that have constant optical density in the wavelength region of interest. Such filters linearly scale down the photoelectron count mean, $\langle \mathcal{N} \rangle \to \eta_{\text{ND}} \langle \mathcal{N} \rangle$, where η_{ND} is the transmission of the neutral density filter. However, they do not change M, because if $\eta_{\boldsymbol{k}}$ is replaced by $\eta_{\text{ND}}\eta_{\boldsymbol{k}}$ in Eq. (2.82), then η_{ND} cancels out in the numerator and

Table 2.1: Summary of the parameters of the Brookhaven experiment [13] and the experiment at Fermilab in the IOTA storage ring [26, 50, 60]. The electron bunch dimensions correspond to the center of the wiggler (undulator). Both rings store a single electron bunch. The parameters of IOTA are given at $I_{\text{beam}} = 2.0\,\text{mA}$ for an electron beam with a strong transverse coupling, such that the transverse mode emittances are equal by design . For more details about the undulator in IOTA, see [71]. Some parameters of the BNL VUV ring are followed by (A) or (B) to specify the corresponding lattice configuration.

Parameter	BNL VUV ring	Fermilab IOTA ring
Ring circumference	51.06 m (170.2 ns)	40 m (133 ns)
Beam energy	650 MeV	96.4 MeV
Typical average current	50 mA	2.0 mA
Horizontal emittance (rms), ϵ_x	0.80 µm(A), 0.74 µm(B)	95 nm
Vertical emittance (rms), ϵ_y	0.20 µm(A), 0.26 µm(B)	95 nm
Relative momentum spread, σ_p/p	(not available)	2.7×10^{-4}
Horizontal beam size, σ_x	1.0 mm(A), 0.96 mm(B)	513 µm
Vertical beam size, σ_y	0.32 mm(A), 0.36 mm(B)	299 µm
Longitudinal bunch size, σ_z (σ_t)	6.11 cm (0.204 ns)	29 cm (0.97 ns)
Beam lifetime	≈ 100 min	> 10 min
Wiggler (undulator) parameter, K_{u}	5.7	1.0
Wiggler (undulator) period, λ_{u}	10 cm	5.5 cm
Number of wiggler (undulator) periods, N_{u}	22.5	10.5
Fundamental harmonic wavelength λ_1	532 nm	1.16 µm
Photodiode diameter	(not available)	1 mm
Quantum efficiency @λ_1	78 %	80 %
Monochromator FWHM	3.2 nm	(not used)
Simulated number of photon counts per turn, $\langle \mathcal{N} \rangle$	5.6×10^7	4.6×10^7
Simulated number of coherent modes, M	5.7×10^4(A), 6.0×10^4(B)	1.1×10^7
Ratio of fluctuation contributions, $\langle \mathcal{N} \rangle / M$	$\approx 10^3$	≈ 4

the denominator.

The two solid curves in Fig. 2.2 are the predictions made by Eqs. (2.69) and (2.82) using the parameters of the electron bunch, the wiggler, and the monochromator, given in Ref. [13]. The Gaussian model for the transmission of the monochromator was used. Equation (2.82) yields the following results for lattice configurations A and B, respectively: $M_A = 5.7 \times 10^4$ and $M_B = 6.0 \times 10^4$.

Although our calculation agrees well with the measurements at lattice configuration A, there is some disagreement at lattice configuration B. In terms of the M parameter, the deviation is about 20 %. It is not clear if this disagreement comes from inaccuracy in our model

or from our incomplete understanding of the experiment configuration from Ref. [13]. The experiment took place three decades ago and a detailed description is currently unavailable. This was one of the motivations for carrying out a new dedicated experiment in IOTA.

In particular, only the electron bunch rms dimensions σ_x, σ_y, σ_z are known for the Brookhaven experiment. The exact Twiss parameters of the electron beam optics in the wiggler are unknown. Therefore, our calculation for the Brookhaven experiment using Eq. (2.82) should be understood as an order-of-magnitude estimate. Equation (2.82) assumes negligible electron beam divergence, which could or could not be the case in the Brookhaven experiment (depending on the exact Twiss parameters in the wiggler). Also, a Gaussian longitudinal electron bunch density distribution is assumed, but there could be deviations. The exact transmission function of the monochromator and the exact angular acceptance are not available as well.

Furthermore, in the Brookhaven experiment, the number of coherent modes (M_A, M_B) is much smaller than the average number of photoelectrons $\langle \mathcal{N} \rangle$. Hence, the first term in Eq. (2.69) is negligible. Therefore, these data do not test Eq. (2.69) in the regime when the two contributions are comparable. This regime is tested in our independent experiment at IOTA.

2.4 Preliminary estimates and motivation for the experiment in IOTA

It will be shown later in this dissertation, that in the IOTA experiment, the angular electron beam divergence affects the number of coherent modes M and, hence, Eq. (2.82) cannot be used. For this reason, a more general expression for M will be obtained in Section 2.5. However, for now, let us broadly discuss what may be expected in the experiment in IOTA using the simpler Eq. (2.82). The exact description will be provided later.

Because in IOTA the fundamental of the undulator radiation is in the near-infrared

range, $\lambda_1 = 1.16\,\mu\text{m}$ [see Eq. (2.95)], it is necessary to use an InGaAs p-i-n photodiode [72] instead of the silicon one, used in [13]. A polarizing filter will not be used. Both polarization components will be registered. The spectral distribution of the number of photons detected in an aperture with a 2" diameter, located 3.5 m away from the undulator in IOTA is shown in Fig. 2.3 (the red curve). This curve was obtained by using our simulation package WIGRAD [69] and also verified by an independent simulation using the SRW software [70]. This curve is calculated for a single electron (s.e.),

$$\frac{\mathrm{d}\,\langle \mathcal{N}_{\text{s.e.}} \rangle}{\mathrm{d}k} = \sum_{s=1,2} \int \mathrm{d}^2\boldsymbol{\phi}\, \eta_{k,s}(\boldsymbol{\phi}) \left| \mathcal{E}_{k,s}(\boldsymbol{\phi}) \right|^2, \tag{2.96}$$

where the notation for the detection efficiency was changed from $\eta_{\boldsymbol{k}}$ to $\eta_{k,s}(\boldsymbol{\phi})$ to explicitly include the polarization s. In this calculation, $\eta_{k,s}(\boldsymbol{\phi}) = 1$ inside the round $\varnothing$2" aperture and zero outside. For convenience, in Fig. 2.3, the results are presented in terms of the distribution over the wavelength λ instead of the magnitude of the wave-vector k.

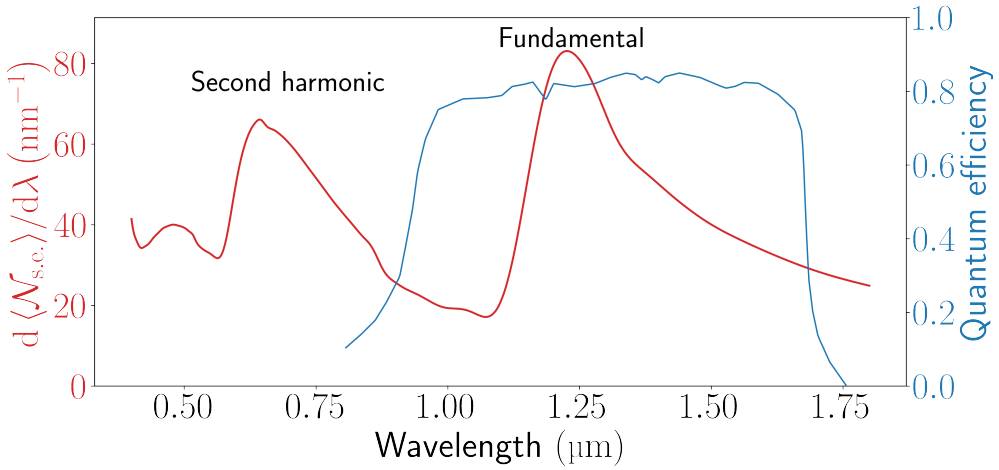

Figure 2.3: Spectral distribution of the average number of detected photons per turn for a single electron (s.e.) for the undulator in IOTA (red curve) assuming an ideal detector. Quantum efficiency of an InGaAs p-i-n photodiode (blue curve).

Assuming no additional losses apart from the quantum efficiency of the InGaAs photodiode, some estimations were made for the expected number of photoelectrons $\langle \mathcal{N} \rangle$ and the

number of coherent modes M for the proposed IOTA experiment. The results are given in Table 2.1 and in Fig. 2.4. Since the goal of this section is to obtain order-of-magnitude estimates, the rms bunch length σ_z is used instead of the effective bunch length $\sigma_z^{\rm eff}$. It is better to avoid using a monochromator in IOTA. This will let us see approximately the same average photoelectron count $\langle \mathcal{N} \rangle$ as in the Brookhaven experiment, even though the beam current, beam energy, undulator (wiggler) parameter $K_{\rm u}$, and the number of undulator periods are lower in IOTA. This is important in order to have a signal of a comfortable amplitude for measurements.

The absence of a monochromator will also make the number of coherent modes M much larger than in the Brookhaven experiment, see Table 2.1, and comparable to $\langle \mathcal{N} \rangle$. This will allow us to probe Eq. (2.69) in the regime where the two sum terms are comparable, see the last row in Table 2.1. Indeed, the curve denoted by M_0 in Fig. 2.4 is rather close to the green dashed line, representing the photon shot noise fluctuations. The value of M_0 was calculated by Eq. (2.82) assuming no additional losses except for the quantum efficiency of the detector. This is the value of M reported in Table 2.1. The curves denoted by M_1 and M_2 were calculated with bandpass filters $(1050\,{\rm nm}, 1350\,{\rm nm})$ and $(1150\,{\rm nm}, 1300\,{\rm nm})$, respectively: $M_1 = 4.6 \times 10^6$ and $M_2 = 2.7 \times 10^6$. These two curves are provided to show how the data may change due to the spectral properties of additional optical elements in the measurement apparatus. The real spectral range will be narrower than that of the InGaAs photodiode. It will be determined by transmission curves of additional optical elements, such as lenses, mirrors, and, possibly, bandpass filters. It will be important to painstakingly account for transmission curves of all of the optical elements used in the experiment.

As opposed to neutral density filters, bandpass filters do change the number of coherent modes M. However, typically, at fixed beam current and shape, the ratio between the incoherence contribution and the photon shot noise contribution in Eq. (2.69), namely, $\langle \mathcal{N} \rangle / M$, stays approximately constant when different bandpass filters are used. For example, it is

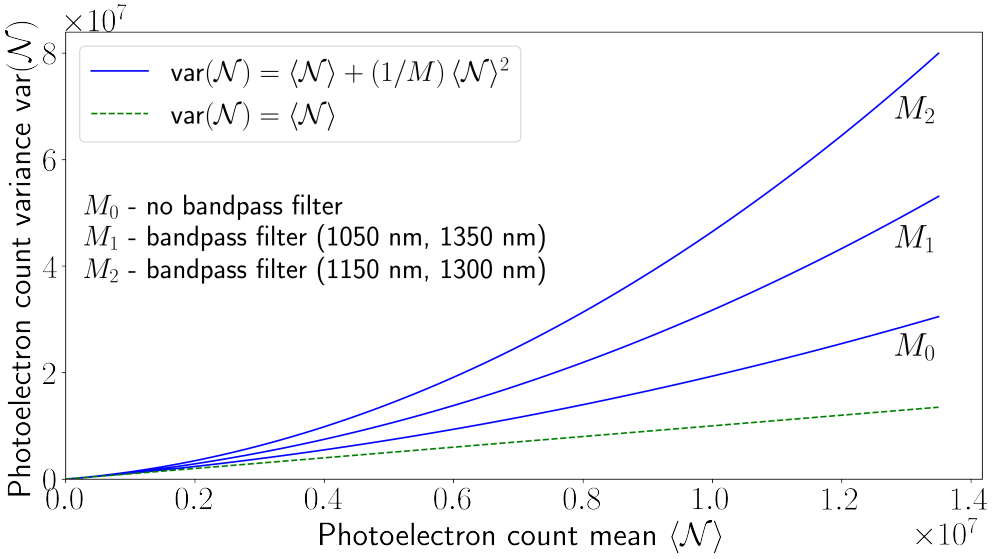

Figure 2.4: Simulations of the photoelectron count variance in IOTA for three different filter configurations. The green dashed line represents the photon shot noise contribution to the fluctuations.

clear in a simplified model of a Gaussian spectral-angular distribution of radiation, considered in [17] and in Section 2.6. In the proposed experiment in IOTA, at $I_{\text{beam}} = 2.0\,\text{mA}$, $\langle \mathcal{N} \rangle / M \approx 4$, see Table 2.1.

In the simulation in Fig. 2.4, the same measurement procedure is assumed as in the Brookhaven experiment. Namely, in each curve, the mean photoelectron count $\langle \mathcal{N} \rangle$ is varied by using a variable neutral density filter. The bunch charge is constant. This means that σ_x, σ_y, σ_t, and M are constant too. The values used in the simulation are provided in Table 2.1. In our experiment in IOTA, the bunch charge will also be varied to observe how the magnitude of the fluctuations $\text{var}(\mathcal{N})$ changes in this case. The dependence of $\text{var}(\mathcal{N})$ on $\langle \mathcal{N} \rangle$ will be nontrivial (not a parabola) because the dimensions of the electron bunch in IOTA change significantly with beam current, and so should M, according to Eq. (2.82). Some examples of the effects that depend on beam current and that determine the electron bunch shape and size in IOTA include intrabeam scattering [73–75] and interaction of the electron bunch with its environment [61].

The proposed measurements in IOTA can help improve our understanding of these effects, because they can provide some information about the dimensions and the shape of the electron bunch in IOTA. Indeed, Eqs. (2.82), (2.86), and (2.87) indicate that the magnitude of the fluctuations depends on the dimensions of a Gaussian bunch. Also, if the longitudinal shape of the bunch is not Gaussian, it will be reflected in the magnitude of the fluctuations according to Eq. (2.77).

The transverse beam sizes σ_x and σ_y are measured by synchrotron radiation monitors using the radiation from dipole magnets, while σ_z and σ_z^{eff} are measured by a wall-current monitor. The existing physical model of beam lifetimes and beam shapes in IOTA (taking into account intrabeam scattering, gas scattering, quantum excitation, etc.) is not fully consistent with observations [76]. An independent estimate of σ_x, σ_y and σ_z (or a certain combination of them) through fluctuations in undulator radiation, see Eq. (2.82), may help resolve inconsistencies. The results of the IOTA experiment are discussed in Chapter 3.

2.5 Derivation of the fluctuations with a considerable beam divergence

Previously, an equation for M [Eq. (2.82)] was derived for the case of a monoenergetic electron beam, zero angular electron beam divergence and temporally incoherent radiation. Below, the steps are outlined to extend this result to the case of a considerable beam divergence. The expression for M for this case will be obtained for the first time. In the previous theoretical derivations [16, 17], only the effect of spatial distribution of the electrons inside the bunch on the turn-to-turn fluctuations was considered. It was not taken into account that in general the distribution of electron velocities affects the fluctuations as well.

In this section, our goal is to obtain a general, but practical, expression to be used for the calculations in IOTA, where the electron beam divergence in the undulator is not negligible. Therefore, from the beginning, the paraxial approximation [2.85] will be used and both

polarizations $s = 1, 2$ will be accounted for. Therefore, the notation $\eta_{k,s}(\boldsymbol{\phi})$ and $\mathcal{E}_{k,s}(\boldsymbol{\phi})$ will be used for the detection efficiency $\eta_{\boldsymbol{k}}$ and the complex field amplitude $\mathcal{E}_{\boldsymbol{k}}$, respectively, where $\boldsymbol{\phi} = (\phi_x, \phi_y)$ specifies the direction of the wave-vector $\boldsymbol{k}$ in the paraxial approximation $\boldsymbol{k} = k(\phi_x, \phi_y, 1 - \phi_x^2/2 - \phi_y^2/2)$.

One can start the derivation with Eq. (2.26), but written in the form that accounts for the beam divergence and converted to an integral over k and $\boldsymbol{\phi}$, namely,

$$\mathrm{var}(\mathcal{N}) = \langle \mathcal{N} \rangle - \langle \mathcal{N} \rangle^2 + \int \mathrm{d}\xi \; p(\xi) \Big[\sum_{s=1,2} \int \mathrm{d}k \, \mathrm{d}^2\boldsymbol{\phi} \, \eta_{k,s}(\boldsymbol{\phi}) \Big| \sum_m \mathcal{E}_{k,s}^{(m)}(\boldsymbol{\phi}) \Big|^2 \Big]^2, \tag{2.97}$$

where ξ describes the states in the 6D phase-space of all the electrons in the center of the radiator,

$$\xi = \tilde{x}_1, \tilde{x}'_1, y_1, y'_1, t_1, \delta p_1 \ldots \tilde{x}_{n_e}, \tilde{x}'_{n_e}, y_{n_e}, y'_{n_e}, t_{n_e}, \delta p_{n_e}, \tag{2.98}$$

where t_m is the time when the mth electron passes through the center of the synchrotron light source, $p(\xi)$ represents the density function for the probability to have the state ξ,

$$p(\xi) = p(\tilde{x}_1, \tilde{x}'_1, y_1, y'_1, t_1, \delta p_1) \ldots p(\tilde{x}_{n_e}, \tilde{x}'_{n_e}, y_{n_e}, y'_{n_e}, t_{n_e}, \delta p_{n_e}), \tag{2.99}$$

$\tilde{x}_m$ and $\tilde{x}'_m$ refer to the monoenergetic component of the motion, because there is also a contribution from the horizontal dispersion, so that

$$x_m = \tilde{x}_m + D_x \delta p_m, \qquad\qquad x'_m = \tilde{x}'_m + D_{x'} \delta p_m, \tag{2.100}$$

and the vertical dispersion is assumed to be zero. According to [2, Eq. (2.93)], the complex field amplitude of the mth electron $\mathcal{E}_{k,s}^{(m)}(\boldsymbol{\phi})$ can be expressed through the amplitude of the reference electron $\mathcal{E}_{k,s}(\boldsymbol{\phi})$ [see Eqs. (2.34), (2.89), and (2.90)] as

$$\mathcal{E}_{k,s}^{(m)}(\boldsymbol{\phi}) = e^{ik_x x_m + ik_y y_m - ict_m} \mathcal{E}_{k,s}(\boldsymbol{\phi} - \boldsymbol{r}'_m), \tag{2.101}$$

where $\boldsymbol{r}'_m = (x'_m, y'_m)$ and it is assumed that $\mathcal{E}^{(m)}_{k,s}(\boldsymbol{\phi})$ does not depend on δp_m directly [only through the dispersion D_x and $D_{x'}$, see Eq. (2.100)]. For the reference electron $\tilde{x}, \tilde{x}', y, y', t, \delta p$ are equal to zero.

The electron bunch is assumed to be Gaussian in the transverse plane. The distribution of δp is assumed to be Gaussian as well. The longitudinal density distribution $p_t(t)$ is arbitrary. The beam focusing optics is assumed to be uncoupled. In this case, the probability density function for one electron takes the following form,

$$p(\tilde{x}, \tilde{x}', y, y', t, \delta p) = \frac{1}{4\pi^2 \epsilon_x \epsilon_y} \exp\Big[-\frac{1}{2\epsilon_x^2} C_x(\tilde{x}, \tilde{x}') - \frac{1}{2\epsilon_y^2} C_y(y, y')\Big] \times p_t(t) \frac{1}{\sqrt{2\pi}\sigma_p} \exp\Big[-\frac{\delta p^2}{2\sigma_p^2}\Big], \quad (2.102)$$

with

$$C_x(\tilde{x}, \tilde{x}') = \gamma_x \tilde{x}^2 + 2\alpha_x \tilde{x}\tilde{x}' + \beta_x (\tilde{x}')^2, \quad (2.103)$$

$$C_y(y, y') = \gamma_y y^2 + 2\alpha_y y y' + \beta_y (y')^2. \quad (2.104)$$

Given Eqs. (2.98) to (2.104), and assuming the regime of temporal incoherence ($\omega\sigma_t \gg 1$), the integration in Eq. (2.97) is solely a mathematical procedure. It is analogous to the derivations in Sections 2.1.3 and 2.1.5 where ξ included only x_m, y_m and t_m. The only difference is the additional integration over $\tilde{x}'_m$, y'_m and δp_m, with $m = 1 \dots n_e$. When the multidimensional integral in Eq. (2.97) has been calculated, one can compare the result with Eq. (2.69) and arrive at the following expression for M,

$$\frac{1}{M} = (1 - 1/n_e) \frac{\sqrt{\pi}}{\sigma_z^{\text{eff}}} \frac{\int \mathrm{d}k \, \mathrm{d}^2\boldsymbol{\phi}_1 \, \mathrm{d}^2\boldsymbol{\phi}_2 \, \mathrm{d}^2\boldsymbol{r'} \, \mathcal{P}_k(\boldsymbol{r'}, \boldsymbol{\phi}_1 - \boldsymbol{\phi}_2) \mathcal{I}_k(\boldsymbol{\phi}_1, \boldsymbol{r'}) \mathcal{I}_k^*(\boldsymbol{\phi}_2, \boldsymbol{r'})}{\langle \mathcal{N}_{\text{s.e.}} \rangle^2}, \quad (2.105)$$

with

$$\mathcal{P}_k(\boldsymbol{r'}, \boldsymbol{\phi}_1 - \boldsymbol{\phi}_2) = \frac{1}{4\pi\sigma_{x'}\sigma_{y'}} e^{-\frac{(x')^2}{4\sigma_{x'}^2} - \frac{(y')^2}{4\sigma_{y'}^2}} \times e^{-ik\Delta_x(\phi_{1x}-\phi_{2x})x' - ik\Delta_y(\phi_{1y}-\phi_{2y})y'} e^{-k^2\Sigma_x^2(\phi_{1x}-\phi_{2x})^2 - k^2\Sigma_y^2(\phi_{1y}-\phi_{2y})^2}, \quad (2.106)$$

$$\mathcal{I}_k(\boldsymbol{\phi}, \boldsymbol{r'}) = \sum_{s=1,2} \eta_{k,s}(\boldsymbol{\phi}) \mathcal{E}_{k,s}(\boldsymbol{\phi}) \mathcal{E}^*_{k,s}(\boldsymbol{\phi} - \boldsymbol{r'}), \quad (2.107)$$

$$\langle \mathcal{N}_{\text{s.e.}} \rangle = \sum_{s=1,2} \int \mathrm{d}k \, \mathrm{d}^2\boldsymbol{\phi} \, \eta_{k,s}(\boldsymbol{\phi}) \left| \mathcal{E}_{k,s}(\boldsymbol{\phi}) \right|^2, \quad (2.108)$$

where $s = 1, 2$ indicates the polarization component, n_e is the number of electrons in the bunch, $k = 2\pi/\lambda$ is the magnitude of the wave vector; $\boldsymbol{\phi} = (\phi_x, \phi_y)$, $\boldsymbol{\phi}_1 = (\phi_{1x}, \phi_{1y})$ and $\boldsymbol{\phi}_2 = (\phi_{2x}, \phi_{2y})$ represent angles of direction of the radiation in the paraxial approximation, the effective bunch length σ_z^{eff} in Eq. (2.105) was defined previously in Eqs. (2.77) and (2.79), it is equal to the rms bunch length σ_z for a Gaussian bunch; $\boldsymbol{r'} = (x', y')$ represents the direction of motion of an electron at the radiator center, relative to a reference electron; $\sigma_{x'}$ and $\sigma_{y'}$ are the rms beam divergences,

$$\sigma_{x'}^2 = \gamma_x \epsilon_x + D_{x'}^2 \sigma_p^2, \qquad \sigma_{y'}^2 = \gamma_y \epsilon_y, \quad (2.109)$$

$$\Sigma_x^2 = \epsilon_x/\gamma_x + (\gamma_x D_x + D_{x'}\alpha_x)^2 \beta_x \epsilon_x \sigma_p^2/\sigma_{x'}^2, \qquad \Sigma_y^2 = \epsilon_y/\gamma_y, \quad (2.110)$$

$$\Delta_x = (\alpha_x \epsilon_x - D_x D_{x'} \sigma_p^2)/\sigma_{x'}^2, \qquad \Delta_y = \alpha_y/\epsilon_y, \quad (2.111)$$

where α_x, β_x, γ_x, α_y, β_y, γ_y are the Twiss parameters of an uncoupled focusing optics in the synchrotron radiation source; D_x, $D_{x'}$ are the horizontal dispersion and its derivative, and the vertical dispersion is assumed to be zero; ϵ_x, ϵ_y are the unnormalized rms emittances;

σ_p is the relative rms momentum spread. The following two useful relations exist,

$$\sigma_x^2 = \Sigma_x^2 + \sigma_{x'}^2 \Delta_x^2, \qquad \sigma_y^2 = \Sigma_y^2 + \sigma_{y'}^2 \Delta_y^2, \tag{2.112}$$

where σ_x and σ_y are the transverse rms beam sizes. The electrons are assumed to be ultrarelativistic, $\gamma \gg 1$, where γ is the Lorentz factor.

The parameter $\langle \mathcal{N}_{\text{s.e.}} \rangle$ in Eq. (2.105) is the average number of detected photons per turn for a single electron (s.e.) circulating in the ring. The case of incoherent radiation ($\sigma_z k \gg 1$) is considered. Therefore, the average number of detected photons for the entire bunch can be obtained as

$$\langle \mathcal{N} \rangle = n_e \langle \mathcal{N}_{\text{s.e.}} \rangle . \tag{2.113}$$

The integrals in Eqs. (2.105) and (2.108) are taken from minus to plus infinity over all integration variables except for k, which goes from zero to plus infinity. The spectral sensitivity and the aperture of the detector are assumed to be included in the detection efficiency $\eta_{k,s}(\boldsymbol{\phi})$, which is a function of polarization, k, and $\boldsymbol{\phi}$ for that reason.

It was decided to study the undulator radiation in IOTA, because the quadratic term in Eq. (2.69), sensitive to bunch parameters, is larger for undulators and wigglers than it is for dipole magnets [16]. If the bending-magnet radiation was used in IOTA, the photon shot noise term would be dominant in Eq. (2.69). Although it could be interesting to observe this regime, it was more interesting to study the case where the incoherence contribution in Eq. (2.69) is considerable and the fluctuations var($\mathcal{N}$) have some dependence on the electron bunch parameters. The complex field amplitude $\mathcal{E}_{k,s}(\boldsymbol{\phi})$, generated by a single electron, can be numerically calculated using Eqs. (2.89) and (2.90) by our PYTHON package WIGRAD [69], based on the equations from [68], or by using the SRW code library [70]. Then, the integrals in Eqs. (2.105) and (2.108) can be calculated by a Monte-Carlo algorithm — our C++ code with PYTHON bindings for calculation of Eqs. (2.105) and (2.108) is provided in

the repository [77].

2.6 Examples of closed-from expressions for the number of coherent modes. Temporally incoherent radiation

Given certain additional assumptions about the radiation source, the electron beam, and the detector, the expressions [Eqs. (2.70), (2.82), and (2.105)] for the number of coherent modes M in the case of temporally incoherent radiation can take simpler forms. Three such examples are presented in this section.

2.6.1 Single-mode detector

The first example where the expression for M takes a simple form is the extreme approximation of a single mode detector, which can only sense one optical mode with a certain wave-vector $\boldsymbol{k}_{\rm det}$. In this case the detection efficiency can be represented by a Delta function $\eta_{\boldsymbol{k}} \propto \delta(\boldsymbol{k} - \boldsymbol{k}_{\rm det})$. It readily follows from Eq. (2.70) that in this model $M = (1 - 1/n_e)^{-1}$. Hence,

$$\mathrm{var}(\mathcal{N}) = \langle \mathcal{N} \rangle + (1 - 1/n_e) \langle \mathcal{N} \rangle^2 . \tag{2.114}$$

which coincides with the results, reported in Refs. [13, 24, 25, 78, 79]. Equation (2.114) is correct for any source of temporally incoherent synchrotron radiation, and for any direction and wavelength of $\boldsymbol{k}$.

2.6.2 Gaussian electron bunch and radiation profile. Negligible electron beam divergence

Assume that the following relation is fulfilled for the complex field amplitude $\mathcal{E}_{k,s}(\boldsymbol{\phi})$ and the detection efficiency $\eta_{k,s}(\boldsymbol{\phi})$,

$$\sqrt{\eta_{k,s}(\boldsymbol{\phi})}\mathcal{E}_{k,s}(\boldsymbol{\phi}) = \sqrt{C_s \exp\big[-\frac{(k-k_0)^2}{2\sigma_k^2} - \frac{\phi_x^2}{2\sigma_{r,x'}^2} - \frac{\phi_y^2}{2\sigma_{r,y'}^2}\big]}, \tag{2.115}$$

which leads to a Gaussian spectral-angular distribution for the number of detected photons $\mathcal{N}$, assuming negligible electron beam divergence,

$$\frac{\mathrm{d}^3\langle\mathcal{N}\rangle}{\mathrm{d}k\mathrm{d}\phi_x\mathrm{d}\phi_y} = C\exp\big[-\frac{(k-k_0)^2}{2\sigma_k^2} - \frac{\phi_x^2}{2\sigma_{r,x'}^2} - \frac{\phi_y^2}{2\sigma_{r,y'}^2}\big], \tag{2.116}$$

where k is the magnitude of the wave-vector, ϕ_x and ϕ_y represent the horizontal and vertical angles of the direction of the radiation in the paraxial approximation [see Eq. (2.85)], k_0 refers to the center of the radiation spectrum, σ_k is the spectral rms width, $\sigma_{r,x'}$ and $\sigma_{r,y'}$ are the angular rms radiation sizes, C_s and C are constants.

In addition, assume a Gaussian electron bunch with rms sizes σ_x, σ_y, σ_z, longitudinally incoherent radiation $k_0\sigma_z \gg 1$, and a very narrow radiation bandwidth $\sigma_k \ll 1/(\sigma_x\sigma_{r,x'})$, $\sigma_k \ll 1/(\sigma_y\sigma_{r,y'})$. Then, it follows from Eq. (2.62) that

$$M = (1-1/n_e)^{-1}\sqrt{1+4\sigma_k^2\sigma_z^2}\sqrt{1+4k_0^2\sigma_{r,x'}^2\sigma_x^2}\sqrt{1+4k_0^2\sigma_{r,y'}^2\sigma_y^2}. \tag{2.117}$$

This limit of Eq. (2.62) was previously obtained in [17], where the turn-to-turn intensity fluctuations were considered classically. Also, similar calculations for a one-dimensional model (longitudinal) were carried out in [2, pp. 26-28].

In general, the parameters of the spectral-angular distribution k_0, σ_k, $\sigma_{r,x'}$, $\sigma_{r,y'}$ are determined by both the properties of the emitted synchrotron radiation and by the properties of the detecting system (angular acceptance, detection efficiency as a function of wavelength).

As an approximation, it is possible to use this Gaussian model to consider a certain harmonic h of the undulator radiation unrestricted by any angular acceptance. In this case,

the magnitude of the wave-vector corresponding to the central peak k_0 can be chosen as

$$k_0 = \frac{4\pi\gamma^2 h}{\lambda_\mathrm{u}\left(1+\frac{K_\mathrm{u}^2}{2}\right)}. \tag{2.118}$$

Further, if a very narrow spectral filter is used $\sigma_k \ll k_0/(hN_\mathrm{u})$, then, the natural angular sizes of the undulator radiation can be estimated as $\sigma_{r,x'}, \sigma_{r,y'} \approx \sqrt{\lambda_0/(2L_\mathrm{u})}$ [2, Eq. (2.57)], where $\lambda_0 = 2\pi/k_0$ and $L_\mathrm{u} = N_\mathrm{u}\lambda_\mathrm{u}$ is the total length of the undulator.

2.6.3 Gaussian electron bunch and radiation profile. Non-negligible electron beam divergence

It is possible to generalize the result of Eq. (2.117) to the case of non-negligible electron beam divergence. Namely, one can use the Gaussian radiation profile from Eq. (2.115) in Eq. (2.105), which can account for the complete 6D phase-space density distribution of the electron bunch Eq. (2.102). In this section, a Gaussian temporal distribution $p_t(t)$ of the electron bunch is assumed. The same assumptions are made about the parameters of the spectral-angular distribution of the radiation as in Section 2.6.2. Namely, $k_0\sigma_z \gg 1$, $\sigma_k \ll 1/(\sigma_x\sigma_{r,x'})$, $\sigma_k \ll 1/(\sigma_y\sigma_{r,y'})$.

After lengthy derivations, which will not be presented here, one can arrive at the following expression for the number of coherent modes M,

$$M = (1-1/n_e)^{-1}\sqrt{1+4\sigma_k^2\sigma_z^2}\sqrt{1+4k_0^2(\sigma_x^2\sigma_{r,x'}^2+\sigma_{x'}^2\Sigma_x^2)+\frac{\sigma_{x'}^2}{\sigma_{r,x'}^2}} \times\sqrt{1+4k_0^2(\sigma_y^2\sigma_{r,y'}^2+\sigma_{y'}^2\Sigma_y^2)+\frac{\sigma_{y'}^2}{\sigma_{r,y'}^2}}, \tag{2.119}$$

the definitions of Σ_x and Σ_y are provided in Eq. (2.110), $\sigma_{x'}$ and $\sigma_{y'}$ are the horizontal and vertical rms angular electron beam divergences, their relation to the corresponding electron

beam emittances ϵ_x and ϵ_y and the rms momentum spread σ_p is provided in Eq. (2.109).

In the limit of zero rms electron beam divergence ($\sigma_{x'}, \sigma_{y'} = 0$), Eq. (2.119) coincides with [17, Eq. (17)] and Eq. (2.117), where this less general case was considered.

2.7 Summary

Equation (2.57) was derived within the framework of quantum optics. This equation predicts the fluctuations var($\mathcal{N}$) in spontaneous synchrotron radiation with any degree of coherence for an electron bunch of arbitrary shape. It is assumed that the electron bunch has negligible angular divergence and energy spread. Then, several possible simplifications were considered for temporally incoherent radiation. The formulas properly take into account the discrete nature of light and the quantum efficiency of the detector, which, in general, is a function of the radiation wavelength. A spectral filter with any transmission function can be incorporated by including the transmission function into $\eta_{\boldsymbol{k}}$ in Eqs. (2.57), (2.70), and (2.82). The detector acceptance can be taken into account by setting $\eta_{\boldsymbol{k}}$ to zero outside of a given angular range.

The predicted variance of the number of detected photons [using Eq. (2.82)] was compared with the empirical data from a previous experiment at Brookhaven [13] for the case of wiggler radiation with a dominant incoherence contribution to the fluctuations. A reasonable agreement within 20 % was observed. However, the exact cause of the deviation cannot be established because the details of the experiment, carried out three decades ago, cannot be found.

Therefore, it was proposed to carry out a new experimental study into the undulator radiation fluctuations in the IOTA storage ring. As will be shown later, in IOTA, the electron beam divergence can affect the number of coherent modes M and, to account for this, a more general equation [Eq. (2.105)] was derived. In this experiment, our calculation of the photoelectron count variance may be tested in a new regime (compared to the Brookhaven

experiment), when the photon shot noise contribution and the incoherence contribution are comparable.

In addition, in IOTA, it will be possible to explore the possibility of determining some electron bunch parameters using the measured value of the photoelectron count variance $\mathrm{var}(\mathcal{N})$. It was pointed out in [14, 15, 17, 18] that the fluctuations in synchrotron radiation can be used to determine the bunch length on a picosecond scale, and the proof of principle experiments were successful. Moreover, references [14, 15] suggest that if the fluctuations in the radiation spectrum are measured with a high resolution spectrometer, then even the longitudinal profile of the electron bunch can be reconstructed. In IOTA, the longitudinal bunch size is relatively large and can be easily measured with a wall-current monitor [62], $\sigma_z = 29\,\mathrm{cm}$ at $I_{\mathrm{beam}} = 2.0\,\mathrm{mA}$ (strong transverse coupling, see Table. 2.1) . On the other hand, the transverse bunch size (especially vertical size of the uncoupled beam) can be quite small, down to a few tens of microns, where it may be difficult to measure by conventional synchrotron radiation monitors [80], because of the diffraction limit and other effects. However, the number of coherent modes M in the undulator radiation in IOTA is rather sensitive to the transverse bunch size (or emittance). Therefore, the magnitude of the fluctuations may help determine the transverse dimensions (or emittances) of the electron bunch.

In any case, the measurement of the undulator radiation fluctuations in IOTA is a measurement of a certain function [see Eqs. (2.69) and (2.82)] of electron bunch dimensions and shape. This measurement is independent from the wall-current monitor and the synchrotron radiation monitors. Therefore, it may help refine the existing model of the physical effects determining the electron bunch parameters in IOTA. The results of this effort will be discussed in detail in Section 3.5.

CHAPTER 3

MEASUREMENTS WITH A BUNCH OF ELECTRONS IN THE IOTA RING

3.1 Introduction

Full understanding of the radiation generated by accelerating charged particles is crucial for accelerator physics and electrodynamics in general. The predictions of classical electrodynamics for pulse-by-pulse average characteristics of synchrotron radiation, such as the total radiated power, spectral composition, angular intensity distribution and brightness [2], are supported by countless observations. In fact, they are confirmed every day by routine operations of synchrotron radiation user facilities. On the other hand, the pulse-to-pulse statistical fluctuations of synchrotron radiation have not been studied at the same level of detail yet, although substantial progress has been made in the past few decades. The turn-to-turn intensity fluctuations of incoherent spontaneous bending-magnet, wiggler, and undulator radiation in storage rings have been studied in Refs. [13–18], both theoretically and experimentally. The statistical properties of the free-electron laser (FEL) radiation have been studied in Refs. [19–25]. Moreover, Refs. [43, 44] claimed to observe a non-classical sub-Poissonian photon statistics in the seventh coherent spontaneous harmonic of an FEL, although it could have been an instrumentation effect [45]. In any case, more experimental studies into the statistical properties of synchrotron radiation are needed. This chapter presents our observation of turn-to-turn power fluctuations of incoherent spontaneous undulator radiation in the Integrable Optics Test Accelerator (IOTA) storage ring at Fermilab [26]. The measurements are compared with the predictions made by our expression for the number of coherent modes Eq. (2.105), which extends the previous theoretical description [16, 17] (also Section 2.1). Namely, in Refs. [16, 17] (and in Section 2.1), only the effect of spatial distribution of the electrons inside the bunch on the turn-to-turn fluctuations is

considered. However, in general, the distribution of electron velocities affects the fluctuations as well. The results presented in this chapter are the first experimental test of our generalized formula [Eq. (2.105)] for the fluctuations in the case of non-negligible electron beam divergence.

Most often, fluctuations and noise are encountered in a negative context and are considered something that needs to be minimized. However, there are multiple examples where noise is used as a non-invasive probe into the parameters of a certain system, and even to measure fundamental constants. Some examples are the pioneering determination of the elementary charge e by the shot noise [81], and the determination of the Boltzmann constant k_B by the Johnson-Nyquist noise [82]. In fact, the latter effect is also relevant to accelerators and storage rings, where it is known as Schottky noise [83] due to the finite number of charge carriers in the beam, as described by Schottky [84]. Many beam parameters, such as the momentum spread, the number of particles and even transverse rms emittances, are imprinted into the power spectrum of Schottky noise. It is often used in beam diagnostics [85–87]. In fact, the fluctuations in synchrotron radiation are similar to Schottky noise. Both effects are related to the existence of discrete point-like charges as opposed to a continuos charge fluid. Because the synchrotron radiation is generated by individual electrons in the beam, one may even think of the fluctuations in the synchrotron radiation as the Schottky noise in the beam current passed on to the synchrotron radiation power. Therefore, one could assume that the synchrotron radiation power noise may carry information about beam parameters as well. This assumption is, in fact, correct. Three decades ago, Ref. [13] reported the results of an experimental study into statistical properties of wiggler radiation in a storage ring. It was noted that the magnitude of turn-to-turn intensity fluctuations depends on the dimensions of the electron bunch. The potential in beam instrumentation was soon realized [88] and a number of papers followed. However, to this day, mostly measurements of a bunch length via these fluctuations were discussed [14, 15, 17]. Only Ref. [18] reported an order-of-magnitude

measurement of a transverse emittance. Section 3.5 describes a new fluctuations-based technique for an absolute measurement of a transverse emittance. There are no free parameters in our equations, nor is a calibration required. However, the transverse and longitudinal focusing functions of the storage ring are assumed to be known. This technique is tested at the IOTA storage ring. For a beam with approximately equal and relatively large transverse rms emittances, the results agree with conventional visible synchrotron light monitors (SLMs) [80]. Then, in a different regime, this new technique is used to measure a much smaller vertical emittance of a flat beam, unresolvable by the SLMs. These emittance measurements agree with estimates, based on the beam lifetime. Possible further improvements are discussed.

3.2 Apparatus

In our experiment, a single electron bunch circulated in the IOTA storage ring, see Fig. 3.1(a), with a revolution period of 133.3 ns and the beam energy of 96.4 ± 1 MeV. Two transverse focusing configurations were considered in IOTA: (1) strongly coupled, resulting in approximately equal transverse mode emittances and (2) uncoupled, resulting in two drastically different emittances. Henceforth, let us refer to the beams in these configurations as "round" and "flat" beams, respectively. In both cases, the bunch length and the emittances depend on the beam current due to intrabeam scattering [89, 90], beam interaction with its environment [61], etc.

The longitudinal electron bunch density distribution $p_t(t)$ was measured with the help of a high-bandwidth wall-current monitor [62]. The signal from the wall-current monitor went to an oscilloscope passing through a long (≈ 100 m) cable and an amplifier on the way. The transmission functions of the long cable and the amplifier were measured with a spectrum analyzer. Then, the inverse of the full transmission function (in the Fourier space) was applied to the oscilloscope's waveforms. To achieve this, a special program was

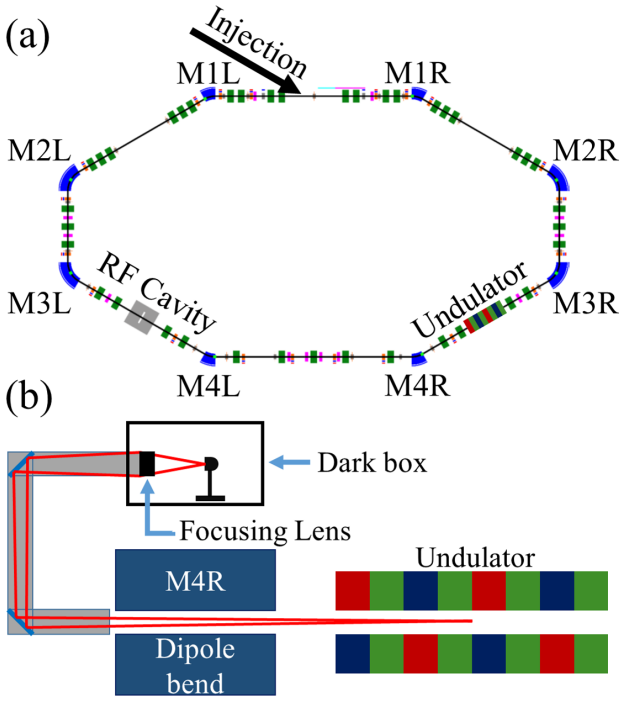

Figure 3.1: (a) Layout of the IOTA storage ring. The electrons circulate clockwise. (b) Light path from the undulator to the detector (not to scale).

developed. It was running on a Raspberry Pi 3b+ computer. It fetched the waveforms from the oscilloscope approximately twice per second, applied the transformation to reconstruct the original waveform from the wall-current monitor, and displayed the results on a webpage (created using the BOKEH library [91]), which could be accessed anywhere on the internal Fermilab network, called "Controls network". The program also calculated a number of useful parameters, such as the rms bunch length, the FWHM bunch length, the effective bunch length [Eqs. (2.77) and (2.79)], etc. These parameters were also sent to the Fermilab Accelerator Control System (ACNET). A screenshot of the program is shown in Fig. 3.2, the source code can be found in the code repository [92].

The longitudinal electron bunch density profile $p_t(t)$ was not exactly Gaussian (see Fig. 3.2), but this fact was properly accounted for by using the effective bunch length σ_z^{eff} [Eqs. (2.77) and (2.79)], which works for any longitudinal bunch shape. The rf cavity in IOTA operated at 30 MHz (4th harmonic of the revolution frequency) with a voltage am-

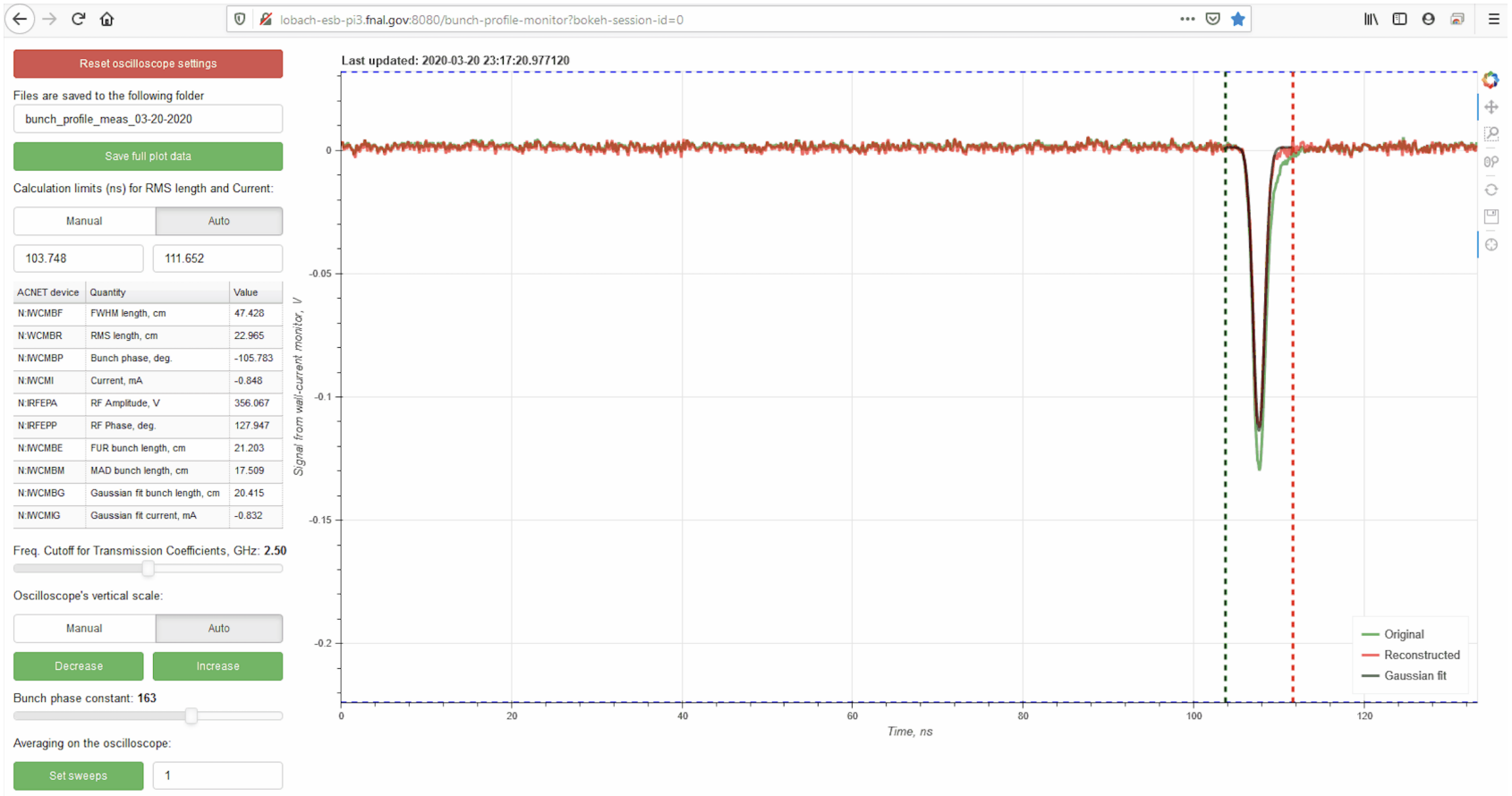

Figure 3.2: A screenshot of the computer program, reconstructing the longitudinal electron bunch density distribution in IOTA using the signal from the wall-current monitor.

plitude of about 360 V. The rms momentum spread σ_p was calculated from the known rf voltage amplitude, the design ring parameters and the measured rms bunch length σ_z. In our experiments, the relation was

$$\sigma_p \approx 9.1 \times 10^{-6} \times \sigma_z[\text{cm}]. \tag{3.1}$$

It is an approximate equation, because of the bunch-induced rf voltage (beam loading) and a small deviation of $p_t(t)$ from the Gaussian shape. However, the effect of σ_p in Eq. (2.105) in IOTA was almost negligible. Therefore, such estimation was acceptable.

For the round beam, the IOTA transverse focusing functions (4D Twiss functions) were chosen to produce approximately equal mode emittances at zero beam current, $\epsilon_1 \approx \epsilon_1 \approx 12\,\text{nm}$ (rms, unnormalized). It was empirically confirmed that they remained equal at all beam currents with a few percent precision. The expected zero-current emittances for a flat beam were $\epsilon_x \approx 50\,\text{nm}$, $\epsilon_y \gtrsim 0.33\,\text{pm}$ (set by the quantum excitation in a perfectly uncoupled ring). The expected zero-current rms bunch length and the rms momentum spread for both round and flat beams were $\sigma_z = 9\,\text{cm}$, $\sigma_p = 8.3 \times 10^{-5}$. In our experiment, the electron beam sizes were monitored and recorded by visible synchrotron light image monitors (SLMs) [80] in seven dipole bend locations, at M1L-M4L and at M1R-M3R, see Fig. 3.1(a) and Fig. 3.3. The smallest reliably resolvable emittance by the SLMs in our experiment configuration was about 20 nm. Figure 3.4 illustrates the bunch parameters of the round and flat beams in IOTA as functions of current. The beam current was measured with a direct-current current transformer (DCCT). The small vertical emittance of the flat beam was unresolvable by the SLMs. However, Section 3.5 will demonstrate that it can be reconstructed using the measured fluctuations.

At the center of the undulator, in the uncoupled optics, the Twiss parameters were $\beta_x = 204\,\text{cm}$, $\beta_y = 98\,\text{cm}$, $\alpha_x = 1.25$, $\alpha_y = -0.87$, the horizontal dispersion $D_x = 101\,\text{cm}$, its derivative $D_{x'} = -4.22$. The strongly coupled optics was created from the uncoupled

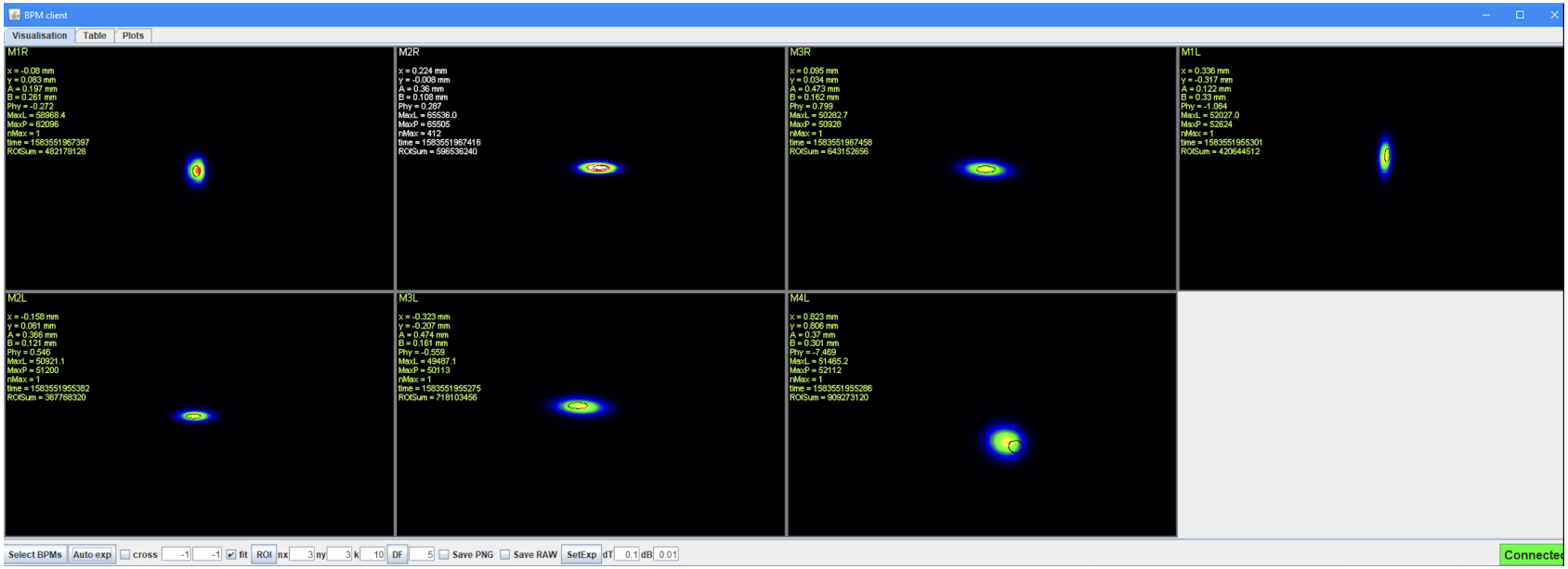

Figure 3.3: A screenshot of the computer program, measuring the electron beam sizes in IOTA. The images of the electron beam are generated by the bending-magnet radiation at seven different locations (at M1L-M4L and at M1R-M3R) around the ring.

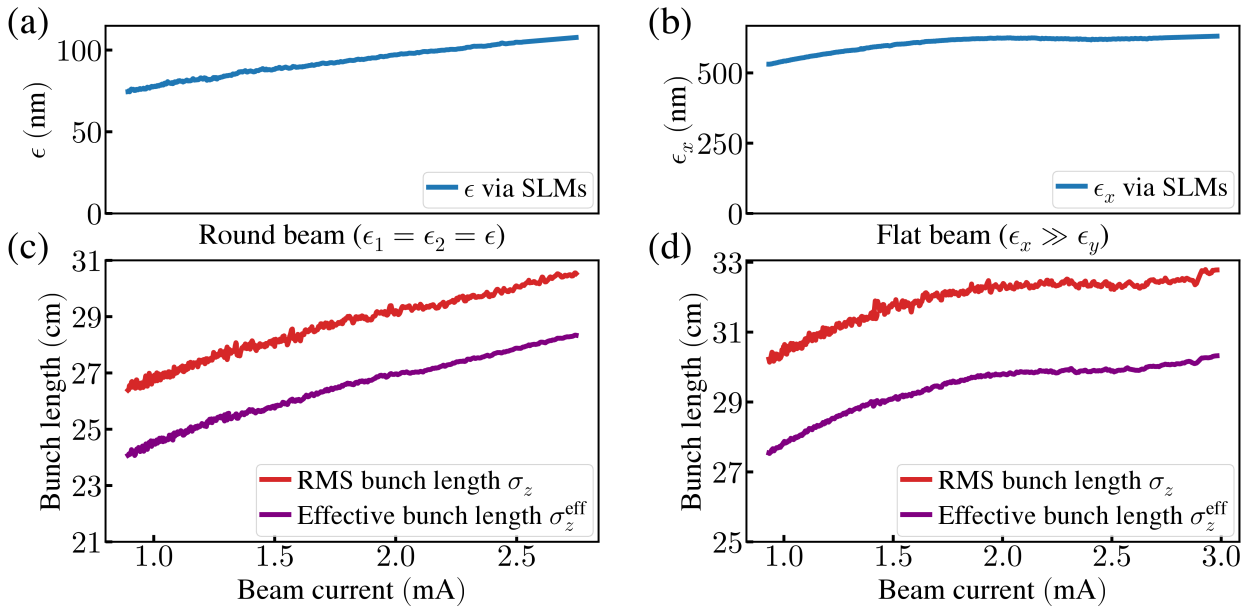

Figure 3.4: Panels (a) and (b) show the mode emittances ($\epsilon_1 = \epsilon_2 = \epsilon$) of a round beam and the horizontal emittance ($\epsilon_x \gg \epsilon_y$) of a flat beam, respectively, as functions of beam current in IOTA. The SLMs had a monitor-to-monitor spread of ± 8 nm (round beam) and ± 50 nm (horizontal emittance of flat beam); these error bars are not shown. All emittances are rms, unnormalized. Panels (c) and (d) present the bunch lengths (rms and effective) of round and flat beams, respectively.

optics by changing the current in one skew-quad located at a zero dispersion location. The coupling parameter u [93] was about 0.5 everywhere in the ring. Therefore, the following is correct for the coupled case 4D Twiss functions, $\beta_{1x} \approx \beta_{2x}$, $\beta_{1y} \approx \beta_{2y}$. Moreover, their sums, $\beta_{1x} + \beta_{2x}$, $\beta_{1y} + \beta_{2y}$, were approximately equal to the Twiss beta functions in the uncoupled case, β_x, β_y. Equation (2.105) assumes uncoupled optics. However, this specific strongly coupled optics used in IOTA can be approximated by the uncoupled optics with equal horizontal and vertical emittances $\epsilon_x = \epsilon_y = \epsilon$. More specifically, what is used in the derivation of Eq. (2.105) (see Section 2.5) is the 6D phase-space distribution of the electrons, Eq. (2.102). This distribution, for the round beam, when calculated using the approximation of uncoupled optics with equal emittances $\epsilon_x = \epsilon_y = \epsilon$, and the distribution, calculated using the exact 4D Twiss functions and equal mode emittances, $\epsilon_1 = \epsilon_2 = \epsilon$, are

almost indistinguishable. This property was intentionally included in the initial design of the coupled optics in IOTA. The Twiss beta-functions and the horizontal dispersion around the ring for the uncoupled focusing are shown in Fig. 3.5.

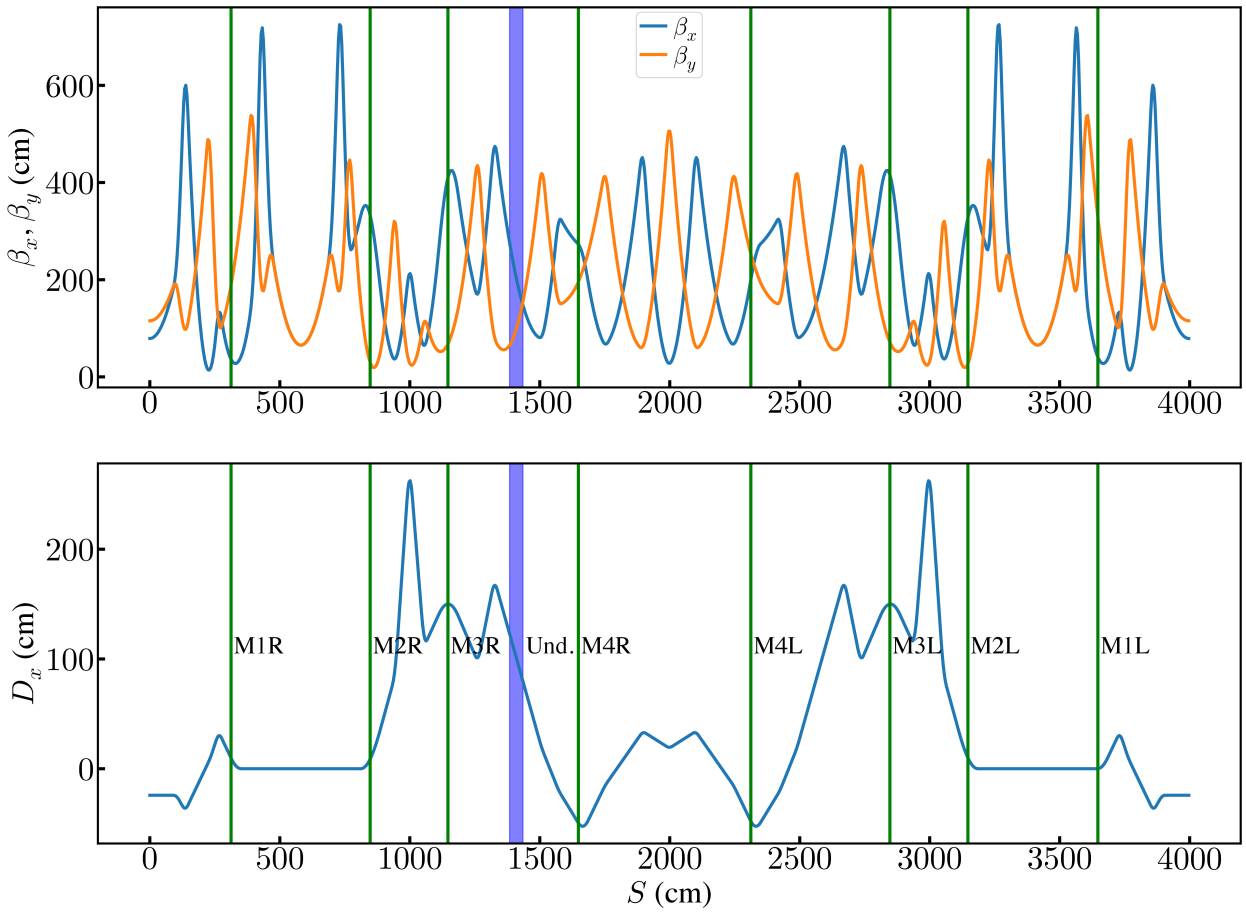

Figure 3.5: The Twiss beta-functions β_x and β_y and the horizontal dispersion D_x in the uncoupled focusing in IOTA. The horizontal axis S represents the position along the ring. The vertical green lines represent the locations of the SLMs, with the exception of M4R, where our photodiode was installed instead. The purple shaded area represents the location of the undulator.

The undulator strength parameter [see Eq. (2.88)] was $K_\mathrm{u} = 1.0$ with the number of periods $N_\mathrm{u} = 10.5$ and the period length $\lambda_\mathrm{u} = 5.5\,\mathrm{cm}$, the total length of the undulator was $L_\mathrm{u} = N_\mathrm{u}\lambda_\mathrm{u} = 58\,\mathrm{cm}$. A photodetector was installed in a dark box above the M4R dipole magnet, see Fig. 3.1(b). The light produced in the undulator was directed to the dark

box by a system of two mirrors (⌀2"). Then, it was focused by a lens (⌀2", focal distance $F = 150\,\mathrm{mm}$) into a spot, smaller than the sensitive area of the detector (⌀1.0 mm). The lens was 3.5 m away from the center of the undulator. Because of the two round mirrors, which are at 45° to the direction of propagation of the radiation, the angular aperture takes an elliptical shape with the vertical axis smaller than the horizontal by a factor of $\sqrt{2}$. Namely, the horizontal and the vertical semi-axes were 7.3 mrad and 5.1 mrad, respectively. The measurements were performed in the vicinity of the fundamental of the undulator radiation, $\lambda_1 = \lambda_\mathrm{u}(1 + K_\mathrm{u}^2/2)/(2\gamma^2) = 1.16\,\mu\mathrm{m}$. As a photodetector, an InGaAs *p-i-n* photodiode [72] was used, which has a high quantum efficiency ($\approx 80\,\%$) around the fundamental.

Using the elliptical angular aperture mentioned above and the manufacturers' specifications for the spectral transmission of the vacuum chamber window at the M4R dipole magnet, the two mirrors, the focusing lens, and the quantum efficiency of the InGaAs photodiode, it was possible to construct the detection efficiency function $\eta_{k,s}(\boldsymbol{\phi})$ for our system. The lens's spectral transmission had to be linearly extrapolated for a small interval outside of the range provided in the manufacturer's specifications. There were no free adjustable parameters. We calculated the field amplitude $\mathcal{E}_{k,s}(\boldsymbol{\phi})$, generated by a single electron, for the parameters of our undulator on a 3D grid (k, ϕ_x, ϕ_y) with our code [69]. Figure 3.6(a) shows the simulated spectrum, where the intensity is integrated over the elliptical aperture,

$$\frac{\mathrm{d}\,\langle \mathcal{N}_\mathrm{s.e.} \rangle}{\mathrm{d}k} = \sum_{s=1,2} \int \mathrm{d}^2\boldsymbol{\phi}\, \eta_{k,s}(\boldsymbol{\phi}) \left| \mathcal{E}_{k,s}(\boldsymbol{\phi}) \right|^2 . \tag{3.2}$$

The blue line is calculated for an ideal detection system, where $\eta_{k,s}(\boldsymbol{\phi}) = 1$ inside the elliptical aperture, and zero outside. The red line is calculated with $\eta_{k,s}(\boldsymbol{\phi})$, constructed using the manufacturers' specifications of the optical elements in our system. This $\eta_{k,s}(\boldsymbol{\phi})$ is equal to zero outside of the elliptical aperture. Whereas, inside, it is equal to the detection efficiency of our system. In our case, the detection efficiencies for the horizontal and vertical polarizations ($s = 1, 2$) are practically the same. Only the reflectance of the mirrors is

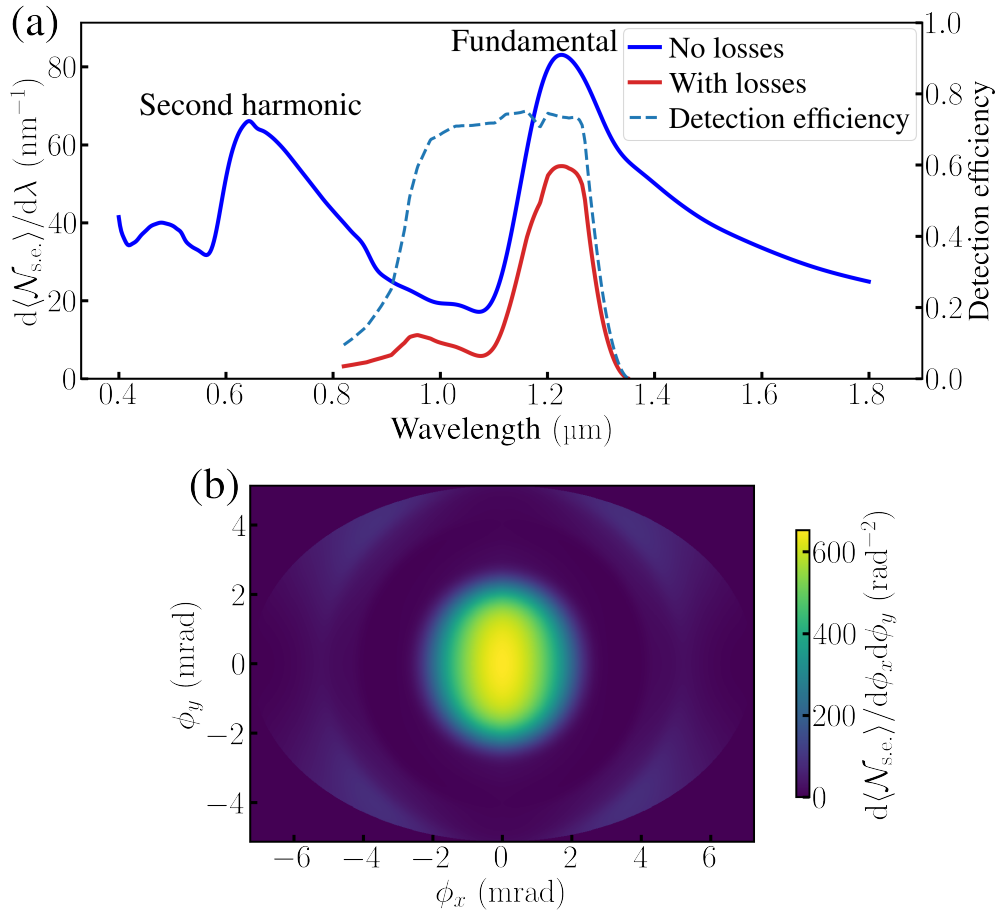

Figure 3.6: (a) Spectral distribution of the average number of detected photons per turn for a single electron (s.e.) assuming no losses (blue) and accounting for the detection efficiency of the system (red). Also, the detection efficiency (dashed, right vertical scale). (b) Angular distribution of the number of detected photons accounting for the detection efficiency of our system. Both (a) and (b) are calculated for an elliptical aperture with the horizontal and the vertical semi-axes 7.3 mrad and 5.1 mrad, respectively.

slightly polarization dependent (under 1 % difference). Moreover, the radiation is dominated by the horizontal polarization (about 96.5 %). The dashed line in Fig. 3.6(a) is the detection efficiency of our system for the horizontal polarization. Figure 3.6(b) shows the angular distribution with $\eta_{k,s}(\boldsymbol{\phi})$ of our system,

$$\frac{\mathrm{d}^2\langle\mathcal{N}_{\mathrm{s.e.}}\rangle}{\mathrm{d}\phi_x\mathrm{d}\phi_y} = \sum_{s=1,2}\int \mathrm{d}k\,\eta_{k,s}(\boldsymbol{\phi})\left|\mathcal{E}_{k,s}(\boldsymbol{\phi})\right|^2. \tag{3.3}$$

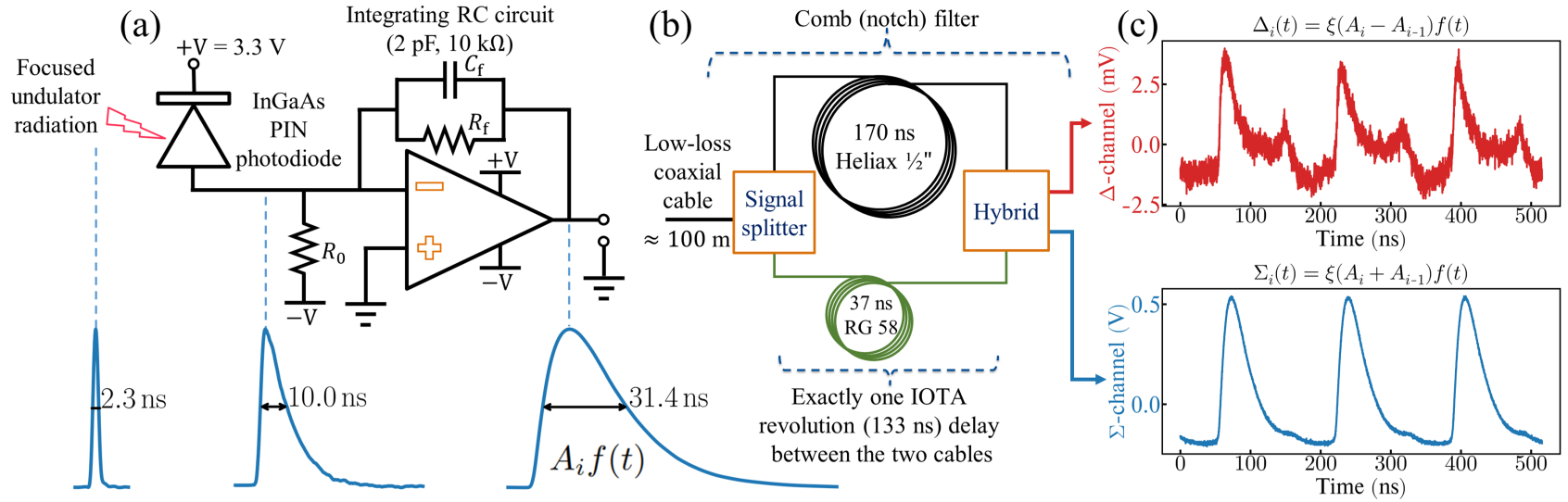

Figure 3.7: (a) Photocurrent integrator circuit. (b) Comb filter. (c) Sample waveforms of hybrid outputs (Δ- and Σ-channels).

With the spectral properties of all optical elements in the system taken into account, the spectral width of the radiation was 0.14 µm (FWHM), and the angular size was ≈ 2 mrad, which could be fully transmitted through the ⌀2" optical system.

Figure 3.7 illustrates our full photodetector circuit. First, the radiation pulse is converted into a photocurrent pulse by the photodiode, see Fig. 3.7(a). Then, the photocurrent pulse is integrated by an op-amp-based RC integrator, which outputs a longer pulse with a voltage amplitude that can be easily measured. The op-amp [94] was capable of driving the 50-Ω input load of a fast digitizing scope, located ≈ 100 m away. The resistor $R_0 = 580\,\mathrm{k}\Omega$ in the circuit in Fig. 3.7(a) was used to remove the offset in the integrator output signal (about 0.3 V), produced by the op-amp input bias current and the photodiode leakage current. The output voltage pulse of the integrator at the ith IOTA turn can be represented as $A_i f(t)$, where A_i is the signal amplitude at the ith turn and $f(t)$ is the average signal for one turn, normalized so that its maximum value is 1, see Fig. 3.7(a). The time t in $f(t)$ is in the range 0–133.3 ns, i.e., within one IOTA revolution. The number of photoelectrons, generated by the light pulse at the ith turn, $\mathcal{N}_i$, can be calculated as the time integral of the output pulse of the integrator divided by the electron charge e and the resistance R_f, i.e.,

$$\mathcal{N}_i = \int A_i f(t)\,\mathrm{d}t\,/(eR_\mathrm{f}). \tag{3.4}$$

The function $f(t)$ is known — it was measured with a fast oscilloscope. It was practically the same during all of our measurements, because $f(t)$ is rather wide (about 30 ns FWHM) and the length of the input light pulses was much smaller (about 2 ns FWHM); moreover, the shape of input pulses did not change significantly. Therefore, during all of our measurements

$$\mathcal{N}_i = \chi A_i, \tag{3.5}$$

where

$$\chi = \int f(t)\,\mathrm{d}t\,/(eR_\mathrm{f}) = 2.08 \times 10^7\,\text{photoelectrons/V}, \tag{3.6}$$

with a $\pm 5\,\%$ uncertainty, because of the uncertainty on R_f. Equation (3.5) was verified empirically at different voltage amplitudes A_i and different bunch lengths, which define the lengths of the input light pulses. During our experiments at different beam currents, A_i was in the range between 0 V and 1.2 V.

Since the empirical linear relation between the beam current and the integrator voltage amplitude was also known, it was possible to use it in Eq. (3.5) to find the average number of detected photons (photoelectrons) per one electron of the electron bunch. The result of this calculation was 8.8×10^{-3} photoelectrons/electron. This value is quite close to the result obtained in our simulation,

$$\sum_{s=1,2} \int \mathrm{d}k\,\mathrm{d}^2\boldsymbol{\phi}\,\eta_{k,s}(\boldsymbol{\phi}) \left|\mathcal{E}_{k,s}(\boldsymbol{\phi})\right|^2 = 9.1 \times 10^{-3}\,\text{photoelectrons/electron}. \tag{3.7}$$

In our experiment, the expected relative fluctuation of A_i was 10^{-4}–10^{-3} (rms), which is considerably lower than the digitization resolution of our 8-bit broad-band oscilloscope. To overcome this problem, a passive comb (notch) filter [95] was used, which is shown in Fig. 3.7(b). The signal splitter divides the integrator output into two identical signals. The lengths and the characteristics of the cables in the two arms were chosen such that one of the signals was delayed by exactly one IOTA revolution and, at the same time, the losses and dispersion in both arms were approximately equal. The time delay in the comb filter could be adjusted with a 0.1 ns precision. Therefore, the time delay error was negligible, because the pulses at the entrance of the comb filter were about 30 ns long (FWHM). Finally, a passive hybrid [96] generated the difference and the sum of the signals in the two arms —

its output channels Δ and Σ, respectively. For an ideal comb filter,

$$\Delta_i(t) = \xi(A_i - A_{i\text{-}1})f(t), \tag{3.8}$$

$$\Sigma_i(t) = \xi(A_i + A_{i\text{-}1})f(t), \tag{3.9}$$

where it is assumed that the pulse shape of input and output signals of the comb filter is the same — $f(t)$. This means that a negligible dispersion in the comb filter is assumed, which is a very good approximation according to our comparison of input and output pulses with the oscilloscope. Also, as a result of this comparison, it was determined that the parameter $\xi = 0.31$. Of course, our comb filter was not perfect. There was some cross-talk between Δ- and Σ-channels, some noise in the signals, a small undesirable reflection in one of the arms, resulting in a small satellite pulse about 85 ns away from the main pulse, see Fig. 3.7(c). In addition, the hybrid was AC-coupled.

With these effects taken into account Eqs. (3.8) and (3.9) take the form

$$\Delta_i(t) = \xi(A_i - A_{i\text{-}1})f(t) + \mu_\Delta \Sigma_i(t) + \delta_r A_i f(t - t_r) + \nu_{\Delta_i}(t) - \Delta_{\text{AC}}, \tag{3.10}$$

$$\Sigma_i(t) = \xi(A_i + A_{i\text{-}1})f(t) + \mu_\Sigma \Delta_i(t) + \delta_r A_i f(t - t_r) + \nu_{\Sigma_i}(t) - \Sigma_{\text{AC}}, \tag{3.11}$$

where t is within one IOTA turn (0–133.3 ns), μ_Δ and μ_Σ describe the cross-talk between Δ- and Σ-channels ($< 1\,\%$), $\delta_r A_i f(t - t_r)$ describes the reflected pulse in one of the arms (perhaps the short one), $t_r = 85\,\text{ns}$, $\delta_r \approx 1.5 \times 10^{-3}$; and it is assumed that the noise contributions $\nu_{\Delta_i}(t)$ and $\nu_{\Sigma_i}(t)$ enter the equations as sum terms, independent of the signal amplitude; the constants Δ_{AC} and Σ_{AC} come from the fact that the hybrid is AC-coupled and the averages of $\Delta_i(t)$ and $\Sigma_i(t)$ over a long time have to be zero.

For each measurement, 1.5 ms-long waveforms (about $n_{\text{rev}} = 11\,250$ IOTA revolutions) of Δ- and Σ-channels were recorded with the oscilloscope at 20 GSa/s. The beam current decay was negligible during this 1.5 ms acquisition period.

In Eq. (3.11), the noise, the cross-talk term, and the reflection term are negligible. The Σ-channel can be used to measure the photoelectron count mean $\langle \mathcal{N} \rangle$ during the 1.5 ms. Using Eq. (3.5) and the non-negligible part of Eq. (3.11),

$$\langle \mathcal{N} \rangle = \chi \frac{\big\langle \Sigma(t_{\text{peak}}) \big\rangle + \Sigma_{\text{AC}}}{2\xi}, \tag{3.12}$$

where t_{peak} was introduced — the time within each turn, corresponding to the peak of the signal, $f(t_{\text{peak}}) = 1$,

$$\big\langle \Sigma(t_{\text{peak}}) \big\rangle = \frac{1}{n_{\text{rev}}} \sum_{i=1}^{n_{\text{rev}}} \Sigma_i(t_{\text{peak}}). \tag{3.13}$$

The idea of using a comb filter is that, in the ideal case, see Eq. (3.8), the Δ-channel would provide the exact difference between two consecutive turns in IOTA. It would enable us to look directly at the turn-to-turn fluctuations. The offset would be removed, and the oscilloscope could be used with the appropriate scale setting, with negligible digitization noise. In our non-ideal comb filter, see Eq. (3.10), the additional terms have some impact on the Δ-signal, see Fig. 3.7(c). Nonetheless, by analyzing the Δ-signal in a special way, described below, it is possible to determine $\text{var}(\mathcal{N})$ with sufficient precision.

Namely, if one takes the variance of Eq. (3.10) with respect to i at a fixed time t, then the following result is obtained,

$$\text{var}(\Delta(t)) = 2\xi^2 \text{var}(A) f^2(t) + \text{var}(\nu_\Delta(t)), \tag{3.14}$$

where the contribution from $\mu_\Delta \Sigma_i(t)$ and $\delta_r A_i f(t)$ may be dropped, because the fluctuations of $\Sigma_i(t)$ and A_i are strongly attenuated by the factors μ_Δ and δ_r, respectively. Also, $\text{var}(\Delta_{\text{AC}}) = 0$ since Δ_{AC} is constant during the 1.5 ms. The left-hand side of Eq. (3.14), as a function of $t \in [0, 133.3]$ns, could be obtained from the collected waveforms of Δ-channel

as

$$\mathrm{var}(\Delta(t)) = \frac{1}{n_{\mathrm{rev}}} \sum_{i=1}^{n_{\mathrm{rev}}} \Delta_i^2(t) - \Big[\frac{1}{n_{\mathrm{rev}}} \sum_{i=1}^{n_{\mathrm{rev}}} \Delta_i(t)\Big]^2. \tag{3.15}$$

The results of such calculation for 2000 moments of time t within an IOTA revolution are shown in Fig. 3.8. These data are for the round beam. The blue, orange, and green lines correspond to three significantly different values of beam current within the range studied in our experiment; the red line corresponds to a zero beam current case.

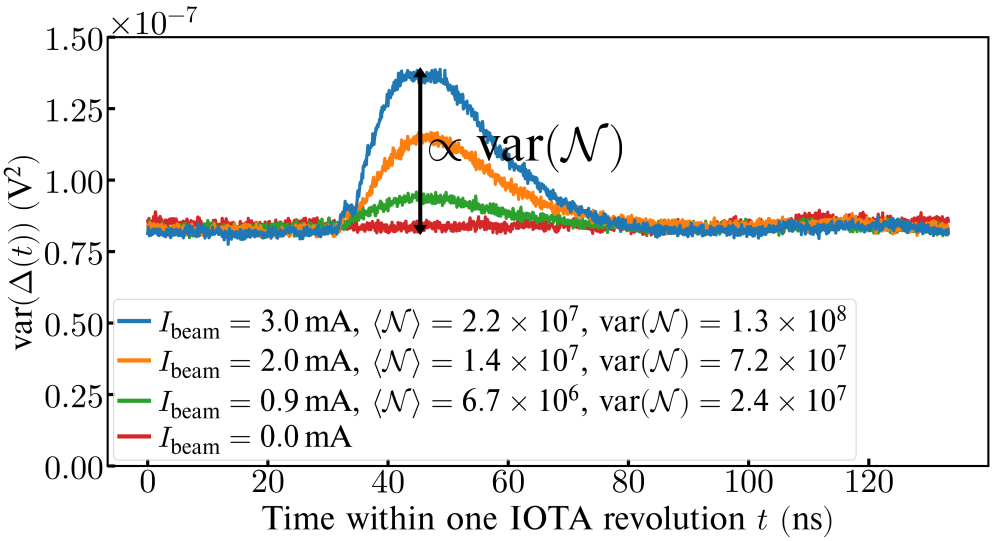

Figure 3.8: The variance of Δ-signal as a function of time [see Eq. (3.14)] within one IOTA revolution (round-beam data).

Figure 3.8 suggests that there is a constant noise level, which does not depend on time and signal amplitude. Specifically, it suggests that the noise term in Eq. (3.14) is

$$\mathrm{var}(\nu_\Delta(t)) = \mathrm{var}(\nu_\Delta) = 8.8 \times 10^{-8}\,\mathrm{V}^2. \tag{3.16}$$

The observed rms noise amplitude ($\approx 0.3\,\mathrm{mV}$) was analyzed by using the noise model for the detector electrical schematic, Figs. 3.7(a) and (b), as well as the typical electrical characteristics of the photodiode [72] and the operational amplifier [94]. The three main contributions to the rms noise in the Δ-channel are the following: the oscilloscope input amplifier noise,

0.21 mV; the operational amplifier input voltage noise, 0.18 mV; and the operational amplifier input current noise, 0.037 mV. When added in quadrature, these three sources explain the measured noise level.

The peaks rising above the noise level in Fig. 3.8 can be fitted well with $f^2(t)$ (fits not shown). Thus, their shape is in agreement with Eq. (3.14) as well.

Therefore, using Eqs. (3.5) and (3.14), the photoelectron count variance $\mathrm{var}(\mathcal{N})$ can be determined as

$$\mathrm{var}(\mathcal{N}) = \chi^2 \mathrm{var}(A) = \chi^2 \frac{\mathrm{var}(\Delta(t_{\mathrm{peak}})) - \mathrm{var}(\nu_\Delta)}{2\xi^2}, \tag{3.17}$$

see Eq. (3.15) for the definition of $\mathrm{var}(\Delta(t_{\mathrm{peak}}))$. The value of the noise level term in Eq. (3.17) is

$$\frac{\chi^2 \mathrm{var}(\nu_\Delta)}{2\xi^2} = 2.0 \times 10^8. \tag{3.18}$$

A dedicated test light source with known fluctuations was employed to verify this method of measurement of $\langle \mathcal{N} \rangle$ and $\mathrm{var}(\mathcal{N})$ [Eqs. (3.12) and (3.17)]. This verification is described in Section 3.3, where the statistical error of the measurement of $\mathrm{var}(\mathcal{N})$ by our apparatus is also estimated. Namely, the error is $\pm 2.7 \times 10^6$ — it is approximately constant in the range of $\mathrm{var}(\mathcal{N})$ observed with the undulator radiation in IOTA.

3.3 Measurements with a test light source

The method of determining $\langle \mathcal{N} \rangle$ and $\mathrm{var}(\mathcal{N})$ by Eqs. (3.12) and (3.17) was tested with an independent test light source with known fluctuations. The test light source consisted of a fast laser diode (1064 nm) with an amplifier, modulated by a pulse generator. The width of the light pulses and the repetition rate were very close to the experiment conditions in IOTA. However, the pulse-to-pulse fluctuations in the test light source were significantly greater than in the undulator radiation in IOTA, namely, $\mathrm{var}(\mathcal{N}) = 4 \times 10^9$ as opposed to $\mathrm{var}(\mathcal{N}) = 0$–$1.5 \times 10^8$ in IOTA. This also means that they were much greater than the

instrumental noise level of our apparatus, 2.0×10^8. Therefore, the relative fluctuations in the test light source could be reliably measured, even without subtraction of the noise level, because it was negligible. The result was

$$\theta = \frac{\mathrm{var}(\mathcal{N})}{\langle \mathcal{N} \rangle^2} = 3.31 \times 10^{-6}, \tag{3.19}$$

which corresponds to the rms value 1.82×10^{-3}. These fluctuations primarily came from the jitter in the pulse generator amplitude.

Further, neutral density filters were used to lower the number of photons detected by our apparatus. Neutral density filters are filters that have constant optical density in the wavelength region of interest. As they lower $\langle \mathcal{N} \rangle$ for the test light source, $\mathrm{var}(\mathcal{N})$ is lowered in the following known way,

$$\mathrm{var}(\mathcal{N}) = \langle \mathcal{N} \rangle + \theta \langle \mathcal{N} \rangle^2 , \tag{3.20}$$

i.e., the relative fluctuations stay practically constant $\mathrm{var}(\mathcal{N}) / \langle \mathcal{N} \rangle^2 \approx \theta$, because they are caused by the pulse generator amplitude jitter, but at a very low $\langle \mathcal{N} \rangle$ the photon shot noise term [the first term in Eq. (3.20)] may have a noticeable contribution, similar to Eq. (2.69). By using many different neutral density filters and their combinations, Δ- and Σ-channel waveforms were recorded for a wide range of $\mathrm{var}(\mathcal{N})$, see Fig. 3.9(a), including the range observed in our experiment in IOTA, shown in Fig. 3.9(b) and highlighted by a red rectangle in Fig. 3.9(a).

In Figs. 3.9(a) and (b), the parameter θ of the red predicted curve was obtained in a configuration without any neutral density filters, when the detector noise and the photon shot noise were negligible, see Eq. (3.19). The blue fluctuation data points, obtained from the Δ- and Σ-channel waveforms using Eqs. (3.12) and (3.17), agree with the red predicted curve in the entire range of $\mathrm{var}(\mathcal{N})$, including the range of Fig. 3.9(b) corresponding to the measurements in IOTA. This means that the method of extracting $\mathrm{var}(\mathcal{N})$ from the

waveforms, described in Fig. 3.8 and Eq. (3.17), works well, and that the instrumental noise [$\mathrm{var}(\nu_\Delta) = 2.0 \times 10^8$] does not depend on the signal amplitude indeed.

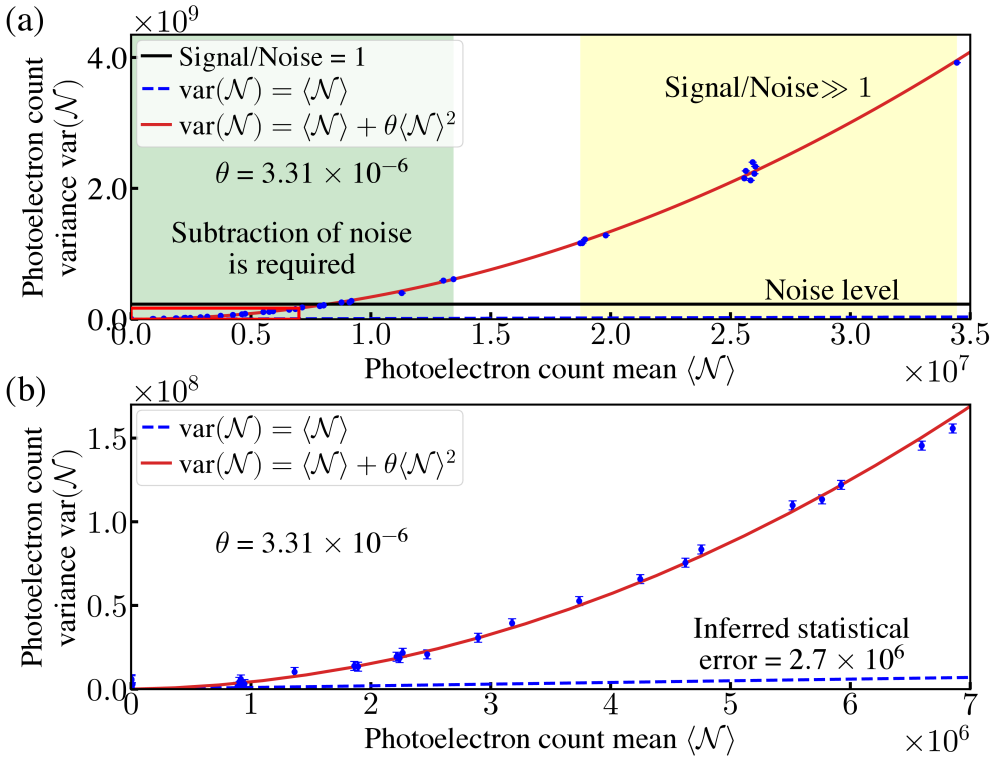

Figure 3.9: Photoelectron count variance $\mathrm{var}(\mathcal{N})$ as a function of photoelectron count mean $\langle\mathcal{N}\rangle$ for the test light source; $\langle\mathcal{N}\rangle$ was varied by using different neutral density filters. (a) The entire range of $\langle\mathcal{N}\rangle$ and $\mathrm{var}(\mathcal{N})$. (b) The region corresponding to the values of $\mathrm{var}(\mathcal{N})$ generated by the undulator radiation in IOTA [highlighted by the red rectangle in (a)].

Further, the statistical error of our measurement of photoelectron count variance in IOTA was estimated as the rms deviation of the fluctuation data points for the test light source from the predicted curve in Fig. 3.9(b). The error is $\pm 2.7 \times 10^6$. It is used in the error bars in Fig.3.9(b), Fig. 3.10(a), and Figs. 3.11(a),(b) .

3.4 Comparison of measured and simulated fluctuations at IOTA

The measured fluctuations data for the round beam at different values of beam current are shown in Fig. 3.10(a) (blue points). The blue dashed straight line, $\mathrm{var}(\mathcal{N}) = \langle\mathcal{N}\rangle$, represents

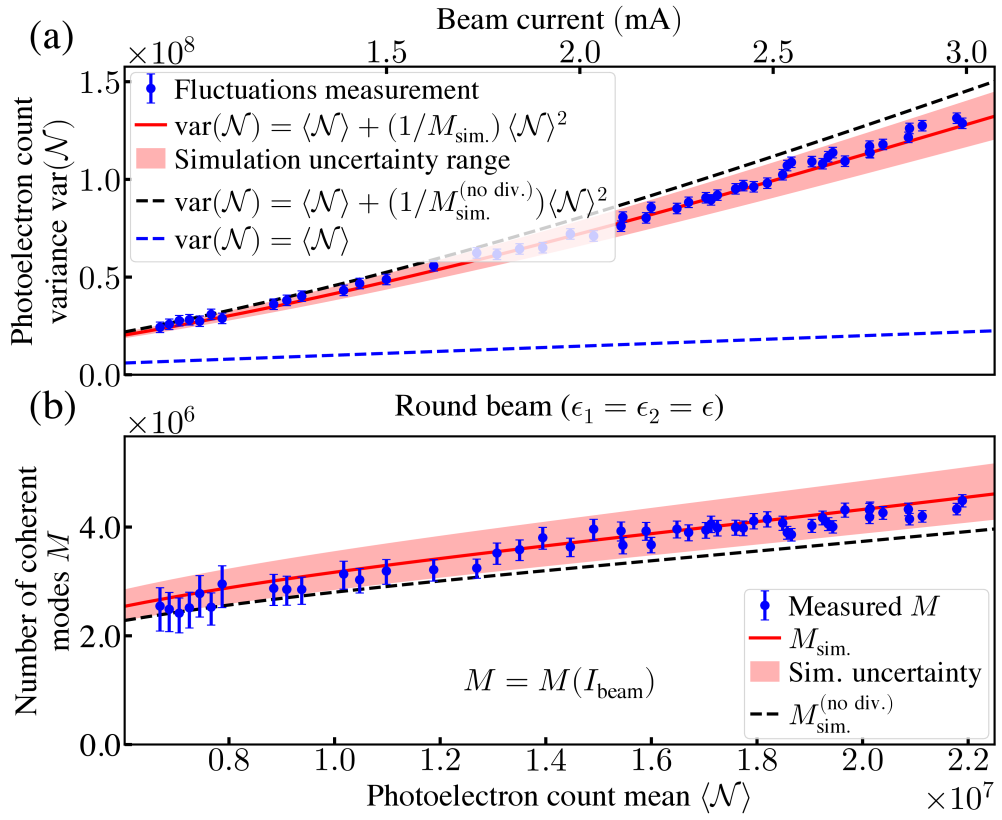

Figure 3.10: Panel (a) presents the fluctuations measurement for the round electron beam in IOTA as a function of beam current, a prediction by Eq. (2.105) (red solid line), and a prediction by Eq. (2.82) (black dashed line), which does not account for the beam divergence. Panel (b) presents the data of (a) in terms of the number of coherent modes M.

the photon shot noise contribution to the fluctuations — the first sum term in Eq. (2.69). The values of M extracted from the fluctuation data points using the equation,

$$M = \langle \mathcal{N} \rangle^2 / (\mathrm{var}(\mathcal{N}) - \langle \mathcal{N} \rangle), \tag{3.21}$$

are shown in Fig. 3.10(b) (blue points). The error bars in Figs. 3.10(a),(b) correspond to the $\pm 2.7 \times 10^6$ statistical error of measurement of var($\mathcal{N}$) by our technique. Further, Fig. 3.10(b) has a curve for M, simulated by Eq. (2.105) (red line), and, for comparison, a curve for M, simulated by Eq. (2.82) (dashed black line), which neglects beam divergence. Corresponding curves for simulated var($\mathcal{N}$) are shown in Fig. 3.10(a). The shaded light red

areas in Figs. 3.10(a),(b) show the uncertainty range of our simulation by Eq. (2.105).

For this simulation, it was necessary to know the values of the following four bunch parameters, entering Eq. (2.105), ϵ_x, ϵ_y, σ_p, $\sigma_z^{\rm eff}$, at all beam currents. Further, it was necessary to know the values of Twiss functions in the undulator, the parameters of the undulator and of the detection system. All these aspects were described in Section 3.2. There were no free parameters in this simulation. Numerical calculation of the integrals in Eq. (2.105) and Eq. (2.82) was performed by the Monte-Carlo algorithm on the Midway2 cluster at the University of Chicago Research Computing Center using our computer code [69, 77].

The simulation uncertainty range (shaded light red area) primarily comes from the uncertainty in the beam energy $96.4 \pm 1\,\text{MeV}$. The next source of uncertainty by magnitude, which is a factor of two smaller, is the SLMs' $\pm 8\,\text{nm}$ monitor-to-monitor variation of ϵ [for the round beam, one can use $\epsilon_x = \epsilon$ and $\epsilon_y = \epsilon$ in Eq. (2.105)]. The uncertainties of other parameters (σ_p, $\sigma_z^{\rm eff}$, Twiss functions in the undulator, etc.) had negligible effect. The manufacturers' specifications for the optical elements of our system did not provide any uncertainties. Therefore, they were not considered.

The fluctuations predicted by Eqs. (2.69) and (2.105) in the round beam configuration agree with the measurements within the uncertainties, as shown in Figs. 3.10(a),(b). In the round beam case, at the beam current value 2.66 mA, for example, the electron beam divergence in the undulator was about 0.43 mrad (both x and y). It was noticeably smaller than the rms radiation divergence $\sqrt{\lambda_1/(2L_{\rm u})} = 1.0\,\text{mrad}$ [2, Eq. (2.57)], which gives an estimate of the angular size of $\mathcal{E}_{k,s}(\boldsymbol{\phi})$. Therefore, the effect of beam divergence on the fluctuations simulation in Figs. 3.10(a),(b) is not too dramatic. However, the deviation from the measurement of the simulation based on Eq. (2.82), which neglects beam divergence, is certainly noticeable, whereas the simulation by Eq. (2.105) agrees well with the measurement.

The measured fluctuations data for the flat beam at different values of beam current are

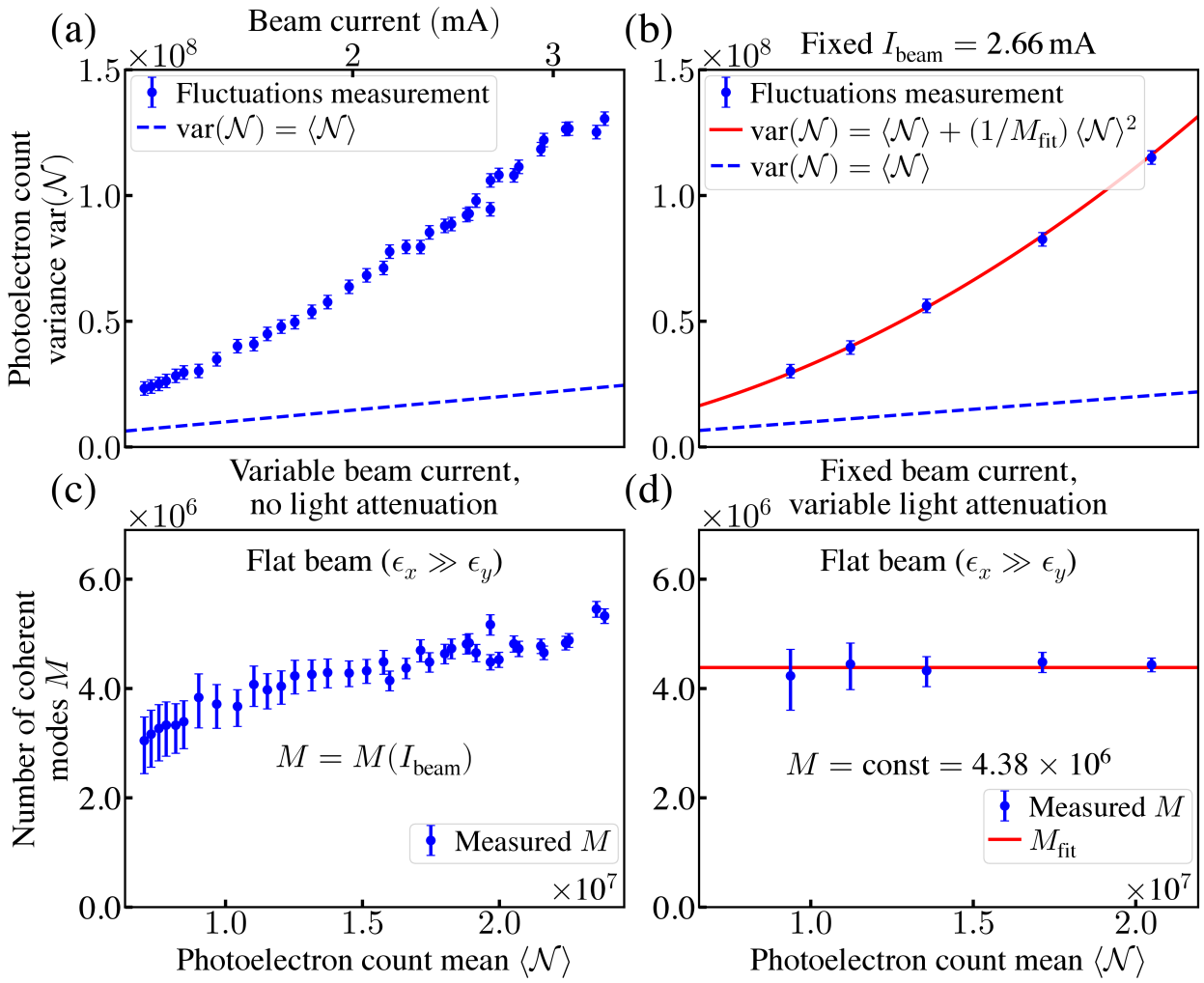

Figure 3.11: Panel (a) presents the fluctuations measurement for the flat electron beam in IOTA as a function of beam current. Panel (b) presents the fluctuations measurement for the flat electron beam at a fixed beam current 2.66 mA with 4 different optical neutral density filters and one point without any filters, as well as a parabolic fit. Predictions for the flat beam could not be made, because the vertical emittance of the flat beam was unknown. Panels (c) and (d) present the data of (a) and (b) in terms of the number of coherent modes M.

shown in Fig. 3.11(a). The values of M extracted from the fluctuation data points using Eq. (3.21) are shown in Fig. 3.11(c). For a flat beam, fluctuations data have also been collected for another experiment configuration. Namely, Fig. 3.11(b) shows fluctuation data points for a flat beam at a fixed beam current 2.66 mA. The corresponding reconstructed

values of M are shown in Fig. 3.11(d). In this measurement, the photoelectron count mean (horizontal axis) was varied by using different optical neutral density filters (one point without a filter and four points with filters). Neutral density filters are filters that have constant attenuation in a certain wavelength range; in our case, around the fundamental harmonic of the undulator radiation. A new bunch was injected into the ring for each measurement. The oscilloscope waveforms for Δ- and Σ-channels were recorded when the beam current decayed to 2.66 mA. The red curve in Fig. 3.11(b) is a fit with a constant M. A corresponding horizontal line is shown in Fig. 3.11(d). The value of M in this fit is $M_{\text{fit}} = (4.38 \pm 0.10) \times 10^6$. This value was calculated as the average of the five values of M in Fig. 3.11(d), and the error was calculated as the standard deviation of these five values. All error bars in Fig. 3.11 correspond to the $\pm 2.7 \times 10^6$ statistical error of measurement of $\text{var}(\mathcal{N})$ by our apparatus.

In IOTA, the bunch parameters ϵ_x, ϵ_y, σ_p, σ_z^{eff} depend on the beam current [see Fig. 3.4] because of various intensity dependent effects, e.g., intrabeam scattering [97], beam interaction with its environment [61], etc. Therefore, M is a function of the beam current too, as one can see in Fig. 3.10(b) and in Fig. 3.11(c). In Figs. 3.11(b),(d), however, all data points correspond to one value of the beam current, 2.66 mA. The photoelectron count mean is varied by using neutral density filters with different attenuation factors η_{ND}. Such filters linearly scale down the photoelectron count mean, $\langle \mathcal{N} \rangle \to \eta_{\text{ND}} \langle \mathcal{N} \rangle$. However, they do not change M, because if $\eta_{k,s}(\boldsymbol{\phi})$ is replaced by $\eta_{\text{ND}} \eta_{k,s}(\boldsymbol{\phi})$ in Eq. (2.105), then η_{ND} cancels out in the numerator and the denominator. This is consistent with Fig. 3.11(d) — all measured values of M are equal within the uncertainty range. This is one more confirmation that our understanding of the origin of the fluctuations $\text{var}(\mathcal{N})$ is likely correct.

No simulation results are presented for the fluctuations $\text{var}(\mathcal{N})$ in the uncoupled focusing, because the SLMs provided very inconsistent estimates for the small vertical emittance ϵ_y of the flat beam — the max-to-min variation for different SLMs reached a factor of eight. We believe this happened because the beam images were close to the resolution limit, set

by a combination of factors, such as the diffraction limit, the point spread function of the cameras, chromatic aberrations, the effective radiator size of the dipole magnet radiation ($\approx 20\,\mu\text{m}$), and the camera pixel size ($\approx 10\,\mu\text{m}$ in terms of beam size). Therefore, the monitor-to-monitor emittance value variation primarily came from the Twiss beta-function variation ($\beta_y^{(\max)}/\beta_y^{(\min)} \approx 12$). The diffraction limit is primarily caused by the irises, used to reduce the radiation intensity to prevent the cameras from saturating at high beam currents. Alternatively, leaving the irises open and using attenuating optical filters may improve the resolution. Additional negative effects include the errors in the light focusing optics, calibration errors of the SLMs, and possible Twiss beta-function errors. The SLMs at locations with larger beta-functions (M4L, M1L) provide estimates for ϵ_y that agree better with the theoretical predictions [98] at lower beam currents, and with the emittance estimates presented below in this section. Nevertheless, this is not enough to claim that the SLMs could provide a reliable estimate for ϵ_y during our experiment.

Without ϵ_y one cannot use Eq. (2.105) to make a prediction for M and $\text{var}(\mathcal{N})$. However, it is possible to attempt the reverse of this procedure. One can estimate the emittance of the electron bunch based on the measured magnitude of the fluctuations of the number of detected photons $\text{var}(\mathcal{N})$. This will be discussed in the next section, dedicated specifically to this idea.

3.5 Transverse beam emittance measurement by undulator radiation power noise

The measured value of the number of coherent modes M_{meas} is a function of four bunch parameters,

$$M_{\text{meas}} = M(\epsilon_x, \epsilon_y, \sigma_p, \sigma_z^{\text{eff}}). \tag{3.22}$$

The full form of the right-hand side is given by Eq. (2.105). When only one of the four parameters is unknown, one can numerically solve Eq. (3.22), using our general formula for M [Eq. (2.105)], to find the unknown bunch parameter. In IOTA, the electron bunch length is around 20–30 cm and it could be easily measured with the wall-current monitor. Therefore, we were not interested in measuring it using the fluctuations of the number of detected photons. However, it was interesting to try measuring the transverse emittances of the electron bunch using the fluctuations-based technique.

3.5.1 Flat beam. Fixed beam current. Different neutral density filters

Let us start with the flat-beam data from Figs. 3.11(b),(d). These data points were all collected at the same value of beam current 2.66 mA. Therefore, all four bunch parameters $\epsilon_x, \epsilon_y, \sigma_p, \sigma_z^{\text{eff}}$ were the same during each measurement. The horizontal emittance ϵ_x of the flat beam at a beam current of 2.66 mA could still be reliably measured via the SLMs, yielding $\epsilon_x = 0.66\,\mu\text{m}$. The effective bunch length σ_z^{eff} could be determined from $p_t(t)$ measured by the wall-current monitor, $\sigma_z^{\text{eff}} = 29.5\,\text{cm}$. The rms momentum spread σ_p was estimated from $p_t(t)$ and the ring parameters, $\sigma_p = 3.0 \times 10^{-4}$. The only unknown in Eq. (3.22) is ϵ_y. Equation (3.22) can be solved for ϵ_y by a simple bisection method. The result is $\epsilon_y = 8.4 \pm 1.5\,\text{nm}$, where the uncertainty corresponds to the statistical error of M_{fit}, mentioned above. For comparison, if one uses Eq. (2.82) in Eq. (3.22), which neglects beam divergence, then the following result is obtained, $\epsilon_y = 18.3 \pm 1.3\,\text{nm}$. This shows that, for the flat beam, accounting for the beam divergence is critical. In this measurement, the horizontal beam divergence was 0.94 mrad and comparable with the rms radiation divergence $\sqrt{\lambda_1/(2L_{\text{u}})} = 1.0\,\text{mrad}$ [2, Eq. (2.57)], which gives an estimate of the angular size of $\mathcal{E}_{k,s}(\boldsymbol{\phi})$. Clearly, in this case it has a significant effect on the integral in the numerator of Eq. (2.105). This is why Eq. (2.105) is used further in this section.

In this reconstruction of ϵ_y, there is also a systematic error due to the uncertainty on

the beam energy (± 1 MeV) and due to the systematic error of ϵ_x measurement by the SLMs (± 50 nm monitor-to-monitor). We estimated these two contributions to the systematic error of ϵ_y, when ϵ_y is determined using Eq. (2.105). They are $^{+2.5}_{-4.5}$ nm and $^{+1.6}_{-1.4}$ nm, respectively. These systematic errors are rather significant. However, they are not directly linked to our measurement technique. They are related to the fact that the beam energy and the horizontal emittance of a flat beam in IOTA were not known with better precision. Further improvements in beam characterization in IOTA will reduce the systematic error of our fluctuations-based technique of ϵ_y measurement.

3.5.2 Flat-beam and round-beam data. Variable beam current

The fluctuations-based procedure for the reconstruction of vertical emittance ϵ_y of the flat beam was repeated for each point of the fluctuations data shown in Figs. 3.11(b),(d), where neutral density filters were not used and the beam current was varied instead. The results are shown in Fig. 3.12(a). In addition to the statistical error of ϵ_y, shown in Fig. 3.12(a), there was also a systematic error due to the 1 MeV uncertainty on the beam energy (from 2.5 nm at lower currents to 5 nm at higher currents), and a systematic error due to the 50 nm uncertainty on ϵ_x (from 1.3 nm at lower currents to 2.4 nm at higher currents). The measured vertical emittance is 5–15 nm, most likely due to a nonzero residual transverse coupling. The expected zero-current flat-beam emittances were $\epsilon_x \approx 50$ nm, $\epsilon_y \gtrsim 0.33$ pm (set by the quantum excitation in a perfectly uncoupled ring). The smallest reliably resolvable emittance by the SLMs in our experiment configuration was ≈ 20 nm.

In addition to determining the unknown vertical emittance of the flat beam, it was also decided to apply our fluctuations-based technique to the round-beam data from Fig. 3.10. Indeed, since the transverse mode emittances are made equal by design $\epsilon_1 = \epsilon_2 = \epsilon$, there is only one unknown ϵ and it can be determined using one measured value M_{meas} and Eq. (2.105). The results are shown as the red points in Fig. 3.12(b). This fluctuations-

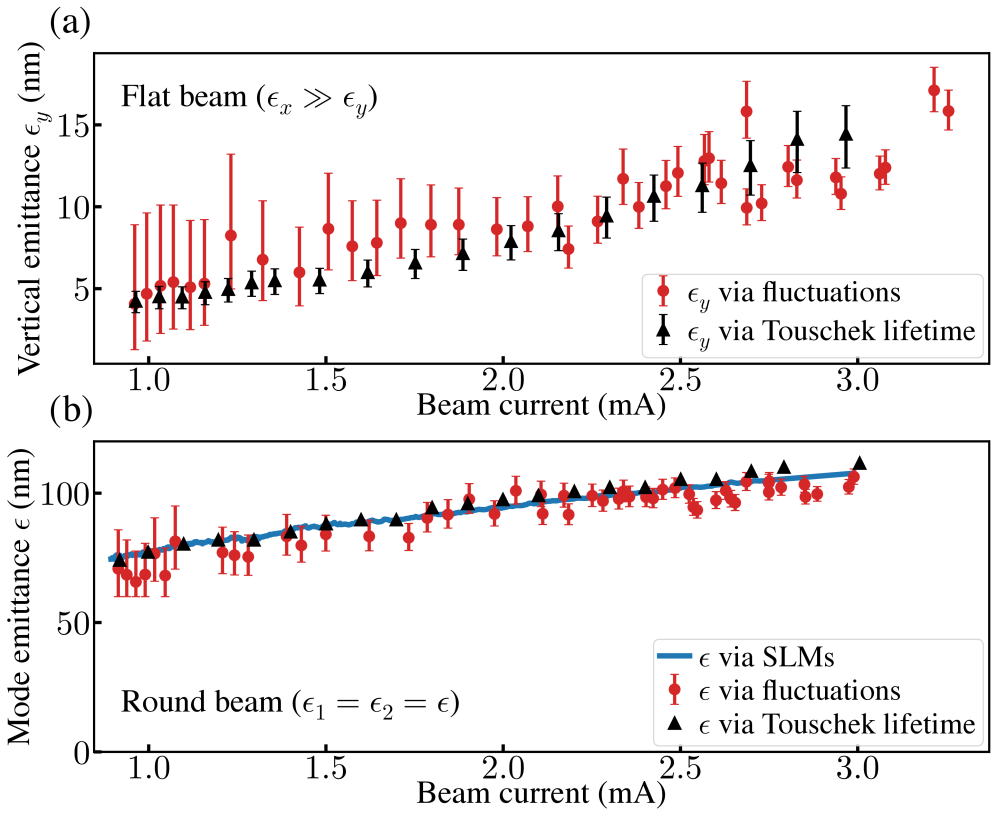

Figure 3.12: Panel (a) presents the flat-beam vertical emittance, determined via fluctuations and via Touschek lifetime. Panel (b) shows the round-beam mode emittance ϵ, determined via SLMs, via undulator radiation fluctuations, and via Touschek lifetime, assuming the effective momentum acceptance 2.0×10^{-3}. The SLMs had a monitor-to-monitor spread of ± 8 nm for the mode emittance ϵ of the round beam, these error bars are not shown. All emittances are rms, unnormalized.

based measurement agrees well with the measurement via SLMs [blue line in Fig. 3.12(b)]. Of course, this was expected given the good agreement between the measurement and the simulation in Figs. 3.10(a),(b). The measured round-beam emittance ϵ is 75–100 nm (rms, unnormalized), primarily due to intrabeam scattering [89, 90]. The expected zero-current value is $\epsilon \approx 12$ nm.

The fact that our fluctuations-based technique works well for the round-beam adds credibility to our fluctuations-based measurements of the small vertical emittance ϵ_y of the flat beam [Fig. 3.12(a)], which is unresolvable by the SLMs. However, it was decided to estimate the vertical emittance of the flat beam in one more independent way — using the measured

beam lifetime and a prediction for it, assuming Touschek scattering as the main particle loss mechanism.

3.5.3 Emittance estimate via Touschek beam lifetime

An independent estimate of the vertical emittance ϵ_y of the flat beam could be made based on the beam lifetime. The beam lifetime could be reliably determined from the measured beam current I as a function of time, as $|I/(\mathrm{d}I/\mathrm{d}t)|$. During all of our measurements the beam current was measured with a DCCT current monitor, it was reported every second. Further, the waveforms from the wall-current monitor allowed us to see the distribution of the electrons among the 4 rf buckets in IOTA. The DCCT current was always corrected to only account for the main bucket. Typically, the combined population of the remaining 3 buckets was no more than a few percent. At the beam currents encountered in our experiment (1–3 mA), the beam lifetime is determined solely by Touschek scattering [93, 98, 99]. In general, the momentum acceptance is a function of the position along the ring. It is limited by the longitudinal bucket size δ_{rf} and by the dynamic momentum aperture. A constant effective momentum acceptance $\delta_{\mathrm{acc}}^{(\mathrm{eff})}$ can be used [100] to describe the losses due to Touschek scattering. It is equal to or smaller than δ_{rf}. The approach described in [101, 102] was used to calculate the Touschek lifetime. Figure 3.13 shows the measured beam lifetime for the round beam (blue points), a calculation with the momentum acceptance limited only by the rf bucket size $\delta_{\mathrm{rf}} = 2.8 \times 10^{-3}$ (green diamonds), and a calculation with an effective momentum acceptance $\delta_{\mathrm{acc}}^{(\mathrm{eff})} = 2.0 \times 10^{-3}$ (orange triangles).

The calculation with $\delta_{\mathrm{acc}}^{(\mathrm{eff})} = 2.0 \times 10^{-3}$ almost perfectly agrees with the measurement. The emittances and the beam lifetime of the round beam are known with good accuracy, the only unknown in this Touschek lifetime calculation for the round beam being $\delta_{\mathrm{acc}}^{(\mathrm{eff})}$. We believe that Fig. 3.13 illustrates that in IOTA $\delta_{\mathrm{acc}}^{(\mathrm{eff})} = 2.0 \times 10^{-3}$.

Further, this Touschek lifetime calculation (with $\delta_{\mathrm{acc}}^{(\mathrm{eff})} = 2.0 \times 10^{-3}$) can be applied to

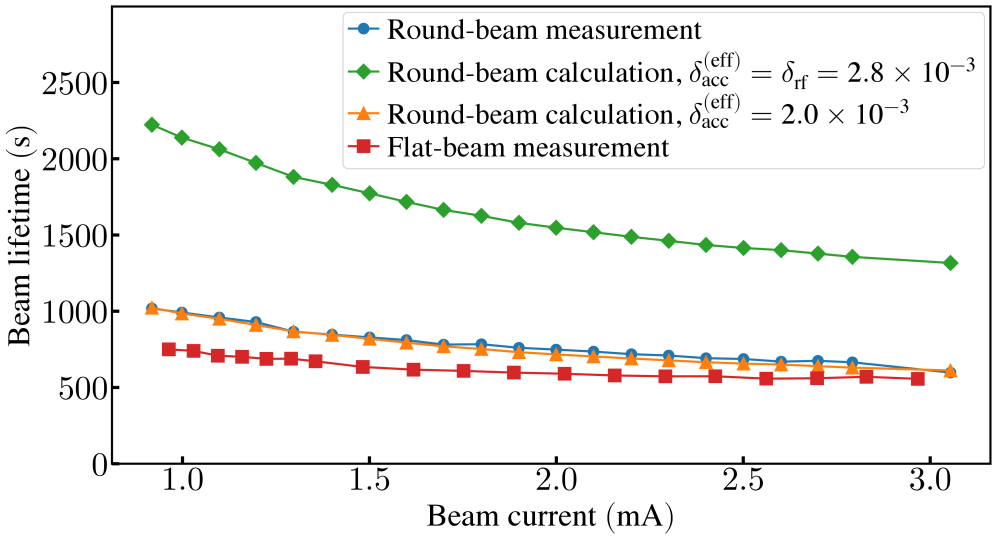

Figure 3.13: Lifetimes of round and flat beams in IOTA as functions of beam current.

the flat beam data, shown in Fig. 3.13 as red squares. In this case, the only unknown is ϵ_y. The values of ϵ_y determined in this way are shown in Fig. 3.12(a) as black triangles. The error bars come from the $\pm 50\,$nm uncertainty on ϵ_x of the flat beam. Other sources of error are much smaller: $\pm 5\,$sec uncertainty on the measured beam lifetime, uncertainties in the beam energy, Twiss-functions, and bunch length. The lifetime-based estimates of ϵ_y agree with the fluctuations-based measurements within the uncertainty.

For the flat-beam data collected with different neutral density filters at the beam current $2.66\,$mA [Figs. 3.11(b),(d)], the fluctuations-based estimate for the vertical emittance was $\epsilon_y = 8.4 \pm 1.5\,$nm. The lifetime-based estimate is $\epsilon_y = 9.6 \pm 1.2\,$nm. Again, these two estimates agree within the uncertainties. The black triangles in Fig. 3.12(b) illustrate the emittance ϵ of the round beam if it were to be determined from the measured beam lifetime using the Touschek lifetime calculation with $\delta_{\rm acc}^{\rm (eff)} = 2.0 \times 10^{-3}$.

3.5.4 Discussion

Other emittance monitors (wire scanners, Compton-scattering monitors [103, 104]) could provide better resolution in IOTA. However, if a bright synchrotron light source is available,

our fluctuations-based monitor may be a good inexpensive non-invasive alternative. There are two requirements for the technique to work: (A) the fluctuations should not be dominated by the Poisson noise, so that M can be reliably deduced from var($\mathcal{N}$), and (B) M has to be sensitive to ϵ_x, ϵ_y. Let us consider the hth harmonic of undulator radiation in the approximation of Eqs. (2.116) and (2.117) with a narrow Gaussian filter $\sigma_k \ll k_0/(hN_\mathrm{u})$ and $k_0 = 2\pi h/\lambda_1$. By integrating Eq. (2.116) one can obtain $\langle\mathcal{N}\rangle = C(2\pi)^{3/2}\sigma_{r,x'}\sigma_{r,y'}\sigma_k$, where C is the peak on-axis photon flux, $C = \alpha N_\mathrm{u}^2\gamma^2 F_h(K_\mathrm{u})n_e/k_0$ [68, p. 68], α is the fine-structure constant, n_e is the number of electrons per bunch, and the function $F_h(K_\mathrm{u})$, defined in [68, p. 69], is typically about 0.2–0.4. If one approximates Eq. (2.117) by $M \approx 8\,k_0^2\,\sigma_k\sigma_{r,x'}\sigma_{r,y'}\sigma_x\sigma_y\sigma_z$, the requirement (A) becomes [see Eq. (2.69)]

$$\frac{\langle\mathcal{N}\rangle}{M} = \alpha\left(\frac{\pi}{2}\right)^{\frac{3}{2}} F_h(K_\mathrm{u})\frac{\gamma^2 N_\mathrm{u}^2 n_e}{\sigma_x\sigma_y\sigma_z k_0^3} \gtrsim 1. \tag{3.23}$$

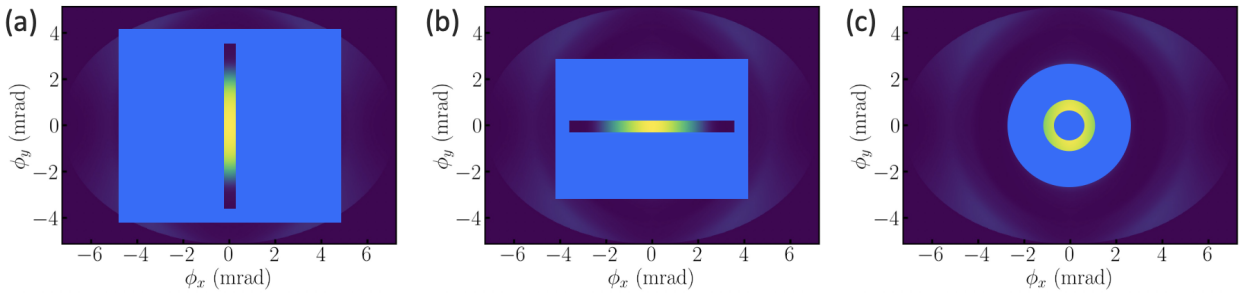

Figure 3.14: Illustration of the slits and masks that can be used to improve the fluctuations-based technique for determination of the electron bunch parameters. The original angular intensity distribution without any slits or masks is shown in Fig. 3.6(b), where the color map is also provided.

In the model of Eq. (2.117), the requirement (B) becomes $\sigma_x \gtrsim 1/(2k_0\sigma_{r,x'})$, $\sigma_y \gtrsim 1/(2k_0\sigma_{r,y'})$. Notably, one can intentionally make M insensitive to σ_x (or σ_y), and, thus, enable an independent measurement of σ_y (or σ_x). For example, by using a vertical slit [Fig. 3.14(a)], which can be approximated by a very small $\sigma_{r,x'} \ll 1/(2k_0\sigma_x)$, one can deduce σ_y from a measured M without the knowledge of σ_x. The same applies to a hor-

izontal slit [Fig. 3.14(b)]. Other more unusual radiation masks [for example, Fig. 3.14(c)] can also be applied to analyze fluctuations in various portions of the angular distribution of the radiation, which adds flexibility to this method. Assuming no angular restrictions, $\sigma_{r,x'}, \sigma_{r,y'} \approx \sqrt{\lambda_0/(2L_\mathrm{u})}$ [2, Eq. (2.57)], and the requirement (B) becomes

$$\sigma_x, \sigma_y \gtrsim \sqrt{2L_\mathrm{u}\lambda_0}/(4\pi), \tag{3.24}$$

where $\lambda_0 = 2\pi/k_0$, L_u is the undulator length. In IOTA, this corresponds to $\sigma_x, \sigma_y \gtrsim 50\,\mu\mathrm{m}$, or $\epsilon_x \gtrsim 1.0\,\mathrm{nm}$, $\epsilon_y \gtrsim 2.2\,\mathrm{nm}$; and $\langle \mathcal{N} \rangle / M \in [2.3, 5.0]$ (as per measurements).

Equation (3.24) shows that the resolution limit improves with a shorter wavelength. Therefore, this technique may be particularly beneficial for existing state-of-the-art and next generation low-emittance high-brightness ultraviolet and x-ray synchrotron light sources. Consider the Advanced Photon Source Upgrade (APS-U) with a round beam configuration for example. The beam energy is $6\,\mathrm{GeV}$, $n_e = 9.6 \times 10^{10}$, $\sigma_z = 3.1\,\mathrm{cm}$, $\epsilon_x = 31.9\,\mathrm{pm}$, $\epsilon_y = 31.7\,\mathrm{pm}$, $\sigma_x = 12.9\,\mu\mathrm{m}$, $\sigma_y = 8.7\,\mu\mathrm{m}$, $\sigma_{x'} = 2.5\,\mu\mathrm{rad}$, $\sigma_{y'} = 3.6\,\mu\mathrm{rad}$ [105]. Let us use the fundamental harmonic $\lambda_1 = 4.1\,\text{Å}$ of the undulator with $\lambda_\mathrm{u} = 28\,\mathrm{mm}$, $K_\mathrm{u} = 2.459$, and $L_\mathrm{u} = 2.1\,\mathrm{m}$. Equation (3.23) yields $\langle \mathcal{N} \rangle / M = 19$, and Eq. (3.24) becomes $\sigma_x, \sigma_y \gtrsim 3.3\,\mu\mathrm{m}$. Thus, both requirements (A) and (B) are satisfied. These order-of-magnitude estimates were confirmed by more detailed numerical calculations using Eq. (2.105) and our computer code [69, 77].

It may be possible to use our fluctuations measurement apparatus, or an improved variation of it, as a tool for the diagnostics of the Optical Stochastic Cooling (OSC) experiment in IOTA [34–36]. In this experiment, the beam emittances and the bunch length are significantly smaller than in the round and flat beam configurations, considered in this dissertation. Even in the regime when transverse emittances and bunch lengths cannot be measured individually, the fluctuations may serve as an indicator of the cooling process. When the cooling process starts, the electron bunch shrinks, which, in turn, makes the fluctuations of the

number of detected photons increase.

3.6 Conclusions

To conclude, power fluctuations in undulator radiation were measured in IOTA under two different experimental conditions and compared with our theoretical predictions.

In the round-beam configuration, all parameters entering Eq. (2.105) were known. The predicted fluctuations of the number of detected photons $\mathrm{var}(\mathcal{N})$ agree well with the measurements. If Eq. (2.82) was used, which does not account for the electron beam divergence, such a good agreement would not be observed. The angular electron beam divergence can be neglected when it is significantly smaller than the rms radiation divergence. For the fundamental of undulator radiation it can be estimated as $\sqrt{\lambda_1/(2L_\mathrm{u})}$ [2, Eq. (2.57)].

The vertical emittance of the flat beam in IOTA was unresolvable by existing synchrotron light monitors, therefore a prediction for the fluctuations $\mathrm{var}(\mathcal{N})$ using Eq. (2.105) could not be made. However, it was possible to perform the reverse of this procedure and infer the unknown small vertical emittance from the measured fluctuations. The obtained value of ϵ_y agrees with our independent estimate employing a model for the beam lifetime assuming Touschek scattering as the dominant particle loss mechanism.

It was shown that this non-invasive fluctuations-based technique may be particularly beneficial for existing state-of-the-art and next generation low-emittance high-brightness ultraviolet and x-ray synchrotron light sources. Advanced Photon Source Upgrade at Argonne was considered as an example. This technique can be enhanced to determine more than one electron bunch parameter at a time by using various radiation masks, for example, horizontal and vertical slits.

It would be beneficial to repeat these fluctuation measurements with a longer and brighter undulator. In this experiment, it was necessary to avoid using a monochromator or restricting the angular aperture, because all available radiation had to be collected to achieve a

signal with a voltage amplitude that could be easily measured. Therefore, the integrals in Eqs. (2.105) and (2.108) had to be calculated over a broad range of angles and wavelengths. With a monochromator, a slit or a pinhole detector, these integrals could be significantly simplified. Further, if our undulator had more periods and if we were able to use a monochromator, it would be possible to slowly vary the beam energy and find the energy at which the detected power is at maximum, i.e., when we are centered on the peak of the fundamental harmonic. In this case, the systematic error of the ϵ_y measurement via the fluctuations, related to the uncertainty on the beam energy, would be negligible. With a brighter undulator, it would be possible to use a narrow vertical slit in front of the detector, then the magnitude of the fluctuations would only depend on ϵ_y and the systematic error of the ϵ_y measurement related to the uncertainty of ϵ_x, measured by the SLMs, would be minimized, too. Finally, for a brighter undulator, the statistical error on the measured value of the fluctuations would be lower as well.

In this chapter, the photon shot noise contribution [the first term in Eq. (2.69)] to the fluctuations was not studied in detail. Our theoretical derivations in Chapter 2 and most of the literature [47–49] suggest that this contribution is equal to $\langle \mathcal{N} \rangle$. This was used as a fact without confirming it empirically — it was not possible to reduce the incoherence contribution [the second term in Eq. (2.69)] enough to make the photon shot noise contribution dominant. This will be achieved in the next chapter.

CHAPTER 4

MEASUREMENTS WITH A SINGLE ELECTRON IN THE IOTA RING

4.1 Introduction

It was a natural next step in our research to get rid of the collective term (the second term) in the expression for the turn-to-turn variance of the number of detected photons $\mathcal{N}$,

$$\mathrm{var}(\mathcal{N}) = \langle \mathcal{N} \rangle + \frac{1}{M} \langle \mathcal{N} \rangle^2 , \tag{4.1}$$

by considering a single electron circulating in the ring. Indeed, according to Eqs. (2.57), (2.70), (2.82), and (2.105), $1/M \propto (n_e - 1)$. Therefore, when $n_e = 1$, the second contribution vanishes. This allows us to study the quantum contribution (the first contribution) in detail. It can be tested whether the Poissonian photostatistics is observed, which is represented by the relation

$$\mathrm{var}(\mathcal{N}) = \langle \mathcal{N} \rangle . \tag{4.2}$$

There may be some deviations towards super-Poissonian light ($\mathrm{var}(\mathcal{N}) > \langle \mathcal{N} \rangle$) or sub-Poissonian light ($\mathrm{var}(\mathcal{N}) < \langle \mathcal{N} \rangle$). Poissonian light is very common, examples include laser radiation, radioactive decay, and, in fact, any strongly attenuated super- or sub-Poissonian light. Super-Poissonian light is also common. For example, thermal light, or any light with classical fluctuations of the radiated power. In fact, the undulator radiation generated by an electron bunch in Chapter 3 was super-Poissonian. Sub-Poissonian photostatistics, however, is unusual and it would indicate some interesting non-classical state of the radiated field. An example could be the Fock state (number state) with a certain number of quanta in it. Another example is the non-classical states observed in the parametric down conversion [106].

In consideration of the synchrotron radiation, the crucial parameter is the electron recoil,

$$\chi = \frac{E_{\text{photon}}}{E_{\text{electron}}}, \tag{4.3}$$

i.e., the ratio of the photon energy and the electron energy. To properly describe the photostatistics of the synchrotron radiation, it should be considered in the framework of quantum electrodynamics (QED) [107–109], where both the electron and the radiation are quantum objects. The deviations from the Poissonian photostatistics are closely related to the correlation (or anticorrelation) in the detected photon pairs. The quantum two-photon effects in the bending-magnet radiation have been considered perturbatively in [110]. To our knowledge, the quantum two-photon effects have not been considered in an undulator. However, a lot of progress has been made in the QED description of the two-photon Compton process in the intense laser field [111–114]. In terms of theoretical description, the undulator radiation generated by ultra-relativistic electrons is equivalent to the Compton process in the intense laser field. Indeed, due to Weizsäcker-Williams [115–117] approximation, in the electron's rest frame, the magnetic field of the undulator can be approximated as a plane electromagnetic wave. There exists an exact solution of the Dirac equation [107] for an electron in the field of a plane electromagnetic wave — Volkov states [118]. This allows to obtain an expression for the differential emission probability of the two-photon process non-perturbatively using the Dirac-Volkov propagator in the Furry picture [112]. In this description, not only the emitted radiation, but also the electron is considered as a quantum object, including its spin properties. This consideration shows that the effects of two-photon correlation and the deviations from the Poisson photostatistics are proportional to the electron recoil parameter Eq. (4.3). Typically, in accelerators this parameter is very small. It may be possible to observe some correlation effects discussed in [111] in FACET-II [119] with an optical undulator. However, in most other linear and circular accelerators these effects are undetectable. In IOTA, $\chi \approx 10^{-8}$ and the electron (or electrons) circulating in IOTA can be approximated

as a classical current. In this case, it is not necessary to use the Dirac equation and a simpler model, presented by Glauber in Refs. [47–49], can be used. The Glauber's model predicts that the radiated field is in a coherent state (Glauber state), which results in the Poissonian photostatistics and no correlation between the detected synchrotron radiation photons (undulator or bending magnet).

However, there has been at least one experiment with the synchrotron radiation [43, 44] two decades ago claiming to observe a non-classical sub-Poissonian photon statistics in the seventh coherent spontaneous harmonic of an FEL. This could have been an instrumentation effect [45]. The measured photostatistics could be affected by the low quantum efficiency ($\lessapprox$ 10 %) and the relatively long dead time of the detector (a photomultiplier tube) used in [43, 44]. Nonetheless, it is interesting to carry out a fairly similar photostatistics measurement in IOTA with more advanced equipment available today and see the results. Although we do not anticipate any deviations from the Glauber's model, they cannot be eliminated completely.

A single electron circulating in a ring is a well-controlled and repeatable system. It may be very useful for testing theoretical predictions for the synchrotron radiation. In this chapter, the photon flux and the statistical properties of the photon detection events will be considered. Measurements with a single detector and with two detectors, separated by a beamsplitter, will be presented. In addition, the recorded detection times will be used to study the synchrotron motion of a single electron in IOTA. Similar previous experiments with a countable number of electrons in the VEPP-3 storage ring in Novosibirsk have been reported in [120–122]. A single electron has also been observed in the Metrology Light Source in Germany [123, 124] and in the first electron-positron collider AdA [125, 126].

4.2 Apparatus

This experiment with a single electron is carried out with the same undulator and in the same dark box as in Chapter 3, see Fig. 3.1 . However, the light detector and the data acquisition system are different in this experiment. Namely, a Single Photon Avalanche Diode (SPAD) detector is used, see Table 4.1 and [127], which is mostly sensitive to the second harmonic of the undulator radiation. The pulses from the SPAD detector went to a picosecond event timer [128], which was also provided with the IOTA revolution marker, see Fig. 4.1 . This allowed us to create a table containing the IOTA revolution number and the detection time relative to the IOTA revolution marker for each detection event. The dead time of the SPAD detector (22 ns) was lower than one IOTA revolution (133.3 ns) and, combined with a very low dark count rate, it virtually had no effect on the photostatistics. On the way to the picosecond event timer, the pulses from the SPAD detector also went through a passive signal inverter (hybrid) and through a discriminator, these elements are not shown in Fig. 4.1 .

Table 4.1: Specifications of the SPAD detector [127].

Parameter	Value
Active area (diameter)	180 µm
Detector efficiency at 650 nm	65 %
Dark count rate	$\approx$ 100 Hz
Dead time	22 ns
Pulse height	2 V
Pulse duration	10 ns
Intrinsic arrival time jitter	0.35 ns

The table shown in Fig. 4.1 is obtained after post-processing of the collected data. The raw data include absolute arrival times of the IOTA revolution marker pulses and the SPAD detector pulses. Using the raw data it was possible to calculate the jitter of the IOTA revolution marker. It was about 14 ps (rms). Below, it will be shown that it is negligible compared to the intrinsic timing jitter of the SPAD detector and compared to the synchrotron

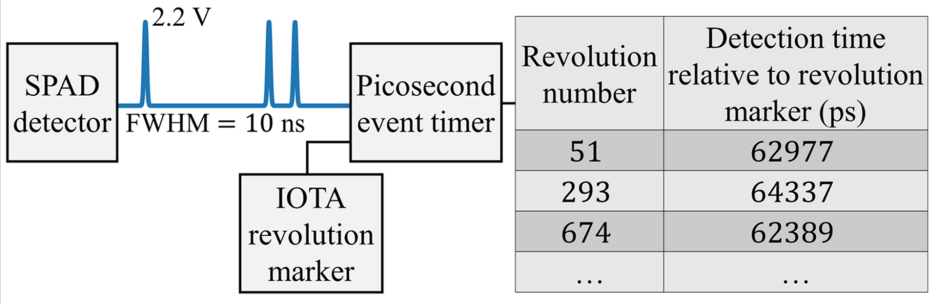

Figure 4.1: Block diagram of the data acquisition system.

motion of the electron in IOTA.

A focusing lens with a focal distance of 180 mm was used (different from the one used in Chapter 3). The SPAD detector was installed on a stage with two picomotors (transverse motion, x- and y-axes) and a stepper motor (longitudinal motion, z-axis), similar to the experiment in Chapter 3. A special website was created for this experiment, where all the controls could be found, a screenshot is shown in Fig. 4.2 . It was created using a Node-RED server [129] running on a Raspberry Pi 3b+ computer. This website was accessible on the Fermilab's secure internal network, called "Controls network", without access to the internet. The optimal location of the detector could be found by moving the detector along x, y, and z iteratively, finding the extremum each time.

4.3 Obtaining a single electron in the ring

Obtaining a single electron in the IOTA ring is a standard and a well-established procedure. The number of electrons in the ring can be determined by looking at the bending-magnet radiation photocount rate on the photomultiplier tubes (PMTs) installed at some dipole magnets in IOTA. In addition, there are high-resolution digital cameras in IOTA looking at the bending-magnet radiation (SLMs, see Fig. 3.3). They are capable of resolving individual electrons in the ring as well, when the exposure time is sufficiently long, e.g., one second. Finally, given optimal alignment, the photocount rate on the SPAD detector is perhaps the

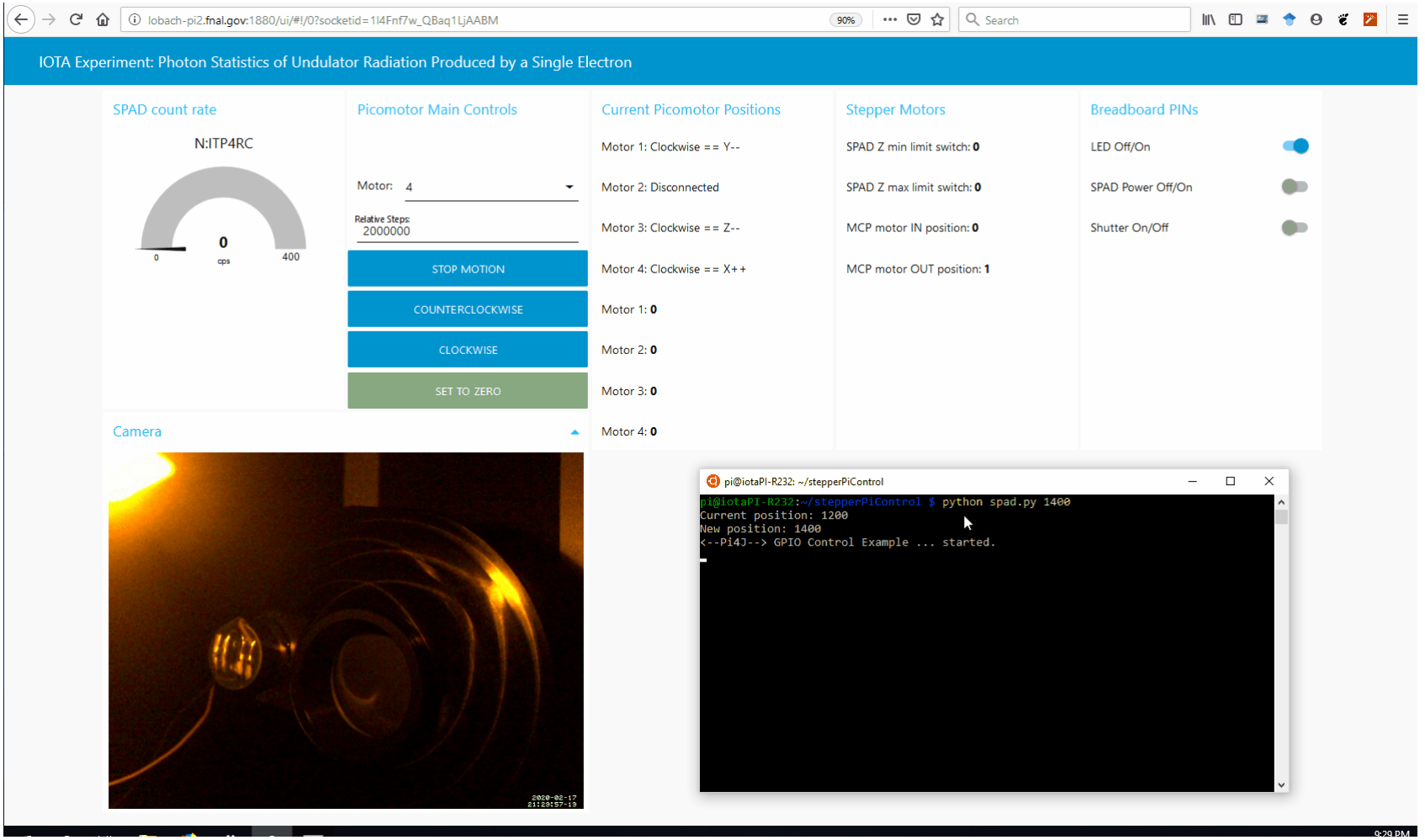

Figure 4.2: A screenshot of the website with most of the controls for the single-electron experiments. Namely, x, y, z motors, photocount rate meter, optical shutter, detector power switch, LED power switch, and live camera.

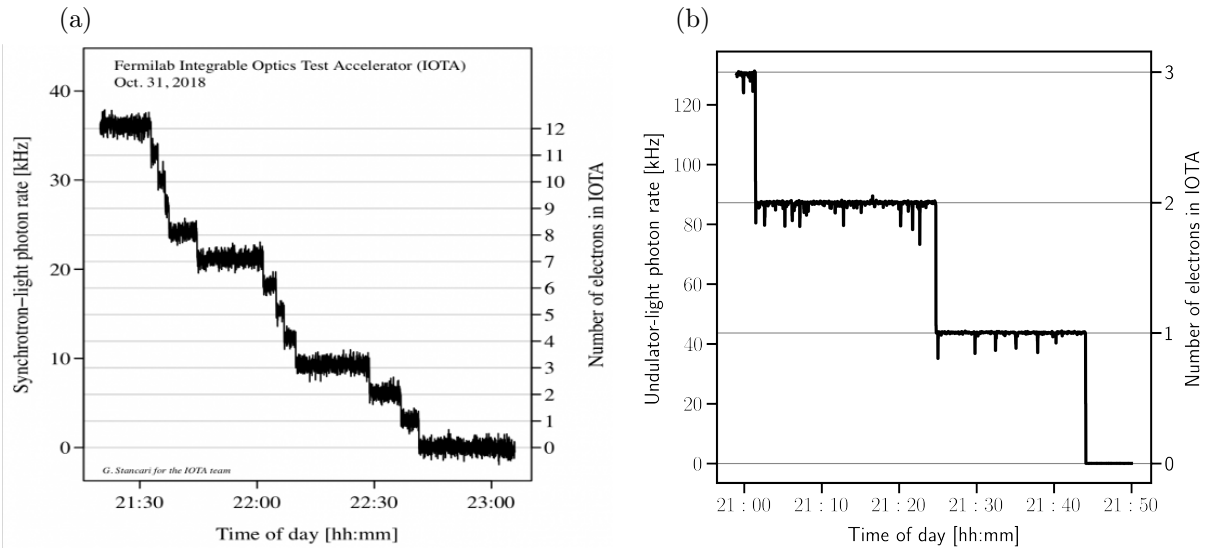

Figure 4.3: (a) Count rate on a photomultiplier tube, detecting the bending-magnet radiation, generated by the last 12 electrons in the ring. Adapted from [130]. (b) Count rate on the SPAD detector, detecting the undulator radiation, generated by the last 3 electrons in the ring (in this measurement the edge-pass filters were removed and the count rate was $\approx 45\,\mathrm{kHz}$, as opposed to $24.7\,\mathrm{kHz}$ with the edge-pass filters).

most accurate measurement of the number of electrons in the ring in the regime of a countable number of electrons. Due to using the undulator radiation and due to the high detection efficiency, the count rate on the SPAD is higher than on the PMTs. The signal-to-noise ratio of the SPAD detector is also superior to that of the PMTs and the digital cameras, compare Figs. 4.3(a) and (b), for example. However, because of the very small active area of the SPAD detector, the events of strong scattering of the electrons in the residual gas may change the photocount rate on the SPAD. This is the origin of the spikes in the photocount rate in Fig. 4.3(b). The PMTs at IOTA do not have this problem.

There are several ways to obtain a single electron in IOTA: (1) if the beam lifetime is relatively short, it is possible to simply wait for the beam current to decay down to a single electron. This is how a single electron was obtained in IOTA for the first time, see Fig. 4.3(a), just one month after the first beam circulation in IOTA; (2) the process of beam current decay can be accelerated dramatically by scraping the electron beam by quickly lowering the

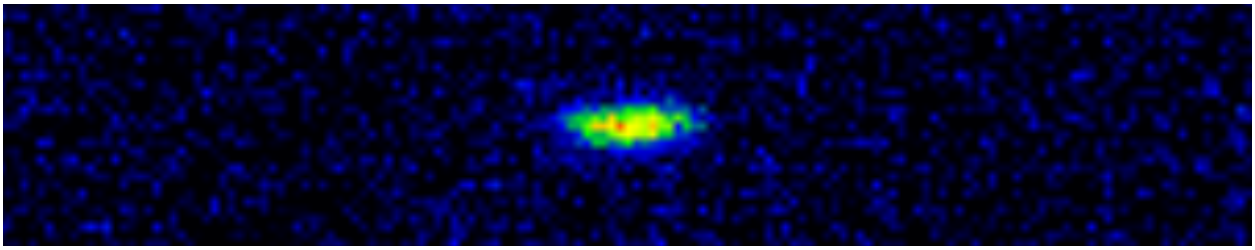

Figure 4.4: Digital camera image created by the bending-magnet radiation, generated by a single electron circulating in IOTA. Adapted from Ref. [131].

rf cavity voltage and then restoring it to the nominal value; (3) It is possible to inject a single electron (or a few electrons) into IOTA in the first place, see Ref. [132]. First, the laser of the FAST linac photo-injector is turned off and only the dark current is produced. Then, several optical transition radiation (OTR) foils are inserted along the linear accelerator to further reduce beam intensity. Finally, the strength of the last quadrupole in the linear accelerator before the injection to IOTA could be varied to fine-tune the number of injected electrons. The average number of injected electrons could be tuned to be approximately equal to one. Figure 4.5 shows the measured distribution of the number of injected electrons in a series of 53 injections. These measurements were reported in Ref. [132]. The measured probability to inject a single electron is 32 %. In this configuration, one can reinject several times until a single electron is observed in the ring. It is a very quick procedure. When everything is tuned optimally, a single electron can be injected in less than one minute, on average.

4.4 Measured and predicted radiation properties

It is important to understand that our SPAD detector is binary — it does not feel the difference between detections of 1,2,3, and so on photons at a time, it always produces the same pulse (TTL, 10-ns-long). Therefore, the data collected with the SPAD detector and the picosecond event timer can be represented as a sequence of 0's and 1's only, where every 0 represents an IOTA revolution without a detection event, and every 1 represents an IOTA

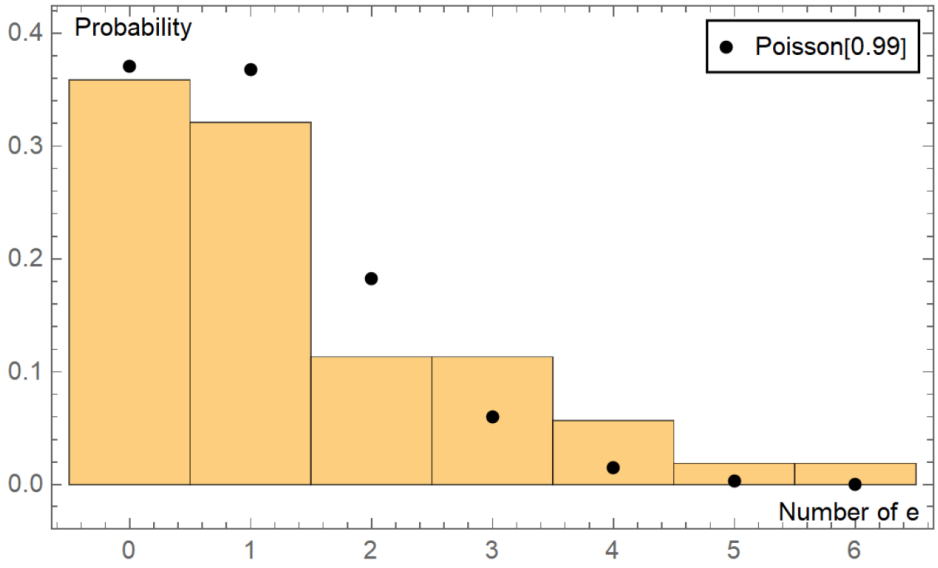

Figure 4.5: Distribution of the number of electrons injected into IOTA (yellow histogram) and a fit by the Poisson distribution (black points). Adapted from Ref. [132].

revolution with a detection event. These data can be used to evaluate the probability of a photon detection per pass in the undulator as the ratio of the total number of detections and the number of IOTA revolutions in the data set. This probability will be denoted by p. This probability p is different from the classically predicted expectation value p_0 of the Poisson distribution for the number of detected photons [47–49] (in the notation of Chapters 2 and 3, $p_0 = \langle \mathcal{N}_{\text{s.e.}} \rangle$). There exists a simple relation between these two probabilities,

$$p = \sum_{k=1}^{\infty} \frac{p_0^k}{k!} e^{-p_0} = 1 - e^{-p_0}, \tag{4.4}$$

i.e., p is the probability to detect 1 or more photons, because our binary detector does not resolve the exact number of detected photons. Several data sets were collected with up to 60 seconds recorded at a time. The measured value of p varied among these data sets within about 2 % because the detector was moved and realigned between some measurements. Therefore, let us consider only one 60-second-long uninterrupted data set for now. In this data set, $p = (3.29 \pm 0.02) \times 10^{-3}$, where the uncertainty was estimated as the standard

deviation of the values of p calculated in ten 6-second-long sub-samples of the entire 60-second-long data set. This probability value corresponds to about one detection event per 304 revolutions in IOTA (on average), or to a count rate of 24.7 kHz. For comparison, the dark count rate of the SPAD detector was only 108 Hz. In addition, a 5-ns-long gate was used around the expected detection arrival time, which allowed us to reduce the effective dark count rate to 4.0 Hz.

Also, a theoretical prediction was made for the probability p. We used Eqs. (2.89), (2.90), and (2.108) to calculate p_0, which is equivalent to $\langle \mathcal{N}_{\text{s.e.}} \rangle$. The integral in Eq. (2.108) was computed using our code repository [77] and the expressions in Eqs. (2.89) and (2.90) were evaluated using our WIGRAD package [69] (which agrees with the SRW package [70]). The manufacturers' specifications were used for the spectral properties of the vacuum chamber window at the M4R dipole magnet, the two mirrors, the focusing lens, the two edge-pass filters, and the detection efficiency of the SPAD detector. The following edge-pass filters were used: a 500-nm longpass filter and a 800-nm shortpass filter. The result of the calculation was $p_{\text{sim}} = 6.07 \times 10^{-3}$. However, this estimate assumed that the lens focused the radiation into a spot smaller than the sensitive area of the SPAD detector — $\varnothing 180\,\mu\text{m}$. Perhaps this assumption was wrong due to the aberrations in the lens and the diffraction limit, and because of that about a half of the photons were lost.

Figure 4.6 offers more details on our calculation of the spectral-angular properties of the undulator radiation in IOTA. Because of the two round mirrors, which are at 45° to the direction of propagation of the radiation, the angular aperture takes an elliptical shape with the vertical axis smaller than the horizontal by a factor of $\sqrt{2}$. This aperture was used in both panels (a) and (b) of Fig. 4.6.

Since the second harmonic of the undulator radiation is considered in this experiment, the angular distribution of the number of detected photons is represented by two peaks. The photograph embedded in Fig. 4.6(a) and our measurement with the SPAD detector

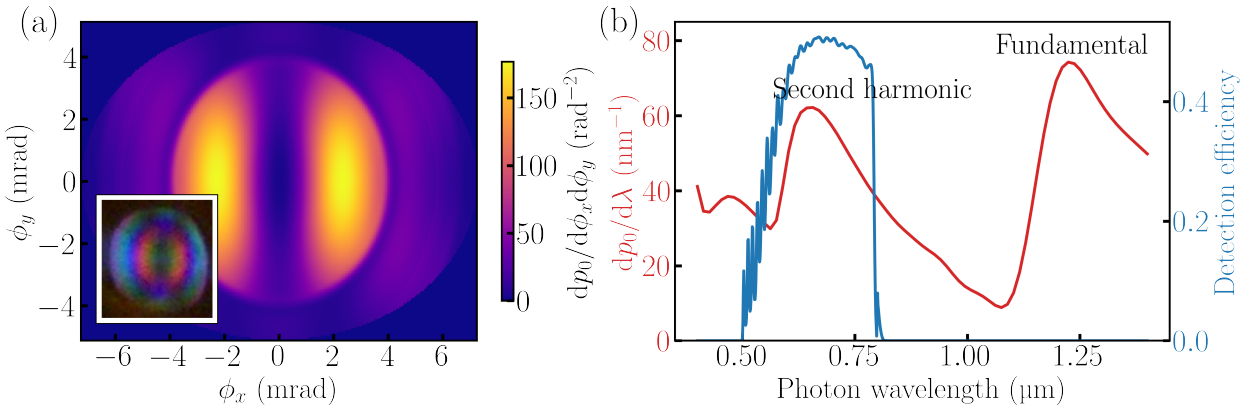

Figure 4.6: (a) Calculated angular distribution of the number of detected photons accounting for the detection efficiency of our system. Also, a photograph of the undulator light spot on a black screen (bottom left). (b) Calculated spectral distribution of the number of photons, emitted into the angular aperture (red line, left-hand vertical scale) and the detection efficiency of our system (blue line, right-hand vertical scale). Both (a) and (b) are calculated for an elliptical aperture with the horizontal and the vertical semi-axes 7.3 mrad and 5.1 mrad, respectively.

in Fig. 4.7 agree rather well with the simulation shown in Fig. 4.6(a). The measurement with the SPAD detector in Fig. 4.7 was obtained by recording the photocount rate on the SPAD detector, while moving it with the x-axis picomotor at seven different y-positions. The values along x- and y-axes in Fig. 4.7 were obtained assuming that the piezo actuators were moving with a constant speed indicated in the manufacturer's specifications. It should be understood that these values are very approximate, since it is not guaranteed that the motion was uniform. In addition, the speed of motion could significantly depend on the load. These measurements were carried out far from the optimal z-position, because the goal was to see the angular distribution of the number of detected photons. In the optimal z-position, one would only see a single very narrow peak, defined by the convolution of the focused light spot and the sensitive area of the SPAD detector.

Let us consider the statistical properties of the collected data. Assuming no correlation between IOTA revolutions, there are only two possible outcomes at each revolution: (1) a detection event with probability p and (2) no detection with probability $1 - p$. It is a

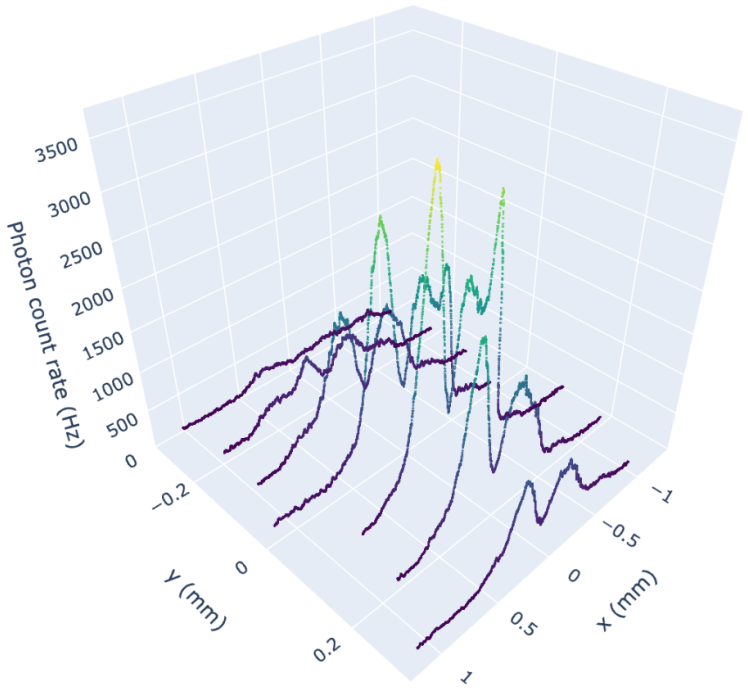

Figure 4.7: Seven measured x-scans of the photocount rate at seven different y-positions of the SPAD detector. This measurement was carried out far from the focal plane of the lens (far from the optimal z-position).

sequence of Bernoulli trials, for which the mean equals p and the variance equals $p(1-p)$. Interestingly, in this case, the statistics is slightly sub-Poissonian, $\mathrm{var}(\mathcal{N}) = (1-p)\langle\mathcal{N}\rangle$. However, it is because of the principle of operation of the SPAD detector, not because of the intrinsic properties of the radiation.

In general, photostatistics can be characterized by the Fano factor [45], which is defined as

$$F = \frac{\mathrm{var}(\mathcal{N})}{\langle\mathcal{N}\rangle}. \tag{4.5}$$

Then, sub-Poissonian, Poissonian, and super-Poissonian photostatistics correspond to $F < 1$, $F = 1$, and $F > 1$, respectively. For a sequence of Bernoulli trials, $F = 1-p$. Let us consider one 60-second-long data set again. One can divide it into 1000 sub-samples and calculate the value of the Fano factor in each of the sub-samples. Then, it is possible to plot a histogram for the 1000 obtained values. It is presented in Fig. 4.8.

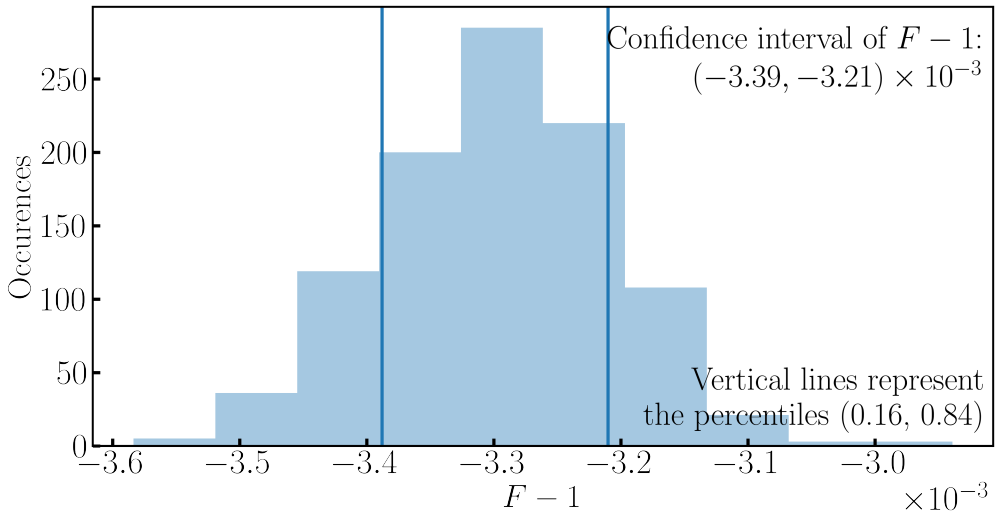

Figure 4.8: A histogram for 1000 values of the deviations of the Fano factor from unity in 1000 sub-samples of a 60-second-long data set of the SPAD's detection events.

All 1000 obtained values of F are smaller than unity. The vertical lines in Fig. 4.8 represent the 0.16 and 0.84 percentiles (in a normal distribution they correspond to a minus one sigma and a plus one sigma). The corresponding confidence interval for $F-1$ is $(-3.39, -3.21) \times 10^{-3}$. This is in agreement with the expectation for a sequence of Bernoulli trials $F - 1 = -p$ within the statistical error, since the measured average detection probability was $p = 3.29 \times 10^{-3}$.

Further, some measurements were taken with several different optical neutral density filters to verify the following relation between the measured Fano factor F_{measured} and the intrinsic Fano factor of the radiation F_{source} [44, 45]

$$F_{\text{measured}} - 1 = \eta(F_{\text{source}} - 1), \tag{4.6}$$

where η is the detection efficiency of the system. A filter wheel was used with seven different neutral density filters and one open hole. Several data sets were recorded with each filter. The results of these measurements are shown in Fig. 4.9.

No statistically significant deviations from the expected linear relation Eq. (4.6) were

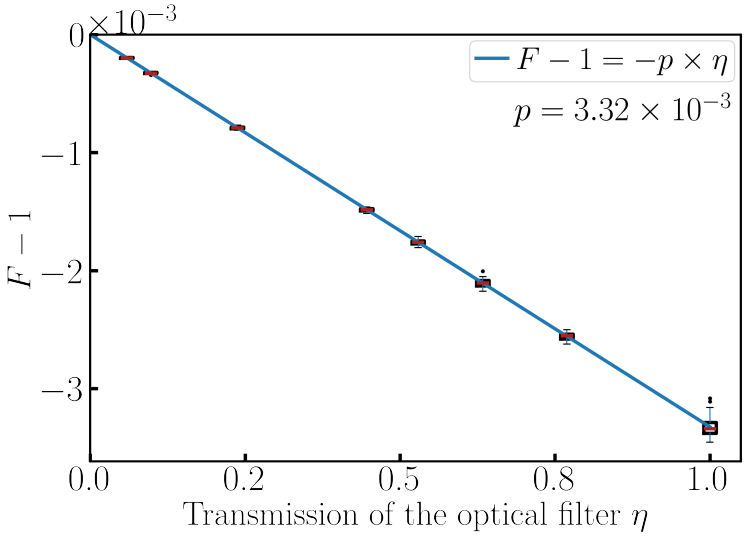

Figure 4.9: Fano factor measurements with seven different neutral density filters and one measurement without any neutral density filter.

observed in Fig. 4.9. Equation (4.6) illustrates that if the detection efficiency is very low, then any intrinsic photostatistics will look like Poissonian when measured. This is why in our measurements the SPAD detector was used, whose quantum efficiency reaches 65 % at 650 nm, which is much higher than in [43, 44] ($\lessapprox 10\,\%$).

In a sequence of Bernoulli trials, the times between consecutive photocounts (in units of IOTA revolutions) should follow a geometric distribution, and the number of photocounts in a certain fixed time window (for example, $n = 1000$ IOTA revolutions) should follow a binomial distribution. Figure 4.10 illustrates that both of these expectations are fulfilled.

In both cases, the χ^2 goodness-of-fit test [133, p. 637] results in a P-value (see [133, p. 140], do not confuse with the probability of detection p) above the conventional 0.05 threshold. Namely, 0.36 for the distribution of the interarrival times and 0.20 for the distribution of the number of counts in a time window. This means that the null hypothesis (exponential or binomial distribution, respectively) cannot be rejected, i.e., there are no statistically significant deviations from the expectations for a sequence of Bernoulli trials. Let us reiterate, however, that the distribution of the number of photons detected per one pass was not studied

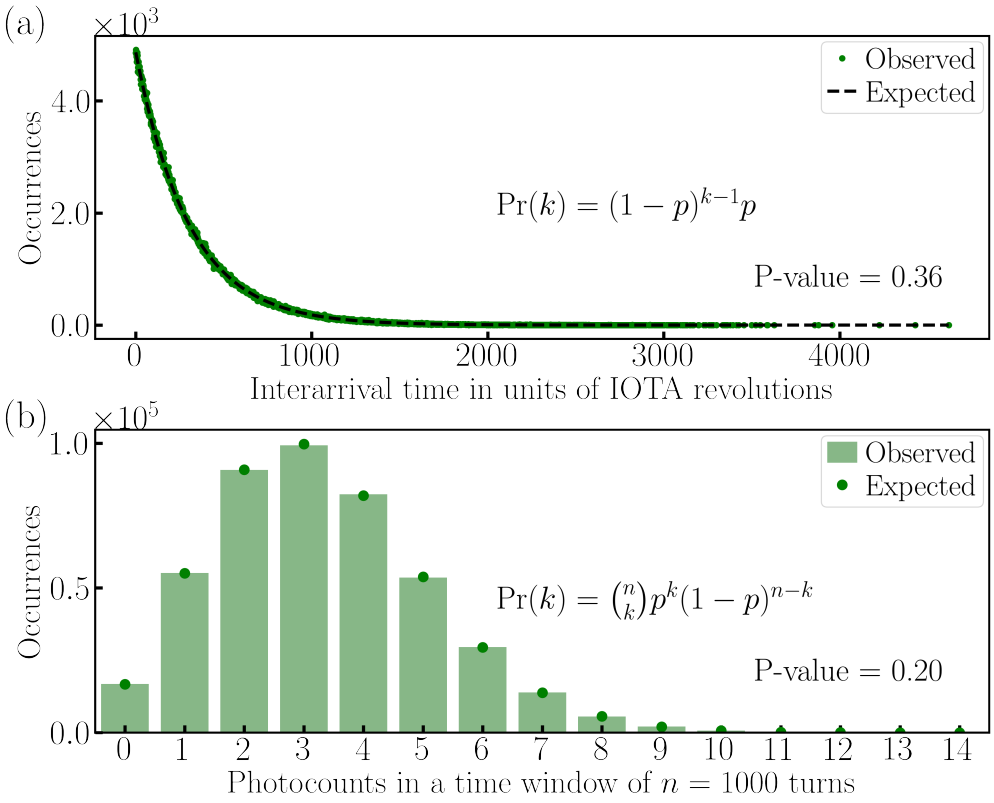

Figure 4.10: (a) The measured distribution of interarrival times between the photocounts and a fit by a geometric distribution. (b) The measured distribution of the number of photocounts in a time window equal to $n = 1000$ IOTA revolutions and a fit by a binomial distribution.

— our detector cannot resolve this number, it can only say if there was or was not a detection event after a pass in the undulator.

4.5 Synchrotron motion of a single electron

Since our apparatus recorded the arrival time relative to the IOTA revolution marker for each detection event, it could be plotted as a function of the IOTA revolution number, see Fig. 4.11 . In this figure one can observe a sinusoidal curve — it is, in fact, the synchrotron motion of a single electron in IOTA.

It was decided to use this as an opportunity to compare the measured synchrotron motion with a simulation. In Fig. 4.11, the time scale is on the order of a few milliseconds, on a

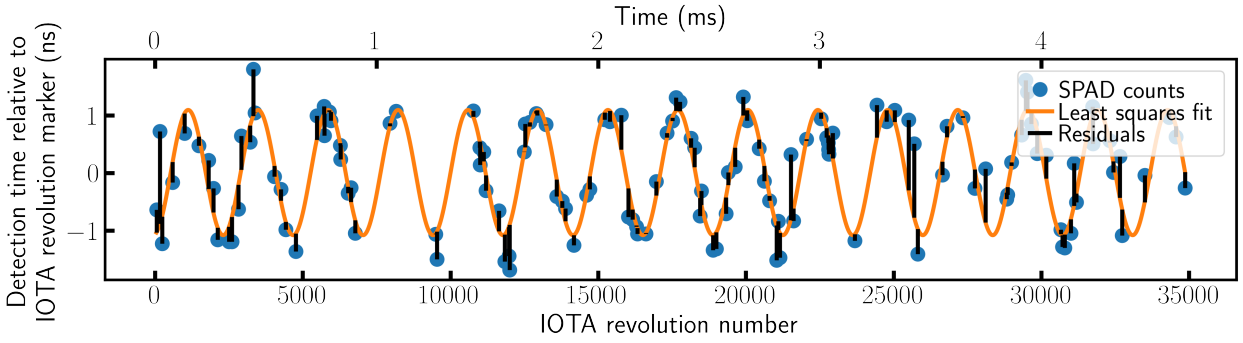

Figure 4.11: The measured detection time relative to the IOTA revolution marker as a function of the IOTA revolution number and a fit by a sinusoidal curve. A single electron was stored in the ring during this measurement. The deviations of the collected data points from the sinusoidal fit are due to the intrinsic timing jitter of the detection system.

larger time scale (seconds) the amplitude of the synchrotron motion will change significantly in a random fashion due to quantum excitation and radiation damping, our simulation will account for these effects too.

4.5.1 Turn-by-turn map equation

Our simulation [134] used the following transformation of the relative energy deviation δ_i and the rf phase ϕ_i of a single electron from turn i to turn $i+1$,

$$\delta_{i+1} = \delta_i + \frac{eV_0}{E_0}\sin\phi_i - \frac{\langle U\rangle\,\mathcal{J}_E}{E_0}\delta_i - \frac{U_i}{E_0}, \tag{4.7}$$

$$\phi_{i+1} = \phi_i - 2\pi q\eta_s\delta_{i+1} + \xi_i, \tag{4.8}$$

where e is the electron charge, $E_0 = \gamma m_e c^2$ is the average energy of the electron, m_e is the electron mass, c is the speed of light, V_0 is the rf voltage amplitude, q is the rf harmonic number, $\eta_s = \alpha_c - 1/\gamma^2$ is the phase slip factor (the variation of η due to the variation of γ is negligible in IOTA), α_c is the momentum compaction factor, $\mathcal{J}_E$ is the longitudinal damping

partition number [135, p. 445], U_i is the radiation energy loss at ith turn, ξ_i is the rf cavity phase jitter at the ith turn. It was decided to model ξ_i as a Gaussian random variable with a zero average and a certain standard deviation σ_ξ. We refer the reader to [135, Eq. (3.28)] for the symplectic part of the transformation. The derivation of the synchrotron radiation damping term, $-\frac{\langle U\rangle \mathcal{J}_E}{E_0}\delta_i$, is described in [135, pp. 438–445]. The quantum excitation term, $-\frac{U_i}{E_0}$, is considered in [136]. The energy kick from the rf cavity at the synchronous phase ϕ_s compensates for the average energy loss due to the synchrotron radiation, i.e.,

$$eV_0 \sin\phi_s = \langle U\rangle\,. \tag{4.9}$$

In IOTA, during the single-electron experiments, the values of the parameters were the following, $V_0 = 380\,\mathrm{V}$, $\gamma = 188.6$, $E_0 = 96.4\,\mathrm{MeV}$, $\phi_s = 0.0287\,\mathrm{rad}$, $\mathcal{J}_E = 2.64$, $q = 4$, $\alpha_c = 0.070\,86$, $\eta_s = 0.070\,83$.

Using the approximation of an isomagnetic ring, the average emitted energy per turn in IOTA is [135, pp. 434–435]

$$\langle U\rangle = \frac{8\pi\alpha\gamma}{9}u_c = 10.9\,\mathrm{eV}, \tag{4.10}$$

where $\alpha = 1/137$ is the fine-structure constant, u_c is the critical energy [136, Eq. (11)],

$$u_c = \frac{3}{2}\frac{\hbar c\gamma^3}{\rho} = 2.8\,\mathrm{eV}, \tag{4.11}$$

where $\rho = 70\,\mathrm{cm}$ is the radius of the electron trajectory in the dipole magnets in IOTA, $\hbar$ is the reduced Plank constant. The isomagnetic ring approximation is a very good approximation in IOTA, the radiation losses in the undulator are negligible compared to the radiation losses in the bending magnets.

Several other mechanisms of losses and fluctuations of the electron's energy have also been considered. However, they proved to be negligible. Namely, we considered the effect of fluctuations of the betatron amplitudes of the electron on the electron's synchrotron phase,

i.e., when the betatron amplitude is larger, the electron's trajectory is curved stronger and it takes longer to complete one revolution in the ring, at a fixed electron energy. Using for a conservative estimation $\epsilon_x = \epsilon_y = 20\,\text{nm}$ (the minimal observed emittance at small beam currents [98]), it can be concluded that this effect results in the rms synchrotron phase jitter contributions $2.6 \times 10^{-7}\,\text{rad}$ and $3.2 \times 10^{-7}\,\text{rad}$, from the horizontal and vertical betatron motions, respectively. It will be shown below that these contributions are negligible compared to the estimated rf cavity phase jitter.

Further, we estimated the energy losses by the electron due to the interaction with the residual gas in the vacuum chamber, namely, due to the collision (ionization) stopping power and due to the radiation (bremsstrahlung) stopping power. In these order-of-magnitude estimations, it was assumed that the residual gas is the atomic hydrogen with the effective pressure $4.2 \times 10^{-8}\,\text{torr}$ [98]. Then, as estimated by [137, Eq. (2.16)], the average collisional energy loss per turn is $3.6 \times 10^{-4}\,\text{eV}$. Per [75, p. 268], the average energy loss per turn due to the bremsstrahlung is $1.3 \times 10^{-5}\,\text{eV}$. When compared with the average energy loss per turn due to the synchrotron radiation ($10.9\,\text{eV}$) these effects are clearly negligible. It should be noted that bremsstrahlung could produce very rare events with energy loss comparable to the average synchrotron radiation energy loss per turn. It is possible to estimate how often such events occur using the formulas from Ref. [137]. Our estimates indicate that, on average, such extreme bremsstrahlung events would take place once per tens of hours. Therefore, most likely there was not even a single such event in all of the collected data.

4.5.2 Distribution of the turn-by-turn energy loss

The average number of bending-magnet radiation photons emitted per turn in an isomagnetic ring is [136]

$$\langle \mathcal{N} \rangle = \frac{5\pi\alpha}{\sqrt{3}}\gamma. \tag{4.12}$$

According to [47–49], in the case of a negligible electron recoil, which is the case in all storage rings, the number of emitted photons follows a Poisson distribution. In addition, in our own measurements in Section 4.4 no anomalies were observed in the photostatistics. Therefore, our simulation [134] will use a Poisson random number generator with the expectation value $\langle \mathcal{N} \rangle$ given by Eq. (4.12). In IOTA, $\langle \mathcal{N} \rangle = 12.5$.

The energies of these photons follow a distribution with the following density function [136, Eq. (18)],

$$n(x) = \frac{3}{5\pi} \int_x^\infty K_{5/3}(\xi)\, \mathrm{d}\xi\,, \tag{4.13}$$

where x is the normalized photon energy, i.e., the energy of an emitted photon u in units of the critical energy u_c,

$$x = \frac{u}{u_c}, \tag{4.14}$$

and $K_{5/3}(\xi)$ is a modified Bessel function of the third kind; $n(x)\,\mathrm{d}x$ gives the probability that the normalized energy of an emitted photon is between x and $x+\mathrm{d}x$. Reference [136] describes an implementation of a generator for the random variable x following the distribution from Eq. (4.13). This implementation will be used in our analysis. A histogram for the energies ($u = u_c x$) of one million emitted photons, obtained by using this generator, is shown in Fig. 4.12(a).

The following routine is used to simulate the total energy loss U_i at ith turn in IOTA. First, the number of emitted photons $\mathcal{N}_i$ is generated using a random Poisson variable generator with the expectation value $\langle \mathcal{N} \rangle = 12.5$. Then, the generator for the photon energies from [136] is used, which corresponds to the probability density from Eq. (4.13). This generator is used $\mathcal{N}_i$ times. Finally, to obtain U_i, the sum of the obtained $\mathcal{N}_i$ values of energy u_j is calculated,

$$U_i = \sum_{j=1}^{\mathcal{N}_i} u_j. \tag{4.15}$$

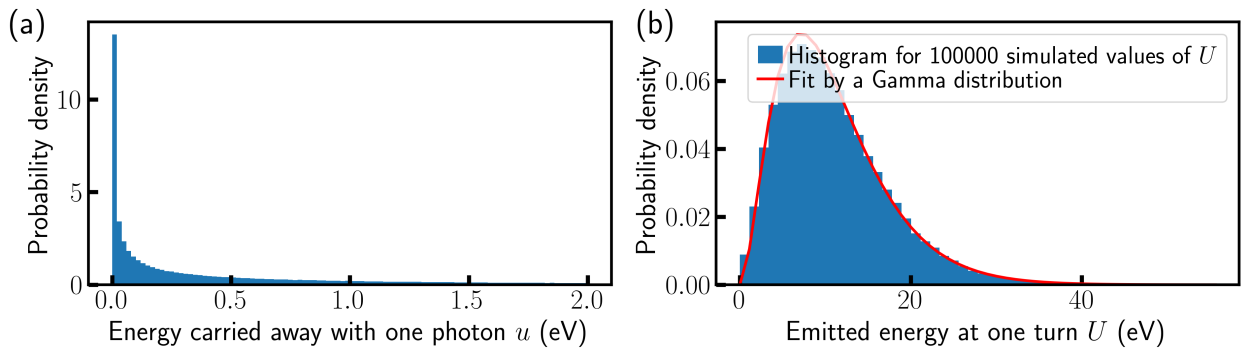

Figure 4.12: (a) A histogram for a million values of energy carried away by a bending-magnet radiation photon in IOTA, generated by the algorithm reported in [136]. (b) A histogram for 100 000 simulated values of energy loss per turn U using Eq. (4.15). Also, a fit by a Gamma distribution.

The result of such simulation of U_i for 100 000 IOTA revolutions is shown in Fig. 4.12(b) (blue histogram). However, this simulation is rather time-consuming, because the random generator for the photon energy has to be called on average $\langle \mathcal{N} \rangle = 12.5$ times per IOTA turn. Therefore, it was decided to approximate the distribution of U_i by a Gamma distribution, as suggested in [2, p. 121] and in [63]. It has the following probability density function [2, Eq. (4.75)]

$$p(U) = \frac{1}{\Gamma(M)} \frac{U^{M-1}}{\langle U \rangle^M} \exp\left(-M \frac{U}{\langle U \rangle}\right), \tag{4.16}$$

where $\Gamma(M)$ is the Gamma function and

$$M = \frac{\langle U \rangle^2}{\langle U^2 \rangle - \langle U \rangle^2}. \tag{4.17}$$

The value of M was obtained from the previously simulated U_i by Eq. (4.15) [blue histogram in Fig. 4.12(b)]. The result was $M = 2.92$. The density function of a Gamma distribution with this value of M is shown in Fig. 4.12(b) (red line). It agrees with the previously simulated histogram rather well. Therefore, henceforth, the Gamma distribution will be

used to simulate the turn-by-turn energy loss U_i. In this case, a random generator needs to be called only once per turn. It makes the simulation of the longitudinal motion of a single electron ≈ 25 times faster. Another justification for using this approximation is that the synchrotron motion period in IOTA during our measurements was about 0.313 ms, which corresponds to about 2351 IOTA revolutions. This means that one IOTA revolution is a very small part of one synchrotron motion period. Therefore, when simulating the quantum excitation term, one could choose time intervals longer than one IOTA revolution, i.e., m IOTA revolutions, with $m = 10, 20$, or 30 for example. This new energy loss, calculated (as a sum of m single-turn energy losses) and used in Eq. (4.7) once per m turns would have a distribution close to a normal distribution according to the central limit theorem, no matter what the single-turn distribution is (within reason). Although this approach could further speed up the simulation, it was decided not to pursue it, because the turn-by-turn simulation with a Gamma distribution had acceptable time performance — one second of synchrotron motion in IOTA could be simulated in about two seconds.

4.5.3 Comparison of simulations and measurements

Let us start by comparing the measurement and the simulation of the synchrotron motion amplitude as a function of time. The collected data points could be fitted by short pieces of sinusoidal curves with different amplitudes, see Fig. 4.13 . The length of each piece was about 20 synchrotron motion periods. The intervals were chosen to be slightly overlapping (by approximately 3 synchrotron motion periods). In this way, there is a possibility to construct a continuous fit for the entire data set by using a weighted average in the overlap region, with a weight of the left-hand sinusoidal curve going from 1 to 0 and the weight of the right-hand sinusoidal curve going from 0 to 1 linearly with time.

After performing this fitting procedure on the measured and on the simulated data, one could extract the sequences of amplitudes and plot them as functions of time, see Fig. 4.14,

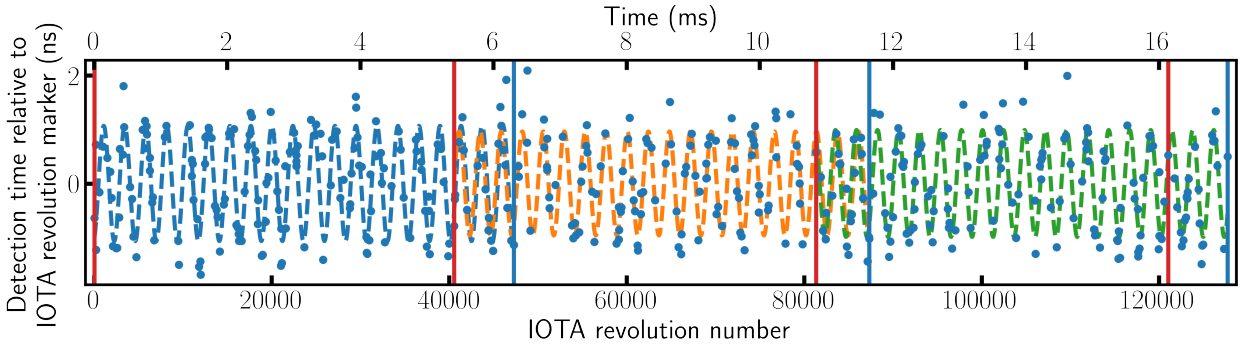

Figure 4.13: Illustration of the fitting procedure. The data points are fitted in short overlapping intervals.

where $\sigma_\xi = 6.0 \times 10^{-5}$ rad in the simulation.

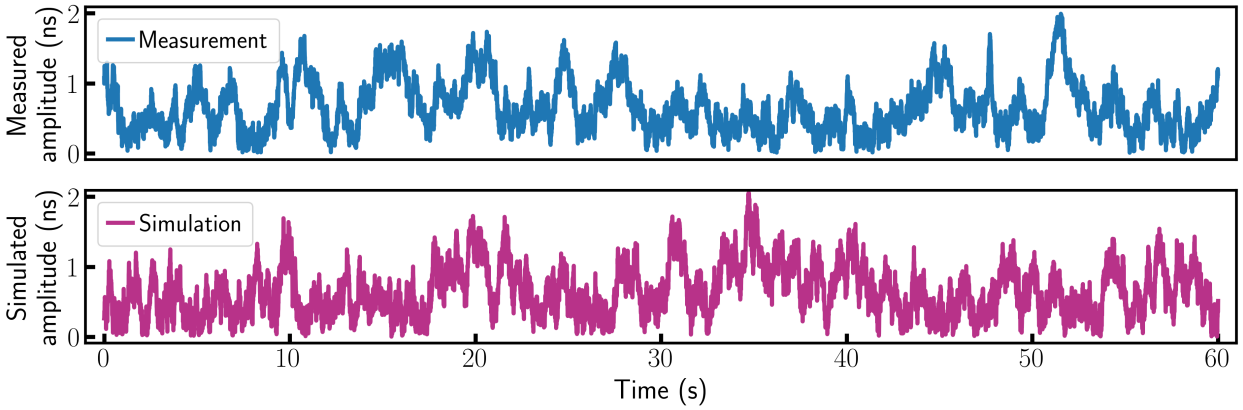

Figure 4.14: Amplitude of the synchrotron motion of the single electron as a function of time. The amplitude is extracted from the measured and the simulated data by the fitting procedure illustrated in Fig. 4.11 . In the simulation, the rms rf cavity phase jitter is $\sigma_\xi = 6.0 \times 10^{-5}$ rad.

The measured and the simulated plots in Fig. 4.14 look very similar. They both exhibit a constant fight between the quantum excitation and the radiation damping. The intrinsic timing jitter of the SPAD detector was about 0.35 ns according to the manufacturer's specifications. Also, there could be other sources of timing jitter due to other active elements in the system (e.g., the signal discriminator). Therefore, what is observed in Figs. 4.11 and 4.13 is a sum of the actual synchrotron motion of the single electron and the random time

delays introduced by the detection system. Fortunately, when the collected data points are fitted by short pieces of sinusoidal curves, the values of the amplitudes in the fits are practically unaffected by the detection system's timing jitter (see Section 4.5.4). Therefore, the comparison of the measurement and the simulation in Fig. 4.14 is sound. One could also plot the dependence on time of the standard deviation of the detection time relative to the IOTA revolution marker σ_t, calculated in a small time interval, e.g., 0.1 sec, see Fig. 4.15.

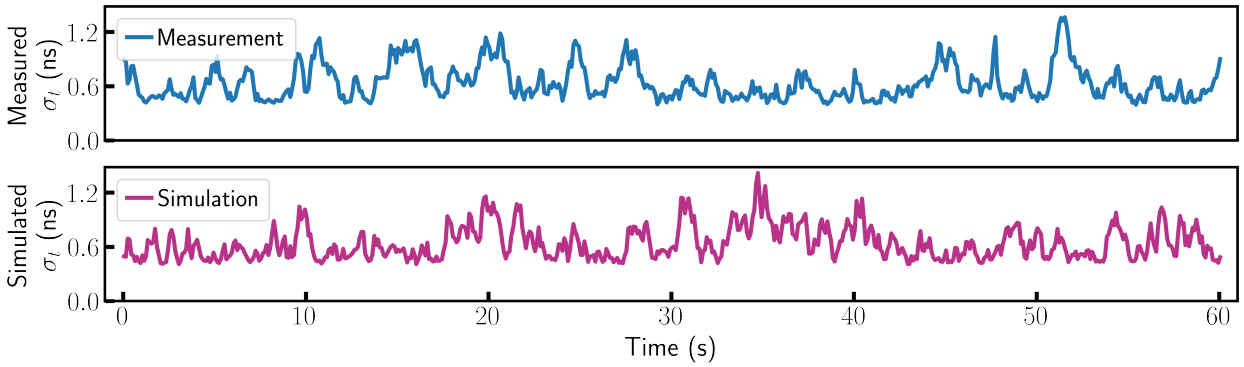

Figure 4.15: Standard deviation of the detection time relative to the IOTA revolution marker σ_t, calculated in a time window 0.1 sec, as a function of time. In the simulation, the SPAD's timing jitter is added as a random variable with a Gamma distribution with the mean 0.73 ns and the standard deviation 0.41 ns.

One can see a similar behavior in these plots — the fight between quantum excitation and radiation damping. However, σ_t never goes close to zero, because of the timing jitter of the detection system. In the simulation, shown in Fig. 4.15, this jitter was modeled as a random variable with a Gamma distribution with the mean 0.73 ns and the standard deviation 0.41 ns. The choice of Gamma distribution and the values of the parameters of the distribution will be justified below in Section 4.5.4 .

Now, let us focus on the analysis of the synchrotron motion amplitude (Fig. 4.14), because it is practically unaffected by the detection system's timing jitter $\sigma_t^{(\mathrm{det})}$. Clearly, one cannot expect a perfect agreement between the measurement and the simulation in Fig. 4.14, because it is a stochastic process. However, one can expect a good agreement between the

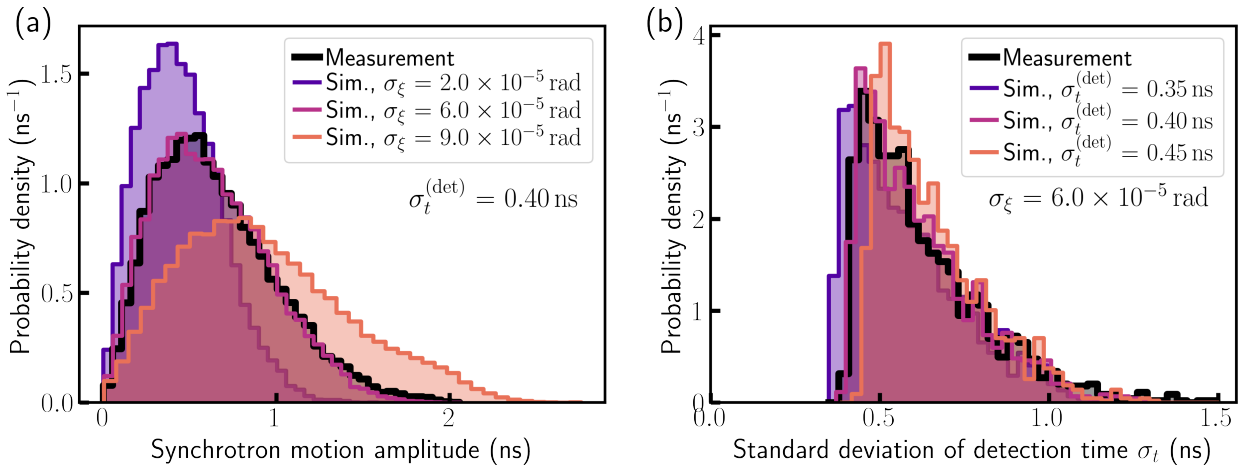

Figure 4.16: Panel (a) shows the comparison of the measured and simulated distributions of the synchrotron motion amplitude. The best agreement is achieved at the rms rf cavity phase jitter $\sigma_\xi = 6.0 \times 10^{-5}$ rad. Panel (b) presents the measured and the simulated histograms for the standard deviation of the detection time relative to the revolution marker σ_t, calculated in a time window 0.1 sec. The best agreement is achieved at the detection system's timing jitter $\sigma_t^{(\mathrm{det})} = 0.40$ ns.

distributions of the values of the synchrotron motion amplitude. Such comparison is shown in Fig. 4.16(a), which presents the measured distribution and the simulated distribution at three different values of the standard deviation of the rf cavity phase jitter σ_ξ. This allows us to find the most likely value of σ_ξ in IOTA, namely, $\sigma_\xi = 6.0 \times 10^{-5}$ rad. More than three values of σ_ξ were considered, but only three are shown in Fig. 4.16(a) to avoid overcrowding. One can say with certainty that σ_ξ is between 5.0×10^{-5} rad and 7.0×10^{-5} rad. In the simulations for Fig. 4.16(a) $\sigma_t^{(\mathrm{det})} = 0.40$ ns. However, the histograms in Fig. 4.16(a) are not sensitive to $\sigma_t^{(\mathrm{det})}$.

Further, it was decided to perform similar calculations for the histograms of σ_t at three different values of $\sigma_t^{(\mathrm{det})}$ and a fixed value of $\sigma_\xi = 6.0 \times 10^{-5}$ rad. The results are shown in Fig. 4.16(b). These results indicate that the value of our detection system's timing jitter was about 0.40 ns.

Using the same piecewise sinusoidal fit of the collected data (Fig. 4.13) one can plot the

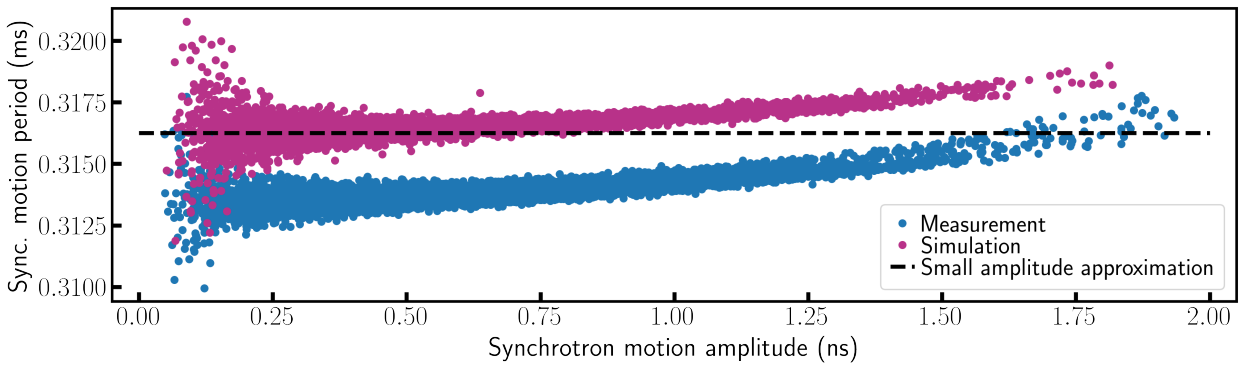

Figure 4.17: Synchrotron motion period as a function of synchrotron motion amplitude.

dependance of the synchrotron motion period on the synchrotron motion amplitude. The results are shown in Fig. 4.17 . Each point in this plot corresponds to an estimation of the period and the amplitude in a 25-ms-long interval in the collected or simulated data. The agreement between the simulation and the measurement is rather good. This shows that we understand the parameters of the IOTA ring well. The small-amplitude approximation for the synchrotron motion period in IOTA is

$$T_s = T_0 \sqrt{\frac{2\pi E_0}{q\eta_s e V_0 \cos\phi_s}} = 0.316\,\text{ms}, \tag{4.18}$$

which is very close to the measured small-amplitude synchrotron motion period 0.313 ms, which is shown in Fig. 4.17 as the black horizontal dashed line. In Eq. (4.18), T_0 is the IOTA revolution period, $T_0 = 133.3\,\text{ns}$. The relative error between the predicted (0.316 ms) and the measured (0.313 ms) small-amplitude synchrotron motion periods is under 1 %. Perhaps this is because of the errors in E_0 and V_0, which are of the same order of magnitude.

Interestingly, the synchrotron motion period is not a constant as a function of the synchrotron motion amplitude in Fig. 4.17 . This shows that the oscillations are not exactly harmonic. It is due to the fact that the synchrotron motion Hamiltonian [135, p. 244] is not a quadratic function of phase ϕ.

4.5.4 *Reconstruction of the detection system's delay distribution*

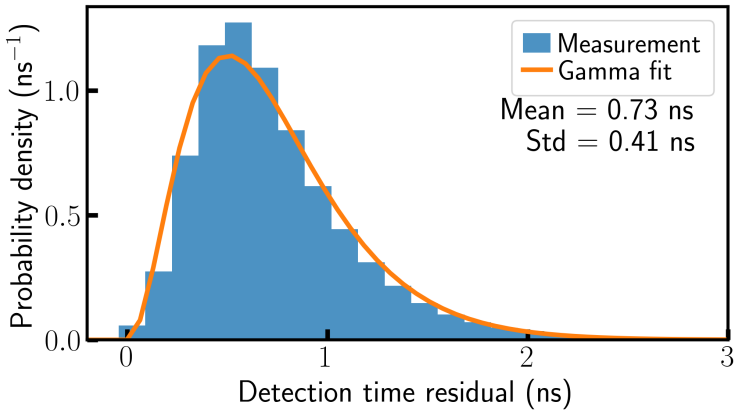

Figure 4.18: The distribution of the residuals between the recorded arrival time and the sinusoidal fit (see Fig. 4.11). A fit by a Gamma distribution with the mean 0.73 ns and the standard deviation 0.41 ns — the same as in the measured residuals. The histogram for the residuals had to be shifted horizontally. The optimal shift, 0.73 ns, was determined by minimizing the Kullback–Leibler divergence between the measured probability distribution and the Gamma distribution fit.

There exists a better way [than Fig. 4.16(b)] to determine the properties of the random time delays introduced by our detection system. One can plot the distribution of the residuals between the collected data points and the sinusoidal fit (see Fig. 4.11). With good accuracy, this distribution directly describes the random delays introduced by the detection system (the SPAD detector, the discriminator, and the picosecond event timer). This distribution is presented in Fig. 4.18, a 60-second-long data set was used. The standard deviation of this distribution is 0.41 ns. It is close to the value determined in Fig. 4.16(b), namely, 0.40 ns. It is higher than the manufacturer's specification for the intrinsic timing jitter of the SPAD detector (0.35 ns). This either means that our SPAD had a slightly higher timing jitter or that there was also a contribution from the discriminator (or both). We believe that the picosecond event timer did not introduce any detectable timing jitter. The distribution in Fig. 4.18 is asymmetric, because the random time delays cannot be negative. Of course, some portion of the residuals (see Fig. 4.11) was negative, but the distribution of the residuals was shifted to obtain Fig. 4.18 . The optimal value of the shift was found by minimizing the

Kullback-Leibler divergence, which is conventionally used to quantify the distance between two probability distributions. The optimal shift was 0.73 ns.

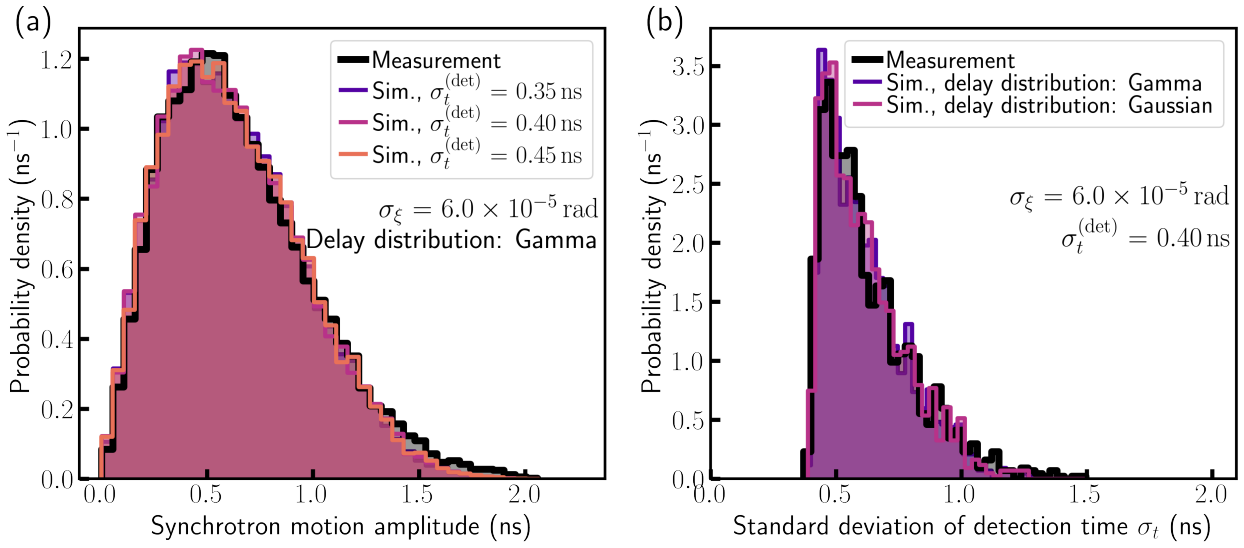

Figure 4.19: Panel (a) shows that the simulated distribution of synchrotron motion amplitudes does not depend (within statistical error) on the standard deviation of the detection system's delay $\sigma_t^{(\mathrm{det})}$ used in the simulation. Panel (b) shows that the simulated distribution of the standard deviation of detection time relative to the IOTA revolution marker σ_t does not depend (within statistical error) on the model of the detection system's delay (Gamma or Gaussian distribution).

Previously, a statement was made that the detection system's random time delays do not affect the synchrotron motion amplitudes obtained by fitting with short sinusoidal curves (see Fig. 4.13). To substantiate this claim, three simulated distributions of the synchrotron motion amplitude with three different values of the standard deviation of the detection system's delay $\sigma_t^{(\mathrm{det})}$ are presented in Fig. 4.19(a). In these simulations, the detection system's time delays were modeled by Gamma distributions with different $\sigma_t^{(\mathrm{det})}$, but with the same mean 0.73 ns. All three simulations agree with each other and with the measurement within the statistical error. Further, the type of the distribution (within reason) does not affect the results too. The Gamma distribution and the Gaussian distribution models of the random time delay are compared in Fig. 4.19(b). This comparison is performed for the

standard deviation σ_t of the detection time calculated in a time window of 0.1 sec.

4.6 Measurements with two SPAD detectors

In addition, some measurements were taken with an upgraded setup, which included two SPAD detectors separated by a beamsplitter, see Fig. 4.20 . Similar measurements with such Brown-Twiss interferometry of undulator radiation have also been reported previously in Ref. [121].

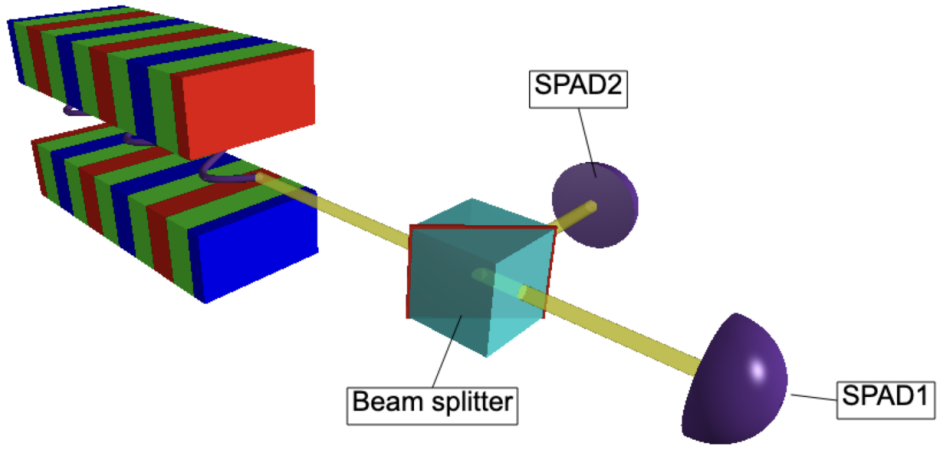

Figure 4.20: Illustration of the two-SPAD experiment setup.

Since our apparatus recorded the detection events for each detector individually, it was possible to see if there was any correlation (or anticorrelation) between the detection events in the two SPADs. The electron in IOTA is believed to be a classical electric current (no electron recoil after photon emission), which means that the radiated field should be in a Glauber state (classical state), according to [47–49]. In this case there should be no correlation (or anticorrelation) between the two detectors, the detection events should be absolutely independent. It is interesting to see if this is actually the case. If the quantum state of the radiated field deviates from the Glauber state towards, for example, the Fock state, then the number of coincidence events (simultaneous detections in both detectors) will be lower than the one expected for a classical radiation. For a perfect Fock state the

coincidence rate goes to zero — full anticorrelation. Anticorrelation was previously observed in a similar experiment with a radioactive cascade, which produces a quantum state close to a Fock state [138]. This experiment proved the existence of individual photons and, therefore, the quantum nature of light.

Several single-electron data sets were recorded with the picosecond event timer. Each data set was either 5-min-long or shorter, if the electron was lost before 5 minutes elapsed. The total recorded time was 1351.3 s. Henceforth, let us use the name "SPAD1" for the SPAD detector collecting the transmitted radiation without any change of direction of propagation and the name "SPAD2" for the SPAD detector collecting the radiation reflected at 90° to the initial direction of propagation, see Fig. 4.20 . The average photocount rates in SPAD1 and SPAD2 were 30.4 kHz and 15.2 kHz, respectively. The edge-pass filters (see Section 4.4) were removed here in order to achieve higher photocount rate. The average coincidence rate was 61.6 Hz. The beamsplitter used in this experiment [139] was a 50-50 beamsplitter, but only for unpolarized light. For π-polarization the ratio could be as far from 50-50 as 70-30 (depending on the wavelength). The undulator radiation was predominantly π-polarized. This is why the photocount rates in SPAD1 and SPAD2 have a ratio of about 2 to 1, rather than 1 to 1.

Using the recorded photocounts in SPAD1 and SPAD2, one could estimate the detection probabilities p_1 and p_2 during one revolution in IOTA in each of the two detectors as $p_1 = q_1/n_{\mathrm{tot}}$ and $p_2 = q_2/n_{\mathrm{tot}}$, where n_{tot} is the total number of IOTA revolutions in the entire 1351.3-second-long dataset, q_1 and q_2 are the total numbers of the detection events in SPAD1 and SPAD2, respectively. Then, using these probabilities, one could calculate the expected number μ of coincidence events during the total observation time 1351.3 s, assuming that the probability of a coincidence event is a product of the two probabilities,

$$p_{12} = p_1 p_2, \tag{4.19}$$

i.e., assuming that the detection events in SPAD1 and SPAD2 are independent from each other. The result was $\mu = 83\,027$. The measured number of coincidence events was $m = 83\,179$. Further, if the coincidence events are also assumed to be independent from each other, then they can be considered as another sequence of Bernoulli trials with the probability p_{12} that a coincidence event happens and the probability $1 - p_{12}$ that it does not happen during each IOTA revolution. In this case it is possible to calculate the expected standard deviation of the number of coincidence events as

$$\sigma_m = \sqrt{n_{\text{tot}} p_{12}(1 - p_{12})} = 288. \tag{4.20}$$

Thus, a hypothesis test can be constructed, where the null hypothesis is that the detection events in each SPAD detector are independent from each other and also are independent from the detection events in the other SPAD detector. If the null hypothesis is true, the measured number of coincidence events m follows a normal distribution (due to the central limit theorem) with the mean $\mu = 83\,027$ and the standard deviation $\sigma_m = 288$. The measured value $m = 83\,179$ corresponds to a P-value equal to 0.60. The P-value [133, p. 140] is the probability to observe a deviation from the expected value μ at least as extreme as the measured m. The obtained P-value is large and well above the conventional threshold value 0.05. Therefore, the deviation of the measured number of coincidence events m from the expected value μ is statistically insignificant and the null hypothesis cannot be rejected. Thus, we do not see any evidence of correlation or anticorrelation between the detection events in the two SPAD detectors.

4.6.1 Possible application in bunch length measurement

The data collected with two SPAD detectors can be used to determine the rms electron bunch duration in the ring at vanishing beam currents. An illustration is provided in Fig. 4.21,

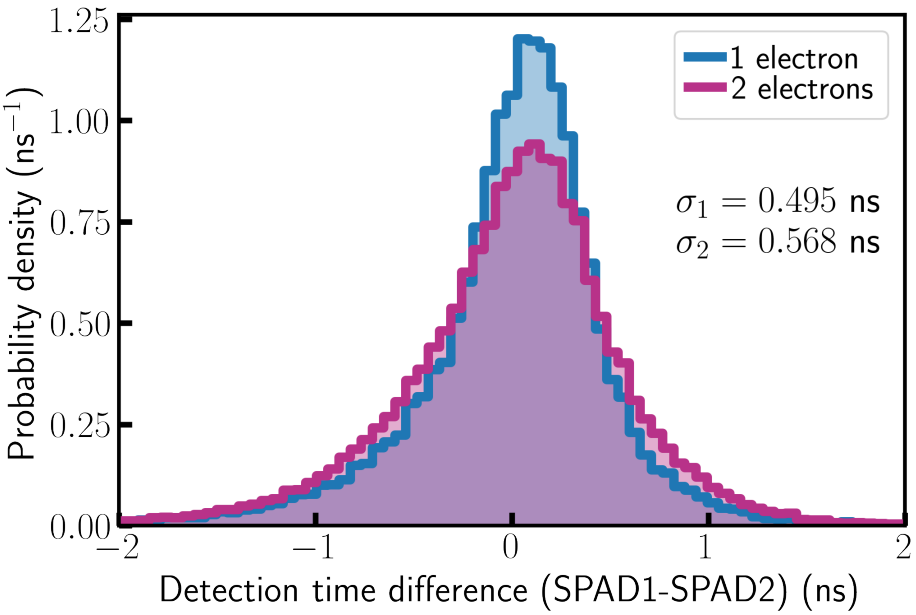

Figure 4.21: Detection time difference histograms for 1 and 2 electrons in the ring. These histograms are based on two 300-second-long data sets for 1 and 2 electrons.

namely, one can record one data set with a single electron in the ring, and another data set with two electrons in the ring. Then, one can select the events where a photocount was observed in each detector (coincidence events). Further, for each such event, the arrival time difference can be calculated between SPAD1 and SPAD2. Examples of histograms for the arrival time difference for 1 and 2 electrons in the ring are shown in Fig. 4.21 . Then, one can calculate the standard deviations of the arrival time difference $\sigma_t^{(1\mathrm{el})}$ and $\sigma_t^{(2\mathrm{el})}$ for the 1- and 2-electron cases, respectively. Finally, the rms electron bunch duration can be estimated as

$$\sigma_t = \sqrt{(\sigma_t^{(2\mathrm{el})})^2 - (\sigma_t^{(1\mathrm{el})})^2}. \tag{4.21}$$

The random time delays introduced by the SPAD detectors and the discriminator contribute significantly to $\sigma_t^{(2\mathrm{el})}$ and $\sigma_t^{(1\mathrm{el})}$. However, in the subtraction under the square root in Eq. (4.21) these contributions cancel each other and what is left is exactly σ_t^2. We considered 12 minutes of recorded data for 1 electron and 12 minutes for 2 electrons in the ring. For

these data sets, $\sigma_t^{(1el)} = 0.503\,\text{ns}$, $\sigma_t^{(2el)} = 0.568\,\text{ns}$, and $\sigma_t = 0.26\,\text{ns}$ (or $\sigma_z = c\sigma_t = 7.9\,\text{cm}$). To estimate the error of this measurement, the entire 12-minute-long data set was divided into three 4-minute-long data sets (for 1 and for 2 electrons in the ring), and three corresponding values of σ_z were obtained. The standard deviation of these three values was 0.5 cm. It gives an estimate for the statistical error of the measurement of $\sigma_z = 7.9\,\text{cm}$ by this method.

4.6.2 Possible further experiments

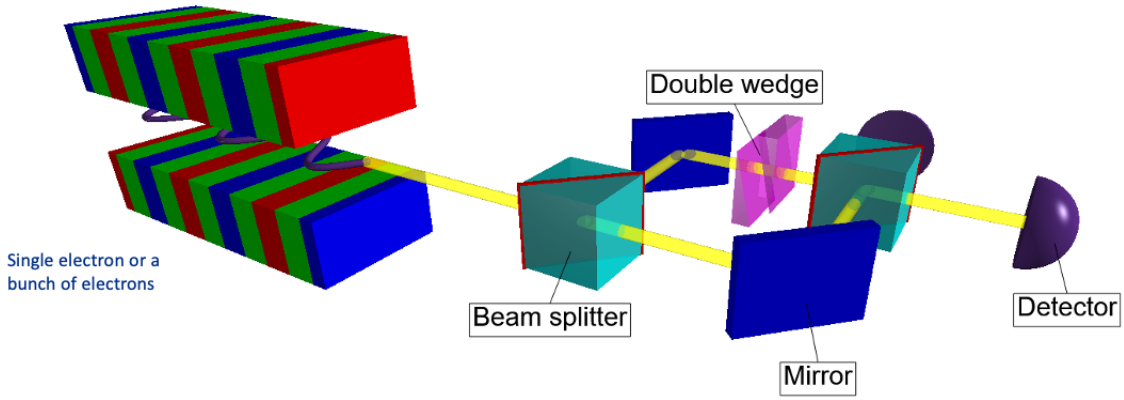

Figure 4.22: Illustration of the Mach-Zehnder interferometry of the undulator radiation.

A possible extension of the experiment with a single beamsplitter is a Mach-Zehnder interferometry of the undulator radiation in IOTA, see Fig. 4.22 . In this interferometer, the incoming radiation pulse is split into two in the first beam splitter. Then, the radiation pulse in one of the arms of the interferometer is delayed by a certain variable optical delay. In Fig. 4.22 a double wedge is used for illustration purposes. Further, the two radiation pulses interact in the second beamsplitter. Nowadays, the optical delay can be adjusted with a very small step, as small as 10 nm using piezo actuators. It can be shown that when the optical delay is slowly varied, one can observe oscillations of the intensities in the two outputs of the interferometer, see [138] for example. This interference pattern contains information about the temporal shape of the undulator radiation pulses, which are about 30 fs long. It may be

an interesting diagnostics tool for the radiation pulses in the time domain. One could also consider the Hong-Ou-Mandel interferometry [140–143].

This experiment can be carried out with a single electron or with an electron bunch. We believe that this experiment should begin by studying the radiation from an electron bunch with pinhole masks in front of the SPADs so that (1) the radiation is strongly attenuated and safe for the SPADs and (2) the on-axis radiation is studied, which results in a more pronounced interference pattern. In this case it is crucial to work with the fundamental harmonic of the undulator radiation, which has a maximum on axis, as opposed to the second harmonic, which has zero intensity on axis. With a 96.4 MeV beam, the SPADs are only sensitive to the second harmonic 400–800 nm. To move the fundamental harmonic to this spectral range, the beam energy has to be increased to about 150 MeV. It has not been achieved until very recently — at the time of writing.

CHAPTER 5

CONCLUSIONS

In our experiments with an electron bunch in IOTA it was shown that the turn-to-turn fluctuations var($\mathcal{N}$) of the number of detected undulator radiation photons per turn $\mathcal{N}$ have two contributions: (1) the Poisson contribution equal to $\langle\mathcal{N}\rangle$, due to the discrete quantum nature of light, and (2) the incoherence contribution $\frac{1}{M}\langle\mathcal{N}\rangle^2$, related to the interference of the fields generated by the electrons in the bunch and the fact that the relative electron positions and directions of motion change from turn to turn randomly due to the betatron motion, the synchrotron motion, quantum excitation, etc. Although the two contributions are different in nature (quantum and classical), there is a unified description in the framework of quantum optics using the density operator formalism [16].

A new equation was derived for the number of coherent modes M for an electron bunch with a Gaussian transverse density distribution, an arbitrary longitudinal density distribution, and non-negligible rms electron beam divergences. The rms bunch length is assumed to be significantly larger than the radiation wavelength. Equation (2.105) is presented for the first time, as beam divergence has been neglected in all previous considerations. Beam divergence can be neglected if it is significantly smaller than the characteristic radiation angle. Equation (2.105) is complex and includes a multidimensional integral. However, a computer program [77] has been developed for numerical computation of Eq. (2.105). It can be easily used for other storage rings if the required parameters are known. A very good agreement was obtained between the measurements and the simulations for the fluctuations of the number of detected photons at IOTA for the round electron beam, whose parameters were well-known. It was shown that such a good agreement would not be achieved if the electron beam divergence was neglected.

Further, it was proposed to use the measured fluctuations var($\mathcal{N}$) and Eq. (2.105) to infer some parameters of the electron bunch. This new fluctuations-based technique enabled

a measurement of the small vertical emittance of the flat electron beam in IOTA, which was unresolvable by the conventional synchrotron light monitors. This measurement was in agreement with another independent estimate based on the measured beam lifetime and a model for the beam lifetime assuming that the dominant particle loss mechanism was the Touschek scattering. This measurement in IOTA was only a proof-of-principle experiment. It used the undulator radiation in the near-infrared spectral range. The potential of this noninvasive fluctuations-based technique can be truly realized when it is used with ultraviolet or x-ray radiation and much smaller electron bunches. It was shown that the sensitivity of this technique improves with shorter wavelength and smaller bunch sizes. For example, our estimations indicate that it may be possible to measure the very small transverse beam emittances $\epsilon_x = 31.9\,\mathrm{pm}$, $\epsilon_y = 31.7\,\mathrm{pm}$ of a strongly coupled electron beam in the Advanced Photon Source Upgrade at Argonne using this new proposed method.

In our experiment with a single electron and a single binary photon detector, we have not yet observed any deviations of the undulator radiation photostatistics from a memoryless Bernoulli process. Our measurements with a Brown-Twiss interferometer (two SPAD detectors separated by a beamsplitter) show no evidence of correlation (or anticorrelation) in the detected photon pairs. Thus, so far, all of our observations confirm the prediction [47–49] that at negligible electron recoil the synchrotron radiation, produced by a single electron, is in a Glauber state. In the future, the Mach-Zehnder interferometry of the undulator radiation could be carried out in IOTA. It would allow to investigate the structure of the radiation pulses in the time domain with a sub-femtosecond resolution.

The detection arrival times can be used to study the synchrotron motion of a single electron and to infer some useful parameters of the ring, such as the rms rf cavity phase jitter and the synchrotron motion period as a function of amplitude. In the future, in IOTA, this diagnostics of the longitudinal motion can complement the diagnostics of the transverse motion [132, 144] and facilitate a complete 3D tracking of a single electron in the ring.

BIBLIOGRAPHY

[1] John M. J. Madey. "Stimulated Emission of Bremsstrahlung in a Periodic Magnetic Field". In: *Journal of Applied Physics* 42.5 (1971), pp. 1906–1913. DOI: 10.1063/1.1660466. eprint: https://doi.org/10.1063/1.1660466. URL: https://doi.org/10.1063/1.1660466.

[2] Kwang-Je Kim, Zhirong Huang, and Ryan Lindberg. *Synchrotron radiation and free-electron lasers*. Cambridge University Press, 2017.

[3] "Time-resolved serial femtosecond crystallography at the European XFEL". In: *Nature Methods* 17.1 (2020), pp. 73–78. DOI: 10.1038/s41592-019-0628-z. URL: https://doi.org/10.1038/s41592-019-0628-z.

[4] *European XFEL homepage*. https://www.xfel.eu/. Accessed: 2021-08-10.

[5] Nenad Ban et al. "The Complete Atomic Structure of the Large Ribosomal Subunit at 2.4 Å Resolution". In: *Science* 289.5481 (2000), pp. 905–920. ISSN: 0036-8075. DOI: 10.1126/science.289.5481.905. eprint: https://science.sciencemag.org/content/289/5481/905.full.pdf. URL: https://science.sciencemag.org/content/289/5481/905.

[6] *The Nobel Prize in Chemistry 2009*. https://www.nobelprize.org/prizes/chemistry/2009/summary/. NobelPrize.org. Nobel Prize Outreach AB 2021. Fri. 9 Jul 2021.

[7] S. Frydrych et al. "Demonstration of X-ray Thomson scattering as diagnostics for miscibility in warm dense matter". In: *Nature Communications* 11.1 (2020), p. 2620. DOI: 10.1038/s41467-020-16426-y. URL: https://doi.org/10.1038/s41467-020-16426-y.

[8] *LCLS homepage*. https://portal.slac.stanford.edu/sites/lcls_public/Pages/Default.aspx. Accessed: 2021-08-10.

[9] *LCLS-II homepage*. https://lcls.slac.stanford.edu/lcls-ii. Accessed: 2021-08-10.

[10] *SACLA homepage*. http://xfel.riken.jp/eng/. Accessed: 2021-08-10.

[11] *Advanced Photon Source parameters*. https://www.aps.anl.gov/files/APS-sync/technical_bulletins/files/APS_1421579.pdf. Accessed: 2021-2-5.

[12] *Swiss FEL homepage*. https://www.psi.ch/swissfel/. Accessed: 2021-08-10.

[13] Malvin C Teich et al. "Statistical properties of wiggler and bending-magnet radiation from the Brookhaven Vacuum-Ultraviolet electron storage ring". In: *Phys. Rev. Lett.* 65.27 (1990), p. 3393.

[14] Vadim Sajaev. *Determination of longitudinal bunch profile using spectral fluctuations of incoherent radiation*. Report No ANL/ASD/CP-100935. Argonne National Laboratory, 2000.

[15] V Sajaev. "Measurement of bunch length using spectral analysis of incoherent radiation fluctuations". In: *AIP Conf. Proc.* Vol. 732. 1. AIP, 2004, pp. 73–87.

[16] Ihar Lobach et al. "Statistical properties of spontaneous synchrotron radiation with arbitrary degree of coherence". In: *Phys. Rev. Accel. Beams* 23 (9 Sept. 2020), p. 090703. DOI: 10.1103/PhysRevAccelBeams.23.090703. URL: https://link.aps.org/doi/10.1103/PhysRevAccelBeams.23.090703.

[17] Fernando Sannibale et al. "Absolute bunch length measurements by incoherent radiation fluctuation analysis". In: *Phys. Rev. ST Accel. Beams* 12.3 (2009), p. 032801.

[18] P Catravas et al. "Measurement of electron-beam bunch length and emittance using shot-noise-driven fluctuations in incoherent radiation". In: *Phys. Rev. Lett.* 82.26 (1999), p. 5261.

[19] Kwang-Je Kim. "Start-up noise in 3-D self-amplified spontaneous emission". In: *Nucl. Instrum. Methods Phys. Res., Sect. A* 393.1-3 (1997), pp. 167–169.

[20] Stephen Benson and John MJ Madey. "Shot and quantum noise in free electron lasers". In: *Nucl. Instrum. Methods Phys. Res., Sect. A* 237.1-2 (1985), pp. 55–60.

[21] Evgeny L Saldin, EV Schneidmiller, and Mikhail V Yurkov. *The physics of free electron lasers*. Springer Science & Business Media, 2013.

[22] C Pellegrini, A Marinelli, and S Reiche. "The physics of x-ray free-electron lasers". In: *Rev. Mod. Phys.* 88.1 (2016), p. 015006.

[23] W Becker and M Suhail Zubairy. "Photon statistics of a free-electron laser". In: *Phys. Rev. A* 25.4 (1982), p. 2200.

[24] W Becker and JK McIver. "Fully quantized many-particle theory of a free-electron laser". In: *Phys. Rev. A* 27.2 (1983), p. 1030.

[25] W Becker and JK McIver. "Photon statistics of the free-electron-laser startup". In: *Phys. Rev. A* 28.3 (1983), p. 1838.

[26] Sergei Antipov et al. "IOTA (Integrable Optics Test Accelerator): facility and experimental beam physics program". In: *J. Instrum.* 12.03 (2017), T03002.

[27] M. Hofer et al. "Nonlinear Optics Measurements in IOTA". In: (Mar. 2021). DOI: 10.2172/1779489. URL: https://www.osti.gov/biblio/1779489.

[28] A. Romanov et al. "Recent results and opportunities at the IOTA facility". In: (Jan. 2020). URL: https://www.osti.gov/biblio/1614724.

[29] Sergey A Antipov, Sergei Nagaitsev, and Alexander Valishev. "Single-particle dynamics in a nonlinear accelerator lattice: attaining a large tune spread with octupoles in IOTA". In: *Journal of Instrumentation* 12.04 (2017), P04008.

[30] E. Stern. "Suppression of Instabilities Generated by an Anti-Damper with a Nonlinear Magnetic Element in IOTA". In: (Apr. 2018). URL: https://www.osti.gov/biblio/1437283.

[31] N. Kuklev et al. "Experimental Demonstration of the Henon-Heiles Quasi-Integrable System at IOTA". In: (Jan. 2019). URL: https://www.osti.gov/biblio/1560831.

[32] V. Danilov and S. Nagaitsev. "Nonlinear accelerator lattices with one and two analytic invariants". In: *Phys. Rev. ST Accel. Beams* 13 (8 Aug. 2010), p. 084002. DOI: 10.1103/PhysRevSTAB.13.084002. URL: https://link.aps.org/doi/10.1103/PhysRevSTAB.13.084002.

[33] V. Lebedev et al. "The design of Optical Stochastic Cooling for IOTA". In: *Journal of Instrumentation* 16.05 (May 2021), T05002. ISSN: 1748-0221. DOI: 10.1088/1748-0221/16/05/t05002. URL: http://dx.doi.org/10.1088/1748-0221/16/05/T05002.

[34] Valeri Lebedev and AL Romanov. "Optical stochastic cooling at the IOTA ring". In: *Proceedings of COOL2015, Newport News VA* (2015), pp. 123–127.

[35] J. D. Jarvis et al. *Optical Stochastic Cooling Experiment At The Fermilab IOTA Ring*. 2018. arXiv: 1808.07922 [physics.acc-ph].

[36] M. B. Andorf et al. "Computation and numerical simulation of focused undulator radiation for optical stochastic cooling". In: *Phys. Rev. Accel. Beams* 21 (10 Oct. 2018), p. 100702. DOI: 10.1103/PhysRevAccelBeams.21.100702. URL: https://link.aps.org/doi/10.1103/PhysRevAccelBeams.21.100702.

[37] K-J Kim. "Analysis of optical stochastic cooling including transverse effects". In: *Proc. 16th Particle Accelerator Conference, Dallas, Texas, 1-5 May 1995*. Vol. 4. IEEE. 1995, pp. 2786–2788.

[38] A. A. Mikhailichenko and M. S. Zolotorev. "Optical stochastic cooling". In: *Phys. Rev. Lett.* 71 (25 Dec. 1993), pp. 4146–4149. DOI: 10.1103/PhysRevLett.71.4146. URL: https://link.aps.org/doi/10.1103/PhysRevLett.71.4146.

[39] G. Stancari et al. "Beam physics research with the IOTA electron lens". In: *Journal of Instrumentation* 16.05 (May 2021), P05002. DOI: 10.1088/1748-0221/16/05/p05002. URL: https://doi.org/10.1088/1748-0221/16/05/p05002.

[40] B Cathey et al. "Calculations of detuning with amplitude for the McMillan electron lens in the Fermilab Integrable Optics Test Accelerator (IOTA)". In: *Journal of Instrumentation* 16.03 (2021), P03041.

[41] R.C. Dhuley et al. "Design of a compact, cryogen-free superconducting solenoid for the electron lens of the Fermilab Integrable Optics Test Accelerator (IOTA)". In: *Journal of Instrumentation* 16.03 (Mar. 2021), T03009. DOI: 10.1088/1748-0221/16/03/t03009. URL: https://doi.org/10.1088/1748-0221/16/03/t03009.

[42] S. Nagaitsev et al. "McMillan electron lens in a system with space charge". In: *Journal of Instrumentation* 16.03 (Mar. 2021), P03047. DOI: 10.1088/1748-0221/16/03/p03047. URL: https://doi.org/10.1088/1748-0221/16/03/p03047.

[43] Teng Chen and John MJ Madey. "Observation of sub-Poisson fluctuations in the intensity of the seventh coherent spontaneous harmonic emitted by a RF linac free-electron laser". In: *Phys. Rev. Lett.* 86.26 (2001), p. 5906.

[44] Teng Chen. "Photon statistics of coherent harmonic radiation of a linac free electron laser". Ph.D. thesis. Duke University, 1999.

[45] Jeong-Wan Park. "An Investigation of Possible Non-Standard Photon Statistics in a Free-Electron Laser". PhD thesis. University of Hawaii at Manoa, 2019. URL: http://hdl.handle.net/10125/66233.

[46] Joseph W Goodman. *Statistical optics*. John Wiley & Sons, 2015.

[47] Roy J Glauber. "The quantum theory of optical coherence". In: *Phys. Rev.* 130.6 (1963), p. 2529.

[48] Roy J Glauber. "Coherent and incoherent states of the radiation field". In: *Phys. Rev.* 131.6 (1963), p. 2766.

[49] Roy J Glauber. "Some notes on multiple-boson processes". In: *Phys. Rev.* 84.3 (1951), p. 395.

[50] Ihar Lobach et al. "Measurements of undulator radiation power noise and comparison with ab initio calculations". In: *Phys. Rev. Accel. Beams* 24 (4 Apr. 2021), p. 040701. DOI: 10.1103/PhysRevAccelBeams.24.040701. URL: https://link.aps.org/doi/10.1103/PhysRevAccelBeams.24.040701.

[51] Kwang-Je Kim. "Characteristics of synchrotron radiation". In: *AIP Conf. Proc.* Vol. 184. 1. AIP. 1989, pp. 565–632.

[52] Ihar Lobach et al. "Study of Fluctuations in Undulator Radiation in the IOTA Ring at Fermilab". In: *Proc. 10th International Partile Accelerator Conference (IPAC'19), Melbourne, Australia, 19-24 May 2019* (Melbourne, Australia). 10. June 2019, pp. 777–780. ISBN: 978-3-95450-208-0. URL: http://jacow.org/ipac2019/papers/moprb088.pdf.

[53] Christine Silberhorn. "Detecting quantum light". In: *Contemporary Physics* 48.3 (2007), pp. 143–156.

[54] Alice Meda et al. "Photon-number correlation for quantum enhanced imaging and sensing". In: *J. Opt.* 19.9 (2017), p. 094002.

[55] Luiz Davidovich. "Sub-Poissonian processes in quantum optics". In: *Rev. Mod. Phys.* 68.1 (1996), p. 127.

[56] ZY Ou, CK Hong, and L Mandel. "Relation between input and output states for a beam splitter". In: *Optics Communications* 63.2 (1987), pp. 118–122.

[57] John Hubbard. "Calculation of partition functions". In: *Phys. Rev. Lett.* 3.2 (1959), p. 77.

[58] Alexander M. Lazaruk and Nikolay V. Karelin. "Average number of coherent modes for pulse random fields". In: *International Conference on Correlation Optics*. Ed. by Oleg V. Angelsky. Vol. 3317. International Society for Optics and Photonics. SPIE, 1997, pp. 12–18. URL: https://doi.org/10.1117/12.295671.

[59] Kwang-Je Kim. "Temporal and transverse coherence of self-amplified spontaneous emission". In: *AIP Conf. Proc.* Vol. 413. 1. AIP. 1997, pp. 3–13.

[60] Ihar Lobach et al. "Transverse Beam Emittance Measurement by Undulator Radiation Power Noise". In: *Phys. Rev. Lett.* 126 (13 Apr. 2021), p. 134802. DOI: 10.1103/PhysRevLett.126.134802. URL: https://link.aps.org/doi/10.1103/PhysRevLett.126.134802.

[61] J Haïssinski. "Exact longitudinal equilibrium distribution of stored electrons in the presence of self-fields". In: *Il Nuovo Cimento B (1971-1996)* 18.1 (1973), pp. 72–82.

[62] Brian Fellenz and Jim Crisp. "An improved resistive wall monitor". In: *AIP Conference Proceedings* 451.1 (1998), pp. 446–453. DOI: 10.1063/1.57030.

[63] Evgenij L Saldin, Evgeny A Schneidmiller, and MV Yurkov. "Statistical properties of radiation from VUV and X-ray free electron laser". In: *Opt. Commun.* 148.4-6 (1998), pp. 383–403.

[64] Stephen O Rice. "Mathematical analysis of random noise". In: *Bell Syst. Tech. J.* 23.3 (1944), pp. 282–332.

[65] Zhirong Huang and Kwang-Je Kim. "Review of x-ray free-electron laser theory". In: *Phys. Rev. ST Accel. Beams* 10.3 (2007), p. 034801.

[66] Avner Amir, Ilario Boscolo, and Luis R Elias. "Spontaneous emission in the waveguide free-electron laser". In: *Phys. Rev. A* 32.5 (1985), p. 2864.

[67] Gianluca Geloni, Vitali Kocharyan, and Evgeni Saldin. "On quantum effects in spontaneous emission by a relativistic electron beam in an undulator". In: *arXiv:1202.0691* (2012).

[68] James A Clarke. "The science and technology of undulators and wigglers". In: 4. Oxford University Press on Demand, 2004, pp. 66–67.

[69] Ihar Lobach. *The source code for calculation of spectral-angular distribution of wiggler radiation*. https://github.com/IharLobach/wigrad. 2020.

[70] O Chubar et al. "Wavefront propagation simulations for beamlines and experiments with "Synchrotron Radiation Workshop"". In: *J. Phys. Conf. Ser.* Vol. 425. 16. IOP Publishing. 2013, p. 162001.

[71] Stephen Gottschalk et al. "Design and Performance of the NLCTA-Echo 7 Undulators". In: *Proc. 34th International Free-Electron Laser Conference, Nara, Japan, 26-31 Aug. 2012* (Nara, Japan).

[72] *Hamamatsu InGaAs PIN photodiode G11193-10R*. https://www.hamamatsu.com/us/en/product/type/G11193-10R/index.html. Accessed: 2020-11-18.

[73] Sergei Nagaitsev. "Intrabeam scattering formulas for fast numerical evaluation". In: *Phys. Rev. ST Accel. Beams* 8.6 (2005), p. 064403.

[74] Karl LF Bane et al. "Intrabeam scattering analysis of measurements at KEK's Accelerator Test Facility damping ring". In: *Phys. Rev. ST Accel. Beams* 5.8 (2002), p. 084403.

[75] Alexander Wu Chao, Karl Hubert Mess, et al. *Handbook of accelerator physics and engineering*. World scientific, 2013.

[76] Valeri Lebedev. "Understanding Lifetimes, Beam Sizes and Scattering in IOTA". FAST/IOTA Collaboration Meeting, Fermilab, Jun 15-17, 2020.

[77] Ihar Lobach. *The source code for calculation of fluctuations in wiggler radiation*. https://github.com/IharLobach/fur. 2020.

[78] A. T. Georges. "From Noise To Coherence In A Free-Electron Laser Oscillator". In: *Free-Electron Generators of Coherent Radiation*. Ed. by Charles A. Brau, Stephen F. Jacobs, and Marlan O. Scully. Vol. 0453. International Society for Optics and Photonics. SPIE, 1984, pp. 297–305. DOI: 10.1117/12.947111. URL: https://doi.org/10.1117/12.947111.

[79] Julio Gea-Banacloche. "Quantum theory of the free-electron laser: Large gain, saturation, and photon statistics". In: *Physical Review A* 31.3 (1985), p. 1607.

[80] N. Kuklev et al. "Synchrotron Radiation Beam Diagnostics at IOTA — Commissioning Performance and Upgrade Efforts". In: *Proc. 10th International Particle Accelerator Conference (IPAC'19), Melbourne, Australia, 19-24 May 2019* (Melbourne, Australia). International Particle Accelerator Conference 10. Geneva, Switzerland: JACoW Publishing, June 2019, pp. 2732–2735. ISBN: 978-3-95450-208-0. DOI: doi:10.18429/JACoW-IPAC2019-WEPGW103. URL: http://jacow.org/ipac2019/papers/wepgw103.pdf.

[81] Albert W Hull and NH Williams. "Determination of Elementary Charge e from Measurements of Shot-Effect". In: *Phys. Rev.* 25.2 (1925), p. 147.

[82] John Bertrand Johnson. "Thermal agitation of electricity in conductors". In: *Phys. Rev.* 32.1 (1928), p. 97.

[83] Simon van der Meer. "Stochastic Cooling and the Accumulation of Antiprotons". In: *Nobel Lecture* (Dec. 1984). URL: https://www.nobelprize.org/prizes/physics/1984/meer/lecture/.

[84] W. Schottky. "Über spontane Stromschwankungen in verschiedenen Elektrizitätsleitern". In: *Annalen der Physik* 362.23 (1918), pp. 541–567. DOI: 10.1002/andp.19183622304.

[85] Daniel Boussard. *Schottky noise and beam transfer function diagnostics*. Tech. rep. CERN-SPS-86-11-ARF. May 1986, 42 p. DOI: 10.5170/CERN-1987-003-V-2.416. URL: http://cds.cern.ch/record/168143.

[86] Simon van der Meer. "Diagnostics with Schottky noise". In: *Frontiers of Particle Beams; Observation, Diagnosis and Correction*. Springer, 1989, pp. 423–433.

[87] Fritz Caspers et al. "The 4.8 GHz LHC Schottky pick-up system". In: *2007 IEEE Particle Accelerator Conference (PAC)*. IEEE. 2007, pp. 4174–4176.

[88] M S Zolotorev and G V Stupakov. *Fluctuational interferometry for measurement of short pulses of incoherent radiation*. Tech. rep. SLAC-PUB-7132. Stanford, CA: SLAC, Mar. 1996. URL: http://cds.cern.ch/record/305348.

[89] James D. Bjorken and Sekazi K. Mtingwa. "Intrabeam scattering". In: *Part. Accel.* 13.FERMILAB-PUB-82-47-THY (1982), pp. 115–143.

[90] Sergei Nagaitsev. "Intrabeam scattering formulas for fast numerical evaluation". In: *Phys. Rev. ST Accel. Beams* 8 (6 June 2005), p. 064403. DOI: 10.1103/PhysRevSTAB.8.064403. URL: https://link.aps.org/doi/10.1103/PhysRevSTAB.8.064403.

[91] *The Bokeh Visualization Library*. https://bokeh.org/. Accessed: 2021-07-17.

[92] Ihar Lobach. *The source code for the bunch profile monitor*. https://github.com/IharLobach/bunch-profile-monitor. 2020.

[93] Valeri A Lebedev and SA Bogacz. "Betatron motion with coupling of horizontal and vertical degrees of freedom". In: *J. Instrum.* 5.10 (2010), P10010.

[94] *Texas Instruments Wideband Operational Amplifier THS4303*. http://www.ti.com/lit/ds/symlink/ths4304.pdf. Accessed: 2020-11-18.

[95] Julius Orion Smith. *Physical audio signal processing: For virtual musical instruments and audio effects*. W3K publishing, 2010.

[96] *MACOM H-9 Hybrid Junction*. https://cdn.macom.com/datasheets/H-9.pdf. Accessed: 2020-11-18.

[97] Martin Reiser and Patrick O'Shea. "Theory and design of charged particle beams". In: vol. 312. Wiley Online Library, 1994. Chap. 6, pp. 483–486.

[98] Valeri Lebedev. *Report on Single and Multiple Intrabeam Scattering Measurements in IOTA Ring in Fermilab*. Report No FERMILAB-TM-2750-AD. Fermilab, 2020.

[99] C. Bernardini et al. "Lifetime and Beam Size in a Storage Ring". In: *Phys. Rev. Lett.* 10 (9 May 1963), pp. 407–409. DOI: 10.1103/PhysRevLett.10.407. URL: https://link.aps.org/doi/10.1103/PhysRevLett.10.407.

[100] Nicola Carmignani. "Touschek Lifetime Studies and Optimization of the European Synchrotron Radiation Facility". pp. 25–26. PhD thesis. Pisa U., 2014. DOI: 10.1007/978-3-319-25798-3.

[101] V. Lebedev. "Intrabeam Scattering". In: *Handbook of Accelerator Physics and Engineering*. Ed. by A. Chao et al. World Scientific, 2013, pp. 155–158.

[102] Anton Piwinski. *The Touschek effect in strong focusing storage rings*. 1999. arXiv: physics/9903034 [physics.acc-ph].

[103] Peter Tenenbaum and Tsumoru Shintake. "Measurement of small electron-beam spots". In: *Annual Review of Nuclear and Particle Science* 49.1 (1999), pp. 125–162.

[104] Hiroshi Sakai et al. "Measurement of an electron beam size with a laser wire beam profile monitor". In: *Phys. Rev. ST Accel. Beams* 4 (2 Feb. 2001), p. 022801. DOI: 10.1103/PhysRevSTAB.4.022801. URL: https://link.aps.org/doi/10.1103/PhysRevSTAB.4.022801.

[105] *Advanced Photon Source Upgrade Project, Final Design Report*. Tech. rep. APSU-2.01-RPT-003. Chapter 2, Table 2.1; Chapter 4, Table 4.62. Lemont, IL: Argonne National Laboratory, May 2019. URL: https://www.aps.anl.gov/APS-Upgrade/Documents.

[106] David C. Burnham and Donald L. Weinberg. "Observation of Simultaneity in Parametric Production of Optical Photon Pairs". In: *Phys. Rev. Lett.* 25 (2 July 1970), pp. 84–87. DOI: 10.1103/PhysRevLett.25.84. URL: https://link.aps.org/doi/10.1103/PhysRevLett.25.84.

[107] Vladimir Borisovich Berestetskii, Evgenii Mikhailovich Lifshitz, and Lev Petrovich Pitaevskii. *Quantum Electrodynamics: Volume 4*. Vol. 4. Butterworth-Heinemann, 1982.

[108] Ihar Lobach. *Quantum effects in undulator radiation: Proposed experiments and results of theoretical analysis*. https://indico.fnal.gov/event/18978/. Budker Seminar, November 2018.

[109] Ihar Lobach. *Dirac-Volkov Model; Glauber's Model; IOTA Experiment Ideas*. https://indico.fnal.gov/event/18395/contributions/46989/. Workshop on Single-Electron Experiments in IOTA, November 2018.

[110] A. A. Sokolov et al. "Two-photon synchrotron emission". In: *Soviet Physics Journal* 19.9 (1976), pp. 1139–1144. DOI: 10.1007/BF00891463. URL: https://doi.org/10.1007/BF00891463.

[111] Erik Lötstedt and Ulrich D. Jentschura. "Correlated two-photon emission by transitions of Dirac-Volkov states in intense laser fields: QED predictions". In: *Phys. Rev. A* 80 (5 Nov. 2009), p. 053419. DOI: 10.1103/PhysRevA.80.053419. URL: https://link.aps.org/doi/10.1103/PhysRevA.80.053419.

[112] Daniel Seipt and Burkhard Kämpfer. "Two-photon Compton process in pulsed intense laser fields". In: *Phys. Rev. D* 85 (10 May 2012), p. 101701. DOI: 10.1103/PhysRevD.85.101701. URL: https://link.aps.org/doi/10.1103/PhysRevD.85.101701.

[113] Daniel Seipt. "Strong-Field QED Processes in Short Laser Pulses". PhD thesis. Dresden, Tech. U., ITP, 2012.

[114] VI Ritus. "Quantum effects of the interaction of elementary particles with an intense electromagnetic field". In: *Journal of Soviet Laser Research* 6.5 (1985), pp. 497–617.

[115] Max S Zolotorev and Kirk T McDonald. "Classical radiation processes in the Weizsacker-Williams approximation". In: *arXiv preprint physics/0003096* (2000).

[116] CF v Weizsäcker. "Ausstrahlung bei Stößen sehr schneller Elektronen". In: *Zeitschrift für Physik* 88.9-10 (1934), pp. 612–625.

[117] Evan J Williams. *Correlation of certain collision problems with radiation theory*. Levin & Munksgaard, 1935.

[118] Daniil M Wolkow. "Über eine klasse von lösungen der diracschen gleichung". In: *Zeitschrift für Physik* 94.3-4 (1935), pp. 250–260.

[119] *FACET-II facility*. https://portal.slac.stanford.edu/sites/ard_public/facet/Pages/FACET-II.aspx. Accessed: 2021-06-17.

[120] A.N. Aleshaev et al. "A study of the influence of synchrotron radiation quantum fluctuations on the synchrotron oscillations of a single electron using undulator radiation". In: *Nuclear Instruments and Methods in Physics Research Section A: Accelerators, Spectrometers, Detectors and Associated Equipment* 359.1 (1995). Proceedings of the 10th National Synchrotron Radiation Conference, pp. 80–84. ISSN: 0168-9002. DOI: https://doi.org/10.1016/0168-9002(96)88028-4. URL: https://www.sciencedirect.com/science/article/pii/0168900296880284.

[121] I.V. Pinayev et al. "Experiments with undulator radiation of a single electron". In: *Nuclear Instruments and Methods in Physics Research Section A: Accelerators, Spectrometers, Detectors and Associated Equipment* 341.1 (1994), pp. 17–20. ISSN: 0168-9002. DOI: https://doi.org/10.1016/0168-9002(94)90308-5. URL: https://www.sciencedirect.com/science/article/pii/0168900294903085.

[122] I.V. Pinayev et al. "A study of the influence of the stochastic process on the synchrotron oscillations of a single electron circulated in the VEPP-3 storage ring". In: *Nuclear Instruments and Methods in Physics Research Section A: Accelerators, Spectrometers, Detectors and Associated Equipment* 375.1 (1996). Proceedings of the 17th International Free Electron Laser Conference, pp. 71–73. ISSN: 0168-9002. DOI: https://doi.org/10.1016/0168-9002(95)01350-4. URL: https://www.sciencedirect.com/science/article/pii/0168900295013504.

[123] Roman Klein et al. "Operation of the Metrology Light Source as a primary radiation source standard". In: *Phys. Rev. ST Accel. Beams* 11 (11 Nov. 2008), p. 110701. DOI: 10.1103/PhysRevSTAB.11.110701. URL: https://link.aps.org/doi/10.1103/PhysRevSTAB.11.110701.

[124] Roman Klein, Reiner Thornagel, and Gerhard Ulm. "From single photons to milliwatt radiant power—electron storage rings as radiation sources with a high dynamic range". In: *Metrologia* 47.5 (Aug. 2010), R33–R40. DOI: 10.1088/0026-1394/47/5/r02. URL: https://doi.org/10.1088/0026-1394/47/5/r02.

[125] Carlo Bernardini. "AdA:The First Electron-Positron Collider". In: *Physics in Perspective* 6.2 (2004), pp. 156–183. DOI: 10.1007/s00016-003-0202-y. URL: https://doi.org/10.1007/s00016-003-0202-y.

[126] Luisa Bonolis and Giulia Pancheri. *Bruno Touschek and AdA: from Frascati to Orsay. In memory of Bruno Touschek, who passed away 40 years ago, on May 25th, 1978.* 2018. arXiv: 1805.09434 [physics.hist-ph].

[127] *SPCM-AQRH Single-Photon Counting Module.* https://www.excelitas.com/product/spcm-aqrh. Accessed: 2021-5-4.

[128] *HydraHarp 400 — Multichannel Picosecond Event Timer & TCSPC Module.* https://www.picoquant.com/products/category/tcspc-and-time-tagging-modules/hydraharp-400-multichannel-picosecond-event-timer-tcspc-module. Accessed: 2021-06-18.

[129] *Node-RED, a flow-based programming tool.* https://nodered.org/. Accessed: 2021-06-24.

[130] Giulio Stancari. *Detecting a Single Electron in IOTA*. https://indico.fnal.gov/event/18395/timetable. Workshop on Single-Electron Experiments in IOTA, November 2018.

[131] Aleksandr Romanov. *Obtaining a Single Electron in IOTA*. https://indico.fnal.gov/event/18395/timetable. Workshop on Single-Electron Experiments in IOTA, November 2018.

[132] Aleksandr Romanov et al. *Experimental 3-dimensional tracking of the dynamics of a single electron in the Fermilab Integrable Optics Test Accelerator (IOTA)*. 2020. arXiv: 2012.04148 [physics.acc-ph].

[133] RJ Freund, WJ Wilson, and DL Mohr. *Statistical Methods*. Academic Press, Burlington, MA, USA, 2010.

[134] Ihar Lobach. *The source code for simulation of the longitudinal motion of a single electron in a storage ring*. https://github.com/IharLobach/ursse. 2020.

[135] Shyh-Yuan Lee. *Accelerator physics*. World Scientific Publishing, 2018.

[136] Helmut Burkhardt. *Monte Carlo generation of the energy spectrum of synchrotron radiation*. http://cds.cern.ch/record/1038899/files/open-2007-018.pdf. 2007.

[137] Martin J Berger and Stephen M Seltzer. *Stopping powers and ranges of electrons and positrons*. Tech. rep. NBSIR 82-2550. U.S. DEPARTMENT OF COMMERCE National Bureau of Standards Washington, DC 20234, 1982.

[138] Philippe Grangier, Gerard Roger, and Alain Aspect. "Experimental evidence for a photon anticorrelation effect on a beam splitter: a new light on single-photon interferences". In: *EPL (Europhysics Letters)* 1.4 (1986), p. 173.

[139] *A 50-50 beamsplitter from Thorlabs*. https://www.thorlabs.com/thorproduct.cfm?partnumber=BSW27. Accessed: 2021-08-06.

[140] Chong-Ki Hong, Zhe-Yu Ou, and Leonard Mandel. "Measurement of subpicosecond time intervals between two photons by interference". In: *Physical Review Letters* 59.18 (1987), p. 2044.

[141] Charles Santori et al. "Indistinguishable photons from a single-photon device". In: *Nature* 419.6907 (2002), pp. 594–597.

[142] H Ollivier et al. "Hong-Ou-Mandel interference with imperfect single photon sources". In: *Physical Review Letters* 126.6 (2021), p. 063602.

[143] T Sh Iskhakov et al. "Macroscopic Hong–Ou–Mandel interference". In: *New Journal of Physics* 15.9 (2013), p. 093036.

[144] A.L. Romanov et al. "3D Tracking of a Single Electron in IOTA". In: *Proc. IPAC'21* (Campinas, SP, Brazil). International Particle Accelerator Conference 12. JACoW Publishing, Geneva, Switzerland, Aug. 2021, THXB01, pp. 3708–3713. ISBN: 978-3-95450-214-1. DOI: 10.18429/JACoW-IPAC2021-THXB01. URL: https://jacow.org/ipac2021/papers/thxb01.pdf.